Simulations of Low-Frequency Electromagnetic Fields in the Human Body.

Vom Fachbereich Elektrotechnik und Informationstechnik
der Technischen Universität Darmstadt
genehmigte Dissertation
vorgelegt von

Dipl.Phys. Andreas Barchanski

geboren in Kattowitz

Darmstadt 2007

Referent:	Prof. Dr.-Ing. Thomas Weiland
Korreferent:	Prof. Dr.-Ing. Volkert Hansen
Prüfer:	Prof. Dr.-Ing. Gerd Balzer
Prüfer:	Prof. Dr. Alex Gershman

Tag der Einreichung:	01.06.07
Tag der mündlichen Prüfung:	02.10.07

D 17

Contents

1 Introduction **5**
- 1.1 Overview . . . 5
- 1.2 Historical Introduction . . . 6
- 1.3 Electromagnetic fields and biological tissue . . . 7
  - 1.3.1 The electromagnetic spectrum . . . 7
  - 1.3.2 Low-frequency interaction . . . 8
  - 1.3.3 Biological effects and restriction levels . . . 9

2 Modeling and Computational Framework **13**
- 2.1 Dielectric Properties of Biological Tissue . . . 13
- 2.2 Geometrical Modeling of the Human Body . . . 17
- 2.3 Discrete Electromagnetic Field Theory . . . 21
  - 2.3.1 Finite Integration Technique . . . 22
  - 2.3.2 Other Computational Methods . . . 25

3 Electric Excitation **29**
- 3.1 Electro Quasi-Static Formulation . . . 29
- 3.2 Impact of the Displacement Current . . . 31
- 3.3 Subgridding for the Electro Quasi-Static Formulation . . . 35
  - 3.3.1 Saddle Point Formulation . . . 35
  - 3.3.2 Interpolation and Local Modifications . . . 37
  - 3.3.3 Results and Conclusions . . . 39
- 3.4 Simulations of Bioimpedance Spectroscopy . . . 42
  - 3.4.1 Simulation Results . . . 43
  - 3.4.2 Comparison of Measurements and Simulations . . . 49
  - 3.4.3 Simple Stylized Phantom for Segmental Impedance Calculations . . . 51

4 Magnetic Excitation **55**
- 4.1 Calculation of Induced Currents . . . 56
  - 4.1.1 Scalar-Potential Finite-Differences (SPFD) Approach . . . 56
  - 4.1.2 Curl-Curl Equation . . . 57
  - 4.1.3 Extended-SPFD (Ex-SPFD) Approach . . . 59
  - 4.1.4 Vector Poisson System . . . 67
- 4.2 Applications . . . 69
  - 4.2.1 Dosimetric Analysis of an Electric Blanket . . . 69
  - 4.2.2 Introduction to Transcranial Magnetic Stimulation (TMS) . . . 73
  - 4.2.3 Transient Calculation of Induced Currents during TMS . . . 75
  - 4.2.4 Mapping Study of the Motor Cortex . . . 81

5 Summary and Outlook **89**

A Solution of Large, Linear Systems of Equations **93**

Applied Notations and Symbols **96**

Bibliography **100**

Acknowledgments **109**

Curriculum Vitae **111**

Chapter 1

Introduction

1.1 Overview

The research area of bioelectromagnetism examines the electromagnetic phenomena which arise in biological tissues. By definition, bioelectromagnetism is interdisciplinary and connects the classical disciplines of biology, medicine, physics, (electro-)chemistry and engineering. Particularly, the interaction of external electromagnetic fields with the human organism has gained increasing attention throughout the past years. Owing to the increasing number of electromagnetic and wireless devices in our daily surroundings, some concern about possible adverse health effects of electromagnetic fields appeared in public opinion. On the other hand, electromagnetic phenomena are used day by day as examination and therapeutic tools in various medical applications.

In this thesis, the interaction of low-frequency electromagnetic fields with the human body is analyzed using field simulations. The electromagnetic field quantities are calculated using the Finite Integration Technique (FIT), that is a discrete electromagnetic field theory formulated on a computational grid. In all calculations, a high-resolution, three dimensional phantom of the human body obtained from modern medical imaging techniques is used. The simulation results allow to gain insight into the electromagnetic field distribution, even inside the body which cannot be easily accessed by measurements. Still, it is a very important and challenging task to find application set-ups, that allow to compare the calculated results with measurements, in order to estimate the accuracy of the used modeling techniques. The simulations of bioimpedance spectroscopy in Sec. 3.4 and the mapping studies of Transcranial Magnetic Stimulation (TMS) in Sec. 4.2.4 are devoted to this task.

Due to the complicated structure of the human body, consisting of organs with varying dimensions and geometrically complicated shapes, all exhibiting different electrical properties, the major task from the simulations point of view is to achieve a very fine spatial resolution in the computations. Two different domain decomposition approaches have been selected to tackle this problem: A subgridding scheme presented in Sec. 3.3, where the local area of interest is resolved finely, while the grid in the surroundings is kept coarse. And, a new algorithm for the efficient calculation of induced currents inside the human body, originating from a low-frequency magnetic field exposure. This algorithm was implemented for a parallel computer architecture, allowing to simultaneously solve one large problem on multiple workstations (App. A).

This thesis is organized as follows. In the next section, a short history of bioelectromagnetism will be presented. It is followed by a characterization of the frequency dependent interaction of electromagnetic fields and biological tissue with emphasis on the low-frequency regime. Sec. 2.1 and 2.2 cover the data used as input for the simulations. This are the dielectric properties of various tissue types and the geometrical modeling of the human body. After introducing the Finite Integration Technique in Sec. 2.3, which establishes the basis of all field calculations in this thesis, some general remarks on the computation of electromagnetic fields in tissue, along with commonly used numerical techniques are presented. In the low-frequency regime two different types of imposing a current flow inside biological tissue can be classified: direct contact of tissue to an electric potential difference (electric excitation) and induction of currents inside the tissue by an external time-varying magnetic field (magnetic excitation). Since both excitation types also come along with different mathematical descriptions, the structure of this thesis follows this classification. Chapter 3 deals with models excited electrically. After an introduction of the electro quasi-static formulation in Sec. 3.1, the impact of the displacement current on the calculated field is examined in Sec. 3.2. In the next section, a subgridding scheme for a local grid refinement based on Lagrange multipliers is presented. The last Sec. 3.4 of this chapter presents the simulations of bioimpedance spectroscopy, a medical examination technique performed with electric excitation. At the beginning of chapter 4, the Scalar-Potential Finite-Differences (SPFD) approach is introduced. This approach was proposed in 1996 for the calculation of induced currents inside the body arising from a low-frequency magnetic field exposure. In Sec. 4.1.3 this approach will be extended to handle arbitrarily shaped field sources and highly conductive material in the computational domain. Two application examples will be presented. First, the dosimetric calculation of induced currents from an electric blanket. Second, in Sec. 4.2.2, the calculation of currents inside the brain during transcranial magnetic stimulation, along with a mapping study of the motor cortex. The thesis ends with a conclusion and an outlook on future work in chapter 5. In the appendix, a short introduction to the solution of large, linear systems of equations on parallel architectures will be given.

1.2 Historical Introduction

The first written document on bioelectromagnetism originates in ancient Egypt and was written around 4000 B.C.. It describes the electric sheatfish, which is capable to produce an electric discharge, that is used to stun or kill prey. In 46 A.D., the roman Scrobonius Largus proposed to use the electricity generated by fishes to cure headaches and arthritis. Electric fishes remained the only source of electricity until the seventeenth century. First experiments on muscle contraction of animals were performed by Jan Swammerdam around 1660, but he was probably not aware of the electrical origin of the observed phenomenon. The invention of the Leyden jar in 1745 by Kleist lead to the possibility to store electrical energy and conduct more studies on electric muscular stimulation. Luigi Galvani performed numerous experiments on the excitation of frog muscles by a voltage from a bimetallic junction in the 1780s. His experiments were continued by Alessandro Volta, who is also the inventor of the first battery, called the Voltaic pile, in 1800. The invention of the induction coil by Michael Faraday in 1831 represents a further progress in stimulation equipment. In 1874, Robert Bartholow used the induction coil for a stimulation of the exposed cerebral cortex and observed that currents can elicit movement in the limb of

the opposite side. In the late 1880s, Jacques d'Arsonval analyzed the interaction of strong time-varying magnetic fields with living tissue and discovered the phenomenon of magnetophosphenes. In the twentieth century, the technique of electric stimulation of tissue was exploited in medical applications like the cardiac pacemaker or the cardiac defibrillator. In 1985, the first magnetic brain stimulation equipment was presented by Barker.
First measurements of electric signals originating from living tissue were performed by Carlo Matteucci in 1838 on frog muscles. The electric brain activity of monkeys and rabbits was first measured by Richard Cation in 1875, constituting the discovery of the electroencephalogram (EEG). In 1924, Hans Berger performed first EEG measurements on humans, identifying the two major brain rhythms. The electrical activity of the human heart, the electrocardiogram (ECG) was first measured in 1887 by Augustus Waller. Around 1910 Willem Einthoven developed the first high-quality ECG recorder, establishing the fundament of this widely spread examination method. Because of the small amplitude of magnetic fields originating from biological tissue, it took until the 60s of the twentieth century to perform measurements. The magnetocardiogram (MCG) was first recorded in 1963 by Gerhard Baule and Richard McFee, followed by the magnetoencephalogram (MEG) in 1970 by David Cohem.
This short introduction to the history of bioelectromagnetism was mainly focused on the excitation of tissue and the measurement of electromagnetic signals originating from living organisms. For further information about the the numerous contributions to this research area, the reader is referred to [1].

1.3 Interaction of electromagnetic fields with biological tissue

The interaction of electromagnetic fields with biological systems is strongly frequency dependent. At the beginning of this section, an overview of the effects of electromagnetic fields in the whole frequency spectrum is given. It is followed by simple theoretical estimates, that provide a framework to quantify the magnitudes of the electromagnetic fields encountered in this thesis. Finally, a short review of observed effects and basic restriction levels for an exposure to low-frequency electromagnetic fields will be given.

1.3.1 The electromagnetic spectrum

At wavelengths shorter than of visible light ($\lambda < 400$ nm, $f > 700$ THz) electromagnetic radiation can ionize atoms and molecules in the biological tissue, leading to a significant damage. The interaction mechanisms of radiation and tissue at these wavelengths are mostly governed by the laws of quantum mechanics. Traditionally, research in this branch is performed at nuclear physics institutes rather than in electrical engineering. The spectrum of electromagnetic radiation of wavelengths longer than of visible light starts with the infrared region, ranging from approximately 750 nm to 1 mm (400 THz $> f >$ 300 GHz). The frequency range from 300 GHz down to static fields represents the classical regime that is defined as electromagnetic fields by various radiation protection boards like the *International Commission on Non-Ionizing Radiation Protection (ICNIRP)*, or the *World Health Organization (WHO)*, when referred to biological effects. The following classification is based on the ICNIRP guidelines published in [2].

Due to the skin effect, radiation of frequencies higher than 10 GHz cannot penetrate biological tissue of organisms and so results in a heating of its surface. The dosimetric quantity at these frequencies is the power density, i.e. the power per unit area normal to the direction of propagation. At frequencies from 100 kHz to 10 GHz, the concept of the specific absorption rate (SAR) is used. SAR, measured in W/kg, is defined at a point in the absorber as the time rate change of energy transferred to an infinitesimal volume at this point divided by the mass of the infinitesimal volume:

$$SAR = \frac{P}{\rho_m} = \frac{\omega \varepsilon_0 \varepsilon'' |\vec{E}|^2}{\rho_m}. \tag{1.1}$$

Here, P denotes time averaged rate of energy absorbed per unit volume, ρ_m is the mass density of the the object at that point, $|\vec{E}|$ is the rms magnitude of the E-field, ω the angular frequency, ε_0 the permittivity of free space and ε'' the imaginary part of the complex relative permittivity. In strongly inhomogeneous tissue like the human body, the SAR distribution is also non uniform especially in a near-field exposure. Local hot spots can occur in tissue, since the absorbed energy results in a temperature increase. The widespread of mobile phones operating at GHz frequencies in the past years has lead to a vast increase of numeric calculations of the SAR distribution.
For frequencies ranging from several Hz up to 10 MHz, the ICNIRP guidelines propose the current density $\vec{J}$ (A/m^2) as the appropriate dosimetric quantity. The internal electric field and the current density are related by Ohm's Law,

$$\vec{J} = \kappa \vec{E}. \tag{1.2}$$

Here, κ denotes the conductivity tensor. The results obtained in this thesis are all presented in terms of the current density or the electric field strength. In the intermediate frequency range from 100 kHz to 10 MHz both, the current density and the specific absorption rate are valid dosimetric quantities according to the ICNIRP guidelines. Although the calculations of transcranial magnetic stimulation presented in Sec. 4.2.3 consider frequency components up to 300 kHz, there is no need to incorporate the SAR concept. Since the interest of this simulations is focused on the excitation of neural tissue, small thermic effects will remain unconsidered.

1.3.2 Low-frequency interaction

At low frequencies, the electromagnetic wavelength is much larger than the spatial dimensions of biological structures. Even at the frequency of 1 MHz, the wavelength amounts to $\approx$ 300 m, more than two orders of magnitude larger than the height of the human body. Therefore, wave propagation effects can be neglected and the electric and magnetic field can be treated as uncoupled.
Consider two materials with the conductivity κ and permittivity ε, exposed to an low-frequency electric field $\vec{E}$. Let $E_\parallel$ denote the component parallel to the boundary and $E_\perp$ the component perpendicular to the boundary. Due to the continuity condition at the interface of material 1 and material 2 we obtain

$$E_{\perp 1} = \frac{\kappa_2 + i\omega\varepsilon_2}{\kappa_1 + i\omega\varepsilon_1} E_{\perp 2}, \tag{1.3}$$

after eliminating the surface charge density. Inserting the material properties of air, $\kappa_1 = 10^{-13}$ S/m and $\varepsilon_1 = 10^{-11}$ F/m and those of biological tissue at 50 Hz (see Sec. 2.1)

$\kappa_1 = 10^{-1}$ S/m and $\varepsilon_1 = 10^6$ F/m results in $E_{\perp 1} \approx -i\ 3.1 \cdot 10^7 E_{\perp 2}$. Defining θ as the angle between the boundary and the electric field vector in the respective material and together with

$$E_{\parallel 1} = E_{\parallel 2} \quad \tan\theta_{1/2} = \frac{E_{\perp 1/2}}{E_{\parallel 1/2}} \tag{1.4}$$

we obtain $\tan\theta_1 \approx 3.1 \cdot 10^7 \tan\theta_2$. This result shows, that for the given material properties, the field in air is practically perpendicular to the boundary of a living organism and that the organism strongly disturbs the external electric field. We can also conclude, that the electric field inside the tissue will be much smaller than the field in the air region e.g. at 50 Hz an external field of 100 kV/m will produce an average internal electric field of 4 mV/m. Primary effects of an exposure of the body to an electric field are: a current flow due to an accumulation of a surface charge density, the polarization of bound charge and the reorientation of dipoles in the tissue. No calculations of an electric field exposure will be performed in this work, but can be found in [3].
Since the magnetic permeability of (macroscopic) biological tissue is equal to the vacuum permeability μ_0, a static magnetic field is not disturbed by the organism. Besides orientation effects of magnetic molecules and particles, also forces on moving ions can be observed. However, the predominant effect of a time-varying magnetic field is the induction of an electric field and eddy currents inside the weakly conductive tissue. Consider a circular path enclosing a magnetic flux density perpendicular to the plane of the loop. Then the magnitude of the induced electric current density is given by

$$J = \kappa E = \kappa \frac{\omega B r}{2}, \tag{1.5}$$

where r denotes the radius of the loop. In Eqn. 1.5, the magnetic field generated by the induced currents is neglected. The justification for this simplification will be further elaborated in Sec. 4.1.3. Choosing a radius of 10 cm and a conductivity of 0.1 S/m at 50 Hz, a magnetic flux density of 0.64 mT is needed to induce an electric field of 10 mV/m, corresponding to a current density of 1 mA/m^2. It is noteworthy, that an external 50 Hz electric field of $\approx$ 250 kV/m would be needed to produce this internal field.

1.3.3 Biological effects and restriction levels

A stimulation of nerve or muscle tissue can occur when the current (density) inside the body reaches a certain threshold. This threshold is depending on the shape and duration of the current, with lowest values in the range from 10 Hz to 500 Hz. The stimulation follows an all-or-none law, therefore, once the threshold is exceeded, higher currents can not increase the response. When the human body is in contact with conductors at a potential difference, a current flow in the body will occur. In the introduction this was called electrical excitation. The results of such a contact current range from a perception of the current, over muscle contractions to severe damage, depending on the magnitude of the current. A substantial amount of experimental data for this scenario is available and the threshold values have been summarized in Tab. 1.1. They are valid for a male person with skin contact to the potential difference at 50 Hz. For an exposure of the body to a low frequency magnetic field a similar classification of the effects, based on the induced current density is given in Tab. 1.2.

Table 1.1: Experimental thresholds for the effects of 50 Hz contact currents on male persons.

Effect	I / mA
Perception threshold finger / grasp	0.36 / 1.1
Painful sensation for finger contact	1.8
Painful sensation for grasp (release possible)	9
Painful sensation for grasp (release partially possible)	16
Strong shock (release not possible)	23
Possible ventricular fibrillation	100

Although the effects summarized in Tab. 1.2 and 1.1 are quite similar, it is important to point out one major difference. In most cases, the different potentials leading to an electric excitation are touched by the limbs, leading to a current flow from e.g. hand to hand or hand to feet. Because of its conductivity value, muscle tissue will carry the largest portion of the current, as it will be pointed out in Sec. 3.4.1. The current in other organs, especially those lying not in the current path, like e.g. the brain will be nearly zero. This is not the case when the body is exposed to a magnetic field, which is able to freely penetrate the tissue. Therefore, the magnetic field will induce currents in every organ that is substantially exposed.

Table 1.2: The effects of induced current densities in the body.

Effect	J / mA/m^2
No confirmed biological effect	<10
Painful sensation, magnetophosphenes, accelerated bone growth	10-100
Health hazards possible, excitation of the nervous system, Distinct damage possible	>100
Additional heart contractions ventricular fibrillation	>1000

From the preceding paragraph it can be concluded that at certain exposure levels adverse health effects are in all probability. There is clearly the need to set up some limits to the exposure of the population to electromagnetic fields. In the ICNIRP guidelines, that have been adopted by many governments worldwide, restriction levels are defined for occupational exposure and for the general public. Since the occupationally exposed population mainly consists of adults, exposed under known conditions and trained to be aware of the risk, the restriction levels for occupational exposure are higher than ones for the general public. Current densities above 100 mA/m^2 can result in acute changes in the central nervous system (Tab. 1.2). In view of safety considerations, the ICNIRP has applied a factor of 10, i.e. for an occupational exposure in the frequency range from 4 Hz to 1 kHz the current density inside the body may not exceed 10 mA/m^2. For the general public, an additional factor of 5 is used, resulting in 2 mA/m^2. Below 4 Hz and above 1 kHz the restriction value increases progressively, corresponding to the increase in the threshold

value for nerve stimulation. Because the current density inside the body can not be easily measured, reference levels for the external fields are defined. They are obtained from the basic restrictions by mathematical modeling and by extrapolation from the results of laboratory investigations at specific frequencies. Surprisingly, nothing more than the simple mathematical model presented in Eqn. 1.5 is used for the calculation of reference levels at the moment.

Since current densities are used as the characteristic quantity throughout this work, the summary of the interaction of low-frequency electromagnetic fields with tissue presented here was focused on the quantification of the effects in terms of current densities. At a final stage of this thesis, analyzing the results of the mapping study in Sec. 4.2.2, the induced electric field turned out to be probably the more appropriate dosimetric quantity for nerve stimulation. Therefore, the results of the mapping study will all be presented in terms of the electric field. However, both quantities can be easily converted into each other using Ohm's law (Eqn. 1.2). Further information as well as a review of biological and epidemiological literature that is beyond the scope of this work can be found in [2].

Chapter 2

Modeling and Computational Framework

In this chapter, the elementary constituents needed to perform electromagnetic simulations in the human body are presented. The modeling framework consists of two sections. A dispersive model for the calculation of the dielectric properties of biological tissue in a broad frequency range is introduced in Sec. 2.1. The mapping of the tissue distribution of the human body to a digital representation that can be used in field simulations is described in Sec. 2.2. In the last section of this chapter, the Finite Integration Technique will be introduced and compared to other calculation methods that have been used for the calculation of low-frequency electromagnetic fields in the human body.

2.1 Dielectric Properties of Biological Tissue

The study of the bulk electrical properties of tissue has been of great interest for more than a century now and is still an active area in actual research. These properties determine the pathways of the current flow through tissue and thus represent crucial input data for the simulations of electromagnetic fields in the body. As early as in 1834, Peltier already discovered that biological tissue can store electric charges, if exposed to DC currents and release it after the termination of the current. It was quickly clear, that the electrical properties of tissue and blood differ greatly from those of simple electrolyte solutions. As electrical technology progressed, first measurements using sinusoidally alternating currents revealed a complex frequency dependence of the dielectric properties of tissue. Particularly, the work of Höber helped to clarify the underlying reason for the strong frequency dependence. Few years after the publishing of the cell membrane hypothesis by Bernstein in 1902, Höber proposed that the cell membrane acts as a capacitor and therefore can be better penetrated by a high frequent current than by a low frequent one. Nowadays, this mechanism is called the β-dispersion. The effects of the β-dispersion on the magnitudes of the currents induced during magnetic brain stimulation will be analyzed in Sec. 4.2.3. During the 1920s and 1930s, the dielectric properties of various cell suspensions and tissue types in the kHz and MHz regime were measured and tabulated. The rapid developments in microwave technology during the Second World War pushed the examined frequency range up to several GHz in the late 1940s. Early theoretical work in this area attempted to apply the dielectric mixture theories proposed e.g. by Maxwell to model the measured behavior, however with rather limited success. In 1941 Cole suggested a model, based on

the theory of dispersion, to describe the complex permittivity of biological tissue. This model has been further extended by several authors like Schwan, Foster and Gabriel.

The work of Gabriel, Gabriel, Corthout and Lau published in 1996, aims in particular at creating a model, that can be easily used to obtain the dielectric properties of various tissues types needed for electromagnetic field calculations based on high-resolution human body models. The model should be easy to use and valid at all frequencies to which the body is exposed. The publication consists of a literature survey [4], new measured data [5] and a parametric model [6] for the dielectric spectrum of tissues. Generally, the dielectric properties of materials are obtained from their measured complex relative permittivity $\underline{\varepsilon}_{\mathrm{rel}}$,

$$\underline{\varepsilon}_{\mathrm{rel}} = \varepsilon^{'} - i\varepsilon^{''} \tag{2.1}$$

where $\varepsilon^{'}$ is the relative permittivity of the material and $\varepsilon^{''}$ is the out-of-phase loss factor associated with it, such that

$$\varepsilon^{''} = \kappa/\varepsilon_0\omega. \tag{2.2}$$

κ is the total conductivity of the material, which also may contain a frequency-independent ionic contribution. Performing such measurements is a very challenging task and several pitfalls have to be avoided. Since the electric properties of tissue begin to change shortly after the death of an organism, *in vivo* measurements are favored over *in vitro* data. Unfortunately, *in vivo* measurements of internal human organs are nearly impossible to perform. Therefore, the available data often origin form measurements performed on animals. For results obtained *in vitro* the time-from-death and the temperature of the sample are vital parameters. Biological tissues are inhomogeneous and exhibit a considerable variability in structure or composition and hence, in the dielectric properties. Such variations are natural and may be due to physiological processes or other functional requirements. The differences in the electrical properties between animal and human are not systematic. It is possible that the variation within a species may exceed the variation between species. Other parameters, like the moisture of the skin, the air content in the lung or the blood infiltration of bone marrow also play an important role. Gabriel *et. al.* report a spread of the measured values in the range from about $\pm 5 - 10$ % above 100 MHz, to $\pm 15 - 25$ % at the lower frequency scale. Not only the sample choice, but also the measuring process itself emerges error prone. The measurements are affected by two sources of systematic errors, electrode polarization and lead inductance errors, which become apparent at the lower and higher ends of the frequency range. Electrode polarization is a manifestation of charge organization, which occurs at the sample-electrode interface in the presence of water molecules and hydrated ions. In its simplest form, this is equivalent to a frequency-dependent capacitor in series with a resistor. The effect increases with increasing sample conductivity. In the case of biological samples, the poorly conducting cells shield parts of the electrode from the ionic current, thus reducing the polarization effects compared to an ionic solution equivalent in conductivity to the intracellular fluid [7]. The inductance of the probe and connecting cables also adds a series component to the measured impedance. Its value is obtained from measurements on standard salt solution, allowing to correct the data measured on tissue.

Fig. 2.1 depicts the values of the conductivity and permittivity of brain gray matter in a frequency range from 10 Hz to 100 GHz. The plots have been reproduced from reference [4] and [5]. In the lower part of the figure, a compilation of literature data as collected by Gabriel *et. al.* is presented. The symbols represent data from various animals as indicated

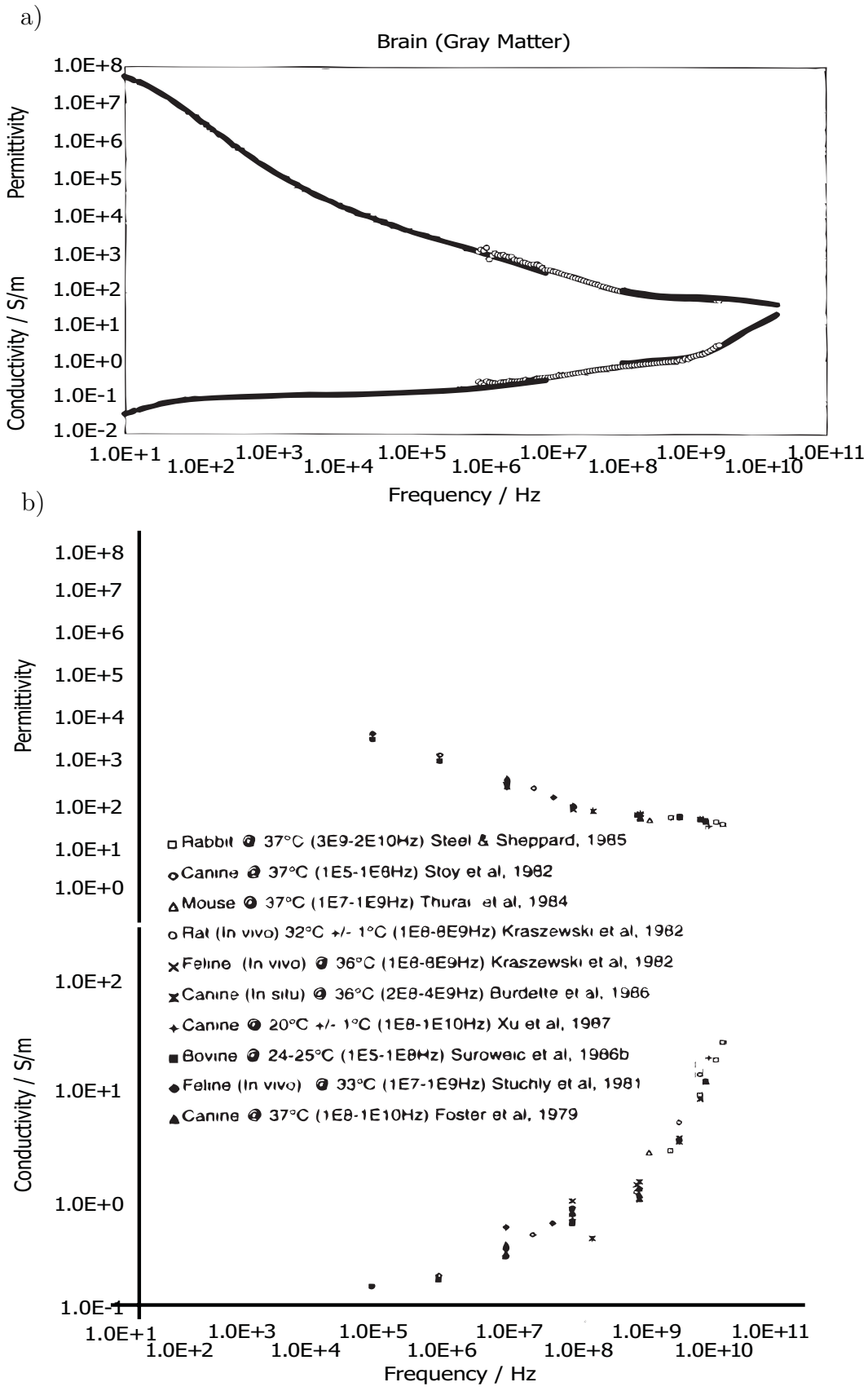

Figure 2.1: The conductivity and permittivity of brain gray matter. a) Measurement results. b) Collection of literature data. Figures reproduced from Gabriel *et. al.* [4, 5]

by the inset. In the upper part of the figure, a plot of data measured by Gabriel *et. al.* on bovine tissue is shown. The white circles represent actually measured values, while the black lines have been extrapolated from the measurements. The absence of data in the low-frequency range is apparent in both plots. This is also the fact for most other tissue types examined and is due to technical difficulties in measurements at low frequencies. For the here presented work, this is a serious drawback. However, at the present time, the model proposed by Gabriel *et. al.* summarizes our knowledge about the dielectric properties of tissue the best and has been widely accepted in the scientific community. Therefore, it will be used throughout this thesis.
The response of a material to a voltage step involves the physical displacement of charge. The kinetics of this displacement determine the frequency dependence of the bulk properties. In the simplest model, relaxation effects may be described by a first order differential equation involving a single relaxation time constant τ. This leads to the well known Debeye expression for the frequency dependence of the complex relative permittivity,

$$\underline{\varepsilon}_{\mathrm{rel}}(\omega) = \varepsilon_\infty + \frac{\varepsilon_\mathrm{s} - \varepsilon_\infty}{1 + i\omega\tau}. \tag{2.3}$$

The magnitude of the dispersion is described as $\Delta\varepsilon = \varepsilon_\mathrm{s} - \varepsilon_\infty$, where ε_s denotes the static permittivity, while ε_∞ refers to the permittivity at infinite frequencies. In fact, only a few materials, like e.g. water exhibit a single constant relaxation behavior. In the case of biological tissue, which is composed of molecules of varying size and bound state, multiple relaxation processes are present. In the simplest case, when all processes are of first order, independent and have well separated relaxations constants, each relaxation process can be described by one Debeye term. However, not all kinetics in biological tissue are of first order and well separated. Cole and Cole have proposed an empirical approach to fit the measured data to the relaxation theory, by introducing a distribution parameter α which measures the broadening of each dispersion region.

$$\underline{\varepsilon}_{\mathrm{rel}}(\omega) = \varepsilon_\infty + \frac{\Delta\varepsilon}{1 + (i\omega\tau)^{1-\alpha}}. \tag{2.4}$$

Functions based on theoretical justifications have also been proposed to fit the available data [8]. However, the resulting distribution functions are often very complicated and awkward to interpret. The empirical approach does not clarify the underlying mechanisms and may lead to non-physical results, like the divergence of the conductivity for $\omega \to \infty$, but it parametrizes the measured data more precisely. The dispersion relations do not incorporate the existence of a DC current due to the movement of ions in a constant field. This effect is modeled by introducing the static ionic conductivity κ_{ion}. In the parametric model proposed by Gabriel *et. al.* four dispersion regions are used, resulting in 14 parameters for each tissue type:

$$\underline{\varepsilon}_{\mathrm{rel}}(\omega) = \varepsilon_\infty + \sum_{n=1}^{4} \frac{\Delta\varepsilon_n}{1 + (i\omega\tau_n)^{1-\alpha_n}} + \frac{\kappa_{\mathrm{ion}}}{i\omega\varepsilon_0}. \tag{2.5}$$

For all simulations presented in this thesis, this parametric Cole-Cole equation along with the data given in [6] will be used.

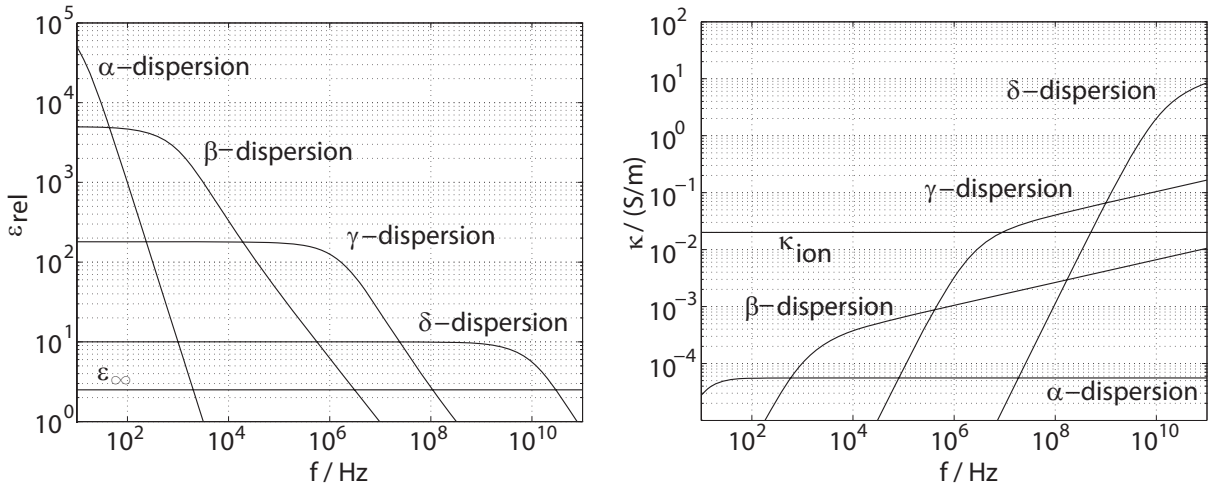

Figure 2.2: Double logarithmic plot of the impact of the four dispersion regions on the relative permittivity and the conductivity, as calculated for bone tissue using (2.5).

The impact of the four dispersion regions on the relative permittivity and the conductivity for bone tissue is depicted in Fig. 2.2. The values have been calculated using Eqn. (2.5). Each dispersion region can be attributed to several mechanisms [9]:

- α-dispersion (mHz-kHz) counterion effects near the membrane surfaces, active cell membrane effects and gated channels, intracellular structure (e.g. sarcotubular system), ionic diffusion, dielectric losses
- β-dispersion (0.1-100 MHz) Maxwell-Wagner effects, passive cell membrane capacitance, intracellular organelle membranes, protein molecule response.
- γ-dispersion (0.1-100 GHz) Dipolar mechanisms in polar media such as water, salts and proteins.
- δ-dispersion (> 5 GHz) Dipolar relaxation of bulk water

It is a well known fact, that the microscopic composition of certain tissue types leads to a distinct anisotropy of the dielectric properties. Most prominent, muscle tissue, consisting of bunches of long fibers exhibits a conductivity contrast of 4 to 9, with higher values in the direction parallel to the fiber. A similar behavior can be observed in nerve bundles. Unfortunately, no data of the orientation of the particular tissue was available to the author. Therefore, all calculations presented in this work have been performed using isotropic models. Results of calculations, incorporating the anisotropy can be found in [10]. Obtaining anisotropic data and the incorporation of the anisotropy into the simulations remain tasks for the future.

2.2 Geometrical Modeling of the Human Body

In the last section, it was shown that the dielectric properties of biological tissue exhibit a distinct variance. At a given frequency, the conductivities can span more than three orders of magnitude (e.g. at 50 Hz, blood 1.5 S/m, bone marrow 0.0016 S/m). Because

of this strong variation of the dielectric properties, realistic body models that reflect the inhomogeneity of the human body are needed for electromagnetic field simulations. Such computational phantoms are also needed in the branch of nuclear radiation dosimetry. The first published works on human-body phantoms were concerned with nuclear radiation safety, rather than electromagnetic field exposure. Basically the available phantoms can be divided into two groups. Stylized phantoms describe the human anatomy by using simple mathematical equations of analytical geometry. Tomographic phantoms are obtained from modern medical imaging techniques, like the Magnetic Resonance Imaging (MRI), or the Computed Tomography (CT) and represent the body by sampled volume pixels, the so-called voxels.
The first available stylized phantoms consisted of extremely simplified geometries like a 30 cm thick slab or a circular cylinder, 30 cm in diameter and 60 cm in height. In 1966 a more detailed phantom was developed by Fisher and Snyder at the Oak Ridge National Laboratory. It was revised in 1969 according to reference data published by the International Commission on Radiological Protection (ICRP) and became well-known as the Medical Internal Radiation Dose (MIRD) 5 phantom [11]. In the following time, the MIRD 5 phantom has been revised several times, male and female phantoms were constructed and also phantoms of pregnant women were utilized to calculate internal dosimetry. Because the dimensions of the body and organs, as well as, the position of the organs inside the body differ from child to adult, special effort has been made to obtain pediatric phantoms at several ages [12]. Although in most actual publications tomographic phantoms are used, stylized phantoms have lately been further improved by several authors [13, 14].
The demand to represent the human body more realistically was the major motivation for the development of tomographic (from Greek, tomos = slice) phantoms. Even though mathematical equations offer some advantages, like e.g. scalability, they are inherently limited with respect to their capacity to describe the complexity of the human anatomy. Advances in computational power and medical imaging made it possible to obtain slice images of the human body, segment the images into the various tissue types and stack the images into a three-dimensional voxel matrix. The first tomographic phantoms were reported in the first half of the 1980's, however, yet with a rather limited resolution. In 1989, the *United States National Library of Medicine* formulated the goal to construct a high-resolution, tomographic phantom of the human body in the framework of the so-called Visible Human Project as follows:

'NLM should undertake a first project building a digital image library of volumetric data representing a complete, normal adult male and female. This Visible Human Project will include digitalized photographic images from cryosectioning, digital images derived from computerized tomography and digital magnetic resonance images of cadavers'

The results of this project have been made available to the public in 1994. Nowadays, comfortable free-of-charge interfaces to the Visible Human images exist on the web [15]. A sample of the raw data obtained for the construction of the Visible Human model is depicted in Fig. 2.3. The left side shows the slice photography data that was taken with a resolution of 0,33 mm x 0,33 mm x 1 mm. In the center of the figure, CT data with a resolution of 0,94 mm x 0,94 mm x 1 mm is shown, while the right side depicts MRI data at a resolution of 1,88 mm x 1,88 mm x 4 mm. These data sources were semi-automatically segmented by anatomists into more than 30 different tissue types [16]. In the finest resolution, the

Figure 2.3: Axial slices through the brain of the visible human. Left: slice photography, center: CT scan, right: MRI data.

model consists of ≈ 380 Mio. voxels, with a edge length of 1 mm. Due to the large amount of data, the Visible Human is also available in coarser resolutions, up to an edge length of 8 mm. The Visible Human data was obtained from the donated body of an executed 38-years-old male convict. Although the height (≈ 180 cm) and weight (≈ 90 kg) are far from reference Caucasian data, this phantom currently has the highest available voxel resolution and will be used in this thesis. Several other tomographic phantoms have been used in the area of electromagnetic field dosimetry. Some of this phantoms have been normalized to match reference data, while others are unmodified. A selection of the most prominent phantoms, along with a reference to the according publication is listed in Tab. 2.1. For a more complete list, the reader is referred to [17].

Table 2.1: A selection of available tomographic phantoms

Phantom	Image type	Subject	Race	Age and gender	Reference
Zubal	CT	Diffuse melanoma	Caucasian	Adult male	[18]
Norman	MRI	N/A	Caucasian	Adult male	[19]
Naomi	MRI	Volunteer	Caucasian	23-year old female	[20]
Korman	MRI	Volunteer	Korean	30-year old male	[21]
Taro	MRI	Volunteer	Japanese	22-year old male	[22]
Hanako	MRI	Volunteer	Japanese	23-year old female	[22]

Most of the available tomographic phantoms represent the body in a lying position. In its original version, the hands of the Visible Human phantom are touching the upper thighs, connecting the arms and legs electrically. After the release of the Visible Human model, effort has been made to obtain a flexible phantom, that can represent the body in any posture. Typically, the desired posture is specified on a simple stick-man model and then the volume data is transformed according to the settings [23]. Such transformations are non-trivial. Several constraints, like the mass conservation of each tissue type, the continuity of blood vessels, or the different elasticity of tissues have to be followed. At the moment, no such software was available to the author. All presented whole-body calculations were performed using the original Visible Human model. It is noteworthy,

that the impact of the posture of the body is less pronounced for the currents induced by an external magnetic field, since the low-frequency magnetic field can freely penetrate biological tissue. This is contrary to an electric field exposure, where the body severely alters the external field. In cases in which the electrical connection of arms and legs is of importance, the connecting interfaces were overwritten by bricks of air. Care was taken to only slightly modify the tissue distribution.
Recently, a new approach to overcome the limitations of stylized and tomographic phantoms have been undertaken. A hybrid phantom that combines the easy-to-standardize mathematical equations of stylized phantoms and the anatomical realism of tomographic phantoms. The internal organs and body contours are segmented from medical images, the surfaces are then sampled using non-uniform rational B-splines (NURBS) [24, 25]. This approach allows to realistically describe the human anatomy with smooth organ surfaces, while the organ position and shape can be easily transformed to match reference data.
The use of computational phantoms imposes a severe limit on the possibility to compare measurement results and simulation data. This topic will be further discussed in Sec. 3.4.2. The development of a whole-body phantom is a very time consuming task and is commonly carried out by specialists. However, in some applications it is sufficient to model only parts of the body. Throughout the past years, the MRI technique was established as a reliable and widely spread imaging technology. Contrary to the CT, no ionizing radiation is needed. Thus the MRI technique allows to obtain data sets of healthy volunteers with a minimum of possible risk. Current state-of-the-art MRI devices offer a resolution of 1 mm, allowing to capture anatomically realistic scans of individuals, that can be further processed for use in electromagnetic field simulations. For the calculation of the induced current densities during magnetic stimulation in Sec. 4.2.2, two brain models obtained from individual subjects were used. The recent progress in functional neurological imaging technology has emerged easy-to-use tools for the manipulation of MRI based voxel data. The Statistical Parametric Mapping (SPM) [26] software package has been designed for the analysis of brain imaging data sequences. It offers an automatic tissue segmentation procedure, based on a probabilistic framework. The segmentation is performed by a hybrid method, called unified segmentation [27], that is a mixture of tissue classification based on voxel intensities and a registration of the data to a template brain. The so obtained model differentiates three tissue types: gray matter, white matter and cerebrospinal fluid (CSF). In the second brain model, used for the mapping study, also the skull bone and the dura was incorporated into the model. Segmentation of this tissues was performed using the FMRIB software library [28, 29]. The segmented data from SPM and FMRIB was combined into one model using Matlab.

Rendered images of the second brain model and the Visible Human at a resolution of 1 mm are presented in Fig. 2.4. An advanced rendering algorithm was used to produce the images. Some sections have been cut-out and made transparent in order to allow to see the inner parts of the models. Only the upper part of the Visible Human phantom is shown. This images give a good impression on the level of detail offered by the models.
The use of tomographic phantoms or segmented MRI data offers a fine spatial resolution for electromagnetic field calculations. However, each voxel belonging to a given tissue type will always be assigned to one conductivity value, not allowing to incorporate the inhomogeneity found in the same tissue type. To overcome this restriction Sekino *et. al.* have proposed a novel method to non-invasively measure the conductivity distribution in biological tissue [30]. The method is based on diffusion-weighted MRI. Since low-frequency

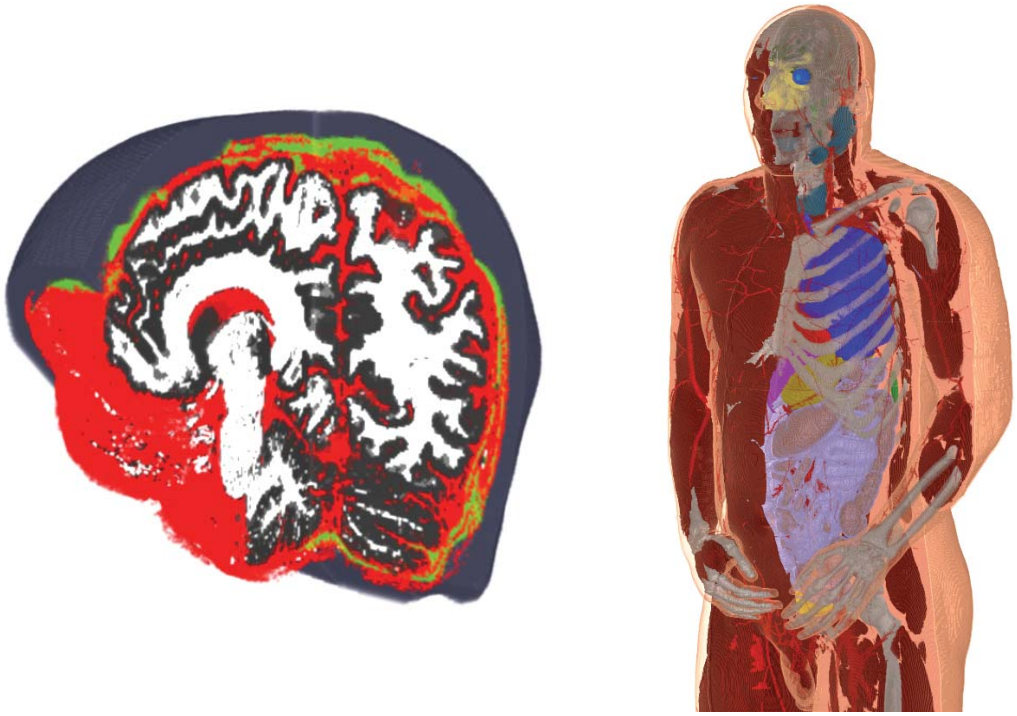

Figure 2.4: Rendered images of the brain model used in Sec. 4.2.4 and the upper part of the Visible Human phantom.

currents are mainly conducted by the migration of ions in the extracellular fluid the conductivity depends on the viscosity of the extracellular fluid. Using the Einstein-Stokes equations the viscosity can be obtained from the diffusion coefficient, which is estimated using so-called motion probing gradients. With the motion probing gradients aligned at the three spatial directions Sekino's method also allows to measure the conduction anisotropy found in tissue [31]. This novel approach is very promising to greatly enhance the modeling detail of the human body for electromagnetic field calculations. However, at the moment the spatial resolution in this measurements is not satisfactory.

2.3 Discrete Electromagnetic Field Theory

Analytic solutions of electromagnetic field problems can only be obtained for a limited number of simple geometries. As an example, the human head can be modeled by a multi-layered sphere, for which an analytic solution can be derived [32]. However, the analytical approach can only provide estimates of the order of magnitude of the electromagnetic fields and lacks anatomical realism. In order to respect the distinct inhomogeneity of the human body, numerical methods are commonly used. For this purpose, the Finite Integration Technique (FIT) is used throughout this work. The FIT was first proposed by Weiland in 1977 [33] and has been developed further throughout the years by numerous contributors, resulting in an extensive library of discrete electromagnetic formulations [34, 35, 36, 37]. The method is based on a discretization of the integral Maxwell Equations on a computational grid.

2.3.1 Finite Integration Technique

All electromagnetic field phenomena can be described using a set of four equations compiled by Maxwell in 1864. They can be denoted in an integral and a differential form as:

$$\oint_{\partial A} \vec{E}(\vec{r},t)\ d\vec{s} = -\int_A \left(\frac{\partial \vec{B}(\vec{r},t)}{\partial t}\right)\ d\vec{A} \quad \Leftrightarrow \quad \nabla \times \vec{E}(\vec{r},t) = -\frac{\partial \vec{B}(\vec{r},t)}{\partial t} \tag{2.6}$$

$$\oint_{\partial A} \vec{H}(\vec{r},t)\ d\vec{s} = \int_A \left(\frac{\partial \vec{D}(\vec{r},t)}{\partial t} + \vec{J}\right)\ d\vec{A} \quad \Leftrightarrow \quad \nabla \times \vec{H}(\vec{r},t) = \frac{\partial \vec{D}(\vec{r},t)}{\partial t} + \vec{J} \tag{2.7}$$

$$\int_{\partial V} \vec{D}(\vec{r},t)\ d\vec{A} = \int_V \rho(\vec{r},t)\ dV \quad \Leftrightarrow \quad \nabla \cdot \vec{D}(\vec{r},t) = \rho(\vec{r},t) \tag{2.8}$$

$$\int_{\partial V} \vec{B}(\vec{r},t)\ d\vec{A} = 0 \quad \Leftrightarrow \quad \nabla \cdot \vec{B}(\vec{r},t) = 0 \tag{2.9}$$

for all $A, V \in \mathbb{R}^3$. $\vec{E}$, $\vec{H}$ refer to the electric and magnetic field, respectively. $\vec{D}$ is the electric flux density, $\vec{B}$ the magnetic flux density, $\vec{J}$ the current density and ρ the charge density. For most practical cases the differential form of the Maxwell equations are used. To ensure uniqueness of the solution, when using the differential form, appropriate boundary conditions for the fields are required. The Eqn. set (2.6 - 2.9) does not include the material properties. They are taken into account by introducing the constitutive material equations, that relate the fields to the flux densities:

$$\vec{D}(\vec{r},t) = \varepsilon_0 \vec{E}(\vec{r},t) + \vec{P}(\vec{r},t) \tag{2.10}$$

$$\vec{B}(\vec{r},t) = \mu_0[\vec{H}(\vec{r},t) + \vec{M}(\vec{r},t)]. \tag{2.11}$$

Here, ε_0 and μ_0 are the permittivity and permeability of free space. $\vec{P}(\vec{r},t)$ denotes the polarization and $\vec{M}(\vec{r},t)$ the magnetization of the medium. In general, the polarization and the magnetization are time-dependent, nonlinear functions. However, in the cases presented in this thesis only linear, isotropic materials, without permanent polarization or magnetization are of importance, reducing (2.10) and (2.11) to

$$\vec{D}(\vec{r},t) = \varepsilon_0 \varepsilon_\mathrm{r}(\vec{r}) \vec{E}(\vec{r},t) \tag{2.12}$$

$$\vec{B}(\vec{r},t) = \mu_0 \mu_\mathrm{r}(\vec{r}) \vec{H}(\vec{r},t). \tag{2.13}$$

For the numerical solution of an electromagnetic field problem, a finite computational domain is defined. The procedure of mapping of the physical quantities from the continuous space to a discrete subspace defined on a grid is called discretization. In the FIT, the discretization is performed on a system of staggered, dual, orthogonal grids G and $\tilde{G}$, using integral state variables defined as:

$$\widehat{e}_i(t) = \int_{L_i} \vec{E}(\vec{r},t)\ d\vec{s} \qquad \widehat{h}_i(t) = \int_{\tilde{L}_i} \vec{H}(\vec{r},t)\ d\vec{s}$$

$$\widehat{\widetilde{d}}_i(t) = \int_{\tilde{A}_i} \vec{D}(\vec{r},t)\ d\vec{A} \qquad \widehat{\widetilde{b}}_i(t) = \int_{A_i} \vec{B}(\vec{r},t)\ d\vec{A}$$

$$\widehat{\widetilde{j}}_i(t) = \int_{\tilde{A}_i} \vec{J}(\vec{r},t)\ d\vec{A} \qquad q_{e_i}(t) = \int_{\tilde{V}_i} \rho_e(\vec{r},t)\ dV.$$

All tilded symbols refer to the dual grid, where L_i, $\tilde{L}_i$ denote the edges, A_i, $\tilde{A}_i$ the facets and V_i, $\tilde{V}_i$ the cell volumes. This allocation of the state variables to the geometric primitives of the computational grid is drafted in Fig. 2.5 a).

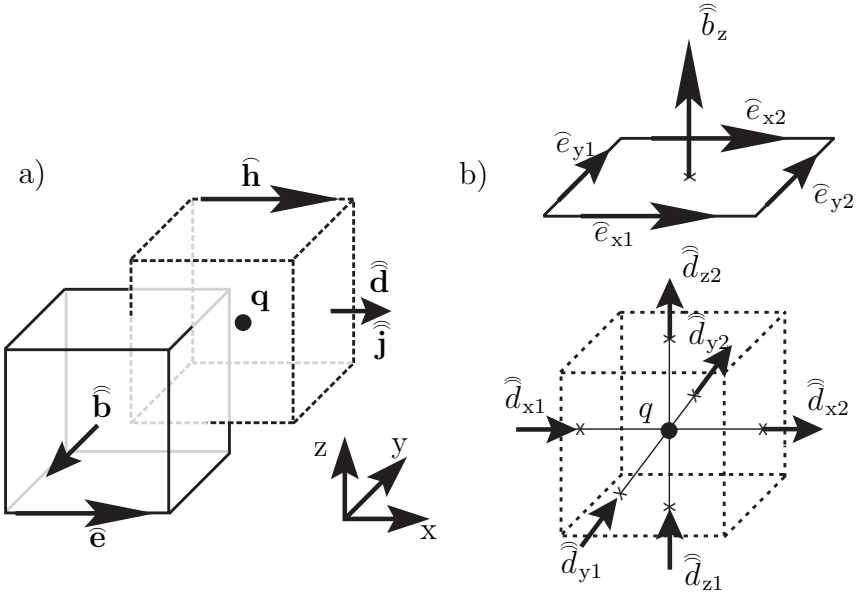

Figure 2.5: FIT grid: Primary grid in full lines, dual grid in dashed lines. a) Allocation of field quantities to the geometric primitives. b) Discretization of Eqn. (2.6) and (2.8).

Applying the Maxwell equations in their integral form to a single facet (2.6 & 2.7), or cell (2.8 & 2.9) of the computational grid and using the integral state variables we obtain:

$$\widehat{e}_{x1} + \widehat{e}_{y2} - \widehat{e}_{x2} - \widehat{e}_{y2} = -\frac{d}{dt}\widehat{\hat{b}}_z \tag{2.14}$$

$$\widehat{h}_{x1} + \widehat{h}_{y2} - \widehat{h}_{x2} - \widehat{h}_{y2} = \frac{d}{dt}\widehat{\hat{d}}_z + \widehat{\hat{j}}_z \tag{2.15}$$

$$-\widehat{\hat{d}}_{x1} + \widehat{\hat{d}}_{x2} - \widehat{\hat{d}}_{y1} + \widehat{\hat{d}}_{y2} - \widehat{\hat{d}}_{z1} + \widehat{\hat{d}}_{z2} = q \tag{2.16}$$

$$-\widehat{\hat{b}}_{x1} + \widehat{\hat{b}}_{x2} - \widehat{\hat{b}}_{y1} + \widehat{\hat{b}}_{y2} - \widehat{\hat{b}}_{z1} + \widehat{\hat{b}}_{z2} = 0. \tag{2.17}$$

Fig. 2.5 b) depicts the schemes of Eqn. (2.14) and (2.16). For the other two equations the picture is identical, only the state variables and the grids have to be swapped. This scheme can be applied to each facet and cell in the computational grid. This results in a system of linear equations, that can be rewritten into the so-called *Maxwell Grid Equations* (MGE), using matrix calculus:

$$\mathbf{C}\widehat{\mathbf{e}} = -\frac{d}{dt}\widehat{\hat{\mathbf{b}}} \tag{2.18}$$

$$\widetilde{\mathbf{C}}\widehat{\mathbf{h}} = \frac{d}{dt}\widehat{\hat{\mathbf{d}}} + \widehat{\hat{\mathbf{j}}} \tag{2.19}$$

$$\widetilde{\mathbf{S}}\widehat{\hat{\mathbf{d}}} = \mathbf{q} \tag{2.20}$$

$$\mathbf{S}\widehat{\hat{\mathbf{b}}} = 0. \tag{2.21}$$

In the Maxwell Grid Equations, the state variables are collected in vectors, while the topological operators $\mathbf{C}$, $\widetilde{\mathbf{C}}$, $\mathbf{S}$, $\widetilde{\mathbf{S}}$ that enforce the relations (2.14)-(2.17) are sparse matrices

with ± 1 and 0 as elements. The topological operators can be understood as the discrete counterparts of the continuous *curl* and *div* operators. The Maxwell Grid Equations exhibit a one-to-one analogy to the Maxwell equations in differential form. This should not be surprising, since the differential form of the Maxwell equations is obtained by applying (2.6)-(2.7) to infinitesimal facets and cells, which is actually the limiting case of the FIT. Furthermore, the topological operators retain some algebraic properties of their continuous counterparts that result in discrete laws of conservation, namely [38]:

- $\mathbf{C} = \widetilde{\mathbf{C}}^T \;\Rightarrow$ Time reversibility
- $\mathbf{C}\mathbf{S}^T = \widetilde{\mathbf{C}}\widetilde{\mathbf{S}}^T \;\Rightarrow$ Energy conservation
- $\mathbf{S}\mathbf{C} = 0$ and $\widetilde{\mathbf{S}}\widetilde{\mathbf{C}} = 0 \;\Rightarrow$ Electric and magnetic charge conservation

The FIT was originally formulated for coordinate grids, however, it can also be extended to non-orthogonal structured grids [39]. Up to this point no approximations have been applied, rendering the MGE exact for any mesh pair. Approximations are inevitably introduced by the discrete, constitutive material relations, that couple the fields to the fluxes:

$$\widehat{\widetilde{\mathbf{d}}} = \mathbf{M}_\varepsilon \widehat{\mathbf{e}} \tag{2.22}$$

$$\widehat{\widetilde{\mathbf{b}}} = \mathbf{M}_\mu \widehat{\mathbf{h}} \tag{2.23}$$

$$\widehat{\widetilde{\mathbf{j}}} = \mathbf{M}_\kappa \widehat{\mathbf{e}} \tag{2.24}$$

The matrices $\mathbf{M}_\varepsilon$, $\mathbf{M}_\mu$ and $\mathbf{M}_\kappa$ are called material matrices. They are constructed from a geometrical discretization of the material distribution in the computational domain. When orthogonal grids are used, as in this thesis, the material matrices become diagonal. Various other discretization schemes can be used for the construction of the material matrices [40, 41, 42]. However, for voxel based geometry data there is no need to apply sophisticated material discretization schemes and a simple staircase approximation will be used. Furthermore, the assignment of a grid cell to one tissue type allows to easily perform organ-wise evaluations of the calculated fields.

In the staircase approximation, the material is considered homogeneous inside each cell of the primary grid. The $\widehat{\mathbf{e}}$ component normal to the corresponding dual facet can strike four regions of different permittivity, as depicted in Fig. 2.6. The permittivity values of these four regions are averaged to one value, the averaged permittivity $\bar{\varepsilon}$:

$$\bar{\varepsilon} = \frac{\varepsilon_1 A_1 + \varepsilon_2 A_2 + \varepsilon_3 A_3 + \varepsilon_4 A_4}{A_1 + A_2 + A_3 + A_4}. \tag{2.25}$$

The same scheme can be applied to the conductivity:

$$\bar{\kappa} = \frac{\kappa_1 A_1 + \kappa_2 A_2 + \kappa_3 A_3 + \kappa_4 A_4}{A_1 + A_2 + A_3 + A_4}. \tag{2.26}$$

Collecting all averaged values in the diagonal of a matrix

$$\mathbf{D}_\varepsilon = Diag(\bar{\varepsilon}_\mathrm{x}(1), \ldots, \bar{\varepsilon}_\mathrm{x}(N_p),\ \bar{\varepsilon}_\mathrm{y}(1), \ldots, \bar{\varepsilon}_\mathrm{y}(N_p),\ \bar{\varepsilon}_\mathrm{z}(1), \ldots, \bar{\varepsilon}_\mathrm{z}(N_p)) \tag{2.27}$$

allows to denote the material matrices $\mathbf{M}_\varepsilon$ and $\mathbf{M}_\kappa$ as:

$$\mathbf{M}_\varepsilon = \tilde{\mathbf{D}}_A \mathbf{D}_\varepsilon \mathbf{D}_S^{-1} \tag{2.28}$$

$$\mathbf{M}_\kappa = \tilde{\mathbf{D}}_A \mathbf{D}_\kappa \mathbf{D}_S^{-1}. \tag{2.29}$$

Where $\tilde{\mathbf{D}}_A$ and $\mathbf{D}_S^{-1}$ are diagonal matrices, filled with the facet areas of the dual grid and inverse edge lengths of the primal grid, respectively. It is evident, that in the case of isotropic materials in the staircase approximation the material matrices are diagonal (for orthogonal grids). For the permeability, commonly a length averaging scheme along the primal grid edges is used. Since biological tissue is non-permeable, the length averaging is of lesser importance for this work.

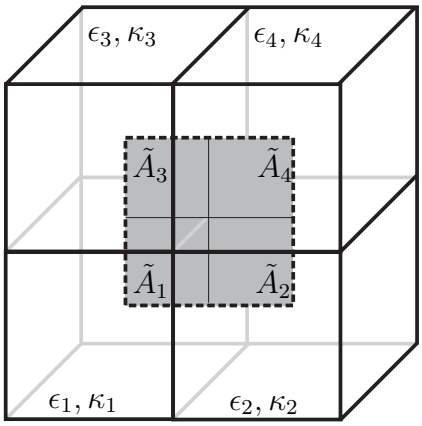

Figure 2.6: Averaging scheme for the conductivity and permittivity.

All field calculations presented in this thesis are performed in the frequency domain, assuming a harmonic time dependence. The time domain solutions can be obtained by means of a Fourier transformation:

$$f(t) = \Re\{\underline{f}\, e^{i\omega t}\}. \tag{2.30}$$

In the frequency domain, the time derivative of a quantity can be expressed by an algebraic multiplication of the complex amplitude with the factor $i\omega$. The time development of the induced currents during magnetic stimulation, presented in Sec. 4.2.3, have been obtained from a Fourier transformation applied as a post-processing step. No time integrator scheme was used.
In this section, only the basic features of the FIT were introduced. The formulations used for the actual calculations of fields inside the human body will be presented in the corresponding chapter: the electro quasi-static approach in Sec. 3.1 and the Ex-SPFD approach in Sec. 4.1.

2.3.2 Other Computational Methods

Throughout the last two decades, several numerical methods have been used for the calculation of low-frequency electromagnetic fields in the human body. In this section, an overview of these methods will be given, along with a brief performance comparison of these methods to the FIT.

Impedance Method

One of the first numerical methods applied to the calculation of low-frequency electromagnetic fields in the human body is the so-called Impedance Method. It was introduced by Gandhi in 1984 [43], based on the ideas of Armitage [44]. In this method, the biological body is represented by a three-dimensional network of impedances, aligned at the grid

edges, whose individual values are obtained from the complex conductivities $\kappa + i\omega\varepsilon$, for the various tissues in the body. For each loop around a facet, Kirchoff voltages are equated to the electromotive force produced by the magnetic field flux normal to the loop surface. The system of equations is solved using the successive over-relaxation (SOR) method. For each loop, the line currents or current densities in the direction of the three coordinates are computed. The impedance method has been extensively used for the calculation of induced currents originating from various low-frequency magnetic field exposure scenarios [45, 46, 47]. In a more general context, this method can be understood as a finite-difference discretization, based on impedances rather than the integral electric field as in the FIT. It requires to calculate three degrees of freedom for each cell, making it less effective than scalar potential based approaches. Furthermore, the SOR method used to solve the system of equations is quite outdated, resulting in very large computational time even for moderate model sizes.

Quasi-Static Finite-Difference Time-Domain Method

In the Finite-Difference Time-Domain (FDTD) method [48], Maxwell's curl equations are solved by directly modeling the propagation of waves into a volume of space containing the biological body. By repeatedly implementing a finite difference representation of the curl equations at each cell of the grid, the incident wave is tracked along with the interaction of the wave with the material. The time stepping is accomplished by an explicit scheme. In its classic form, FDTD at low frequencies leads to very large computational times due to the stability criterion for the time step. Moerloose et. al. have proposed an extension of the FDTD approach to quasi-static fields [49], in which two plane waves in opposite directions are used for excitation. Choosing two waves with the same amplitude, phase and polarization, the magnetic fields cancel out, resulting in an electric field excitation. Using waves of opposite phase, a magnetic field excitation can be achieved, since the electric fields cancel out. To avoid high-frequency contamination, a ramp function with a smooth start is used for the incident electric field. One of the essential factors for this method is the termination of the computational domain using special absorbing boundary conditions [50]. The method is restricted to cases where the characteristic wavelength and skin depth are much greater than the size of the structure under consideration. However, one serious drawback of this method is the restriction to model only conductive or displacement current, but not both simultaneously.

Scalar-Potential Finite-Difference Method

The Scalar-Potential Finite-Difference method has been proposed by Stuchly and Dawson in 1996 [51], for the use in low-frequency magnetic induction applications. It is based on a method previously published by Stevenson [52]. The applied finite-difference discretization is very similar to the one in the FIT. In this thesis, the SPFD approach is extended to handle arbitrarily shaped field sources and highly conductive material in the computational domain. Therefore, it will be described in more detail in Sec. 4.1.1. Exposure scenarios calculated using the SPFD approach can be found in [53, 54, 55, 56]. An comparison of results obtained using the SPFD approach and the impedance method was published in [57], while [58] provides a comparison of the SPFD approach and the quasi-static FDTD method.

Finite-Element Method

The Finite-Element Method (FEM) has emerged as a preferred numerical method in many application areas. The partial differential equations of an electromagnetic field problem are re-formulated into their variational or weak equivalents in the first step. Then, the

formulation is discretized in a finite dimensional space which is a subspace of the solution space of the weak formulation. Once a basis for the finite dimensional space has been chosen, the problem is solved by computing the appropriate coefficients for the chosen basis. Commonly piecewise linear basis functions are used, which are defined on a tetrahedral mesh that offers a very good approximation of complex geometries. The coefficients follow the solution of a linear system of equations. The resulting system of equations is also sparse as in the FIT. However, the number of non-zero elements is larger for a FEM matrix than for a FIT matrix. In cases, in which the same number of grid cells was used, the FEM matrix requires more memory to store. For most geometries this is not a problem, since the tetrahedral grid can approximate complex shapes more precisely than a hexahedral mesh. In the case of voxel data, however, the meshing of the computational domain is cumbersome and in case of extremely inhomogeneous material the method becomes less effective than a finite difference method. Nevertheless, the FEM method has been applied to various exposure scenarios [59, 60].

Hybrid Methods

Hybrid methods combine two known approaches for the solution of a given problem. In the case of low-frequency electromagnetic field computations, hybrid methods can be very efficient for problems in which a large surrounding space has to modeled, like e.g. a person standing below a high-voltage transmission line. Because the human body significantly alters the electric field distribution, a large volume has to be simulated, resulting in a very high number of needed grid cells, when using standard finite methods. In a hybrid approach, the fields in the surrounding space are calculated in a first step. Then, the induced charge density on the surface of the body is used as a source term for the second step, involving only the body [61, 62].

As can be concluded from the overview presented in this section, the FIT is very well suited for the calculation of electromagnetic fields in voxel-based, high-resolution human body models. The use of state-of-the art solvers and preconditioners for the solution of the systems of equations, along with an implementation on a parallel computer architecture, as presented in this thesis, allows to calculate electromagnetic fields inside the body with a so far not achieved spatial resolution.

Chapter 3

Electric Excitation

This chapter deals with systems that are excited electrically. In terms of this thesis, electrical excitation labels the contact of the body's surface to a potential difference, that will lead to a current flow between both contact points. In the following section, the electro quasi-static approach will be introduced. This is a (complex-valued) scalar-potential formulation, that is valid for the calculation of low-frequency electric fields. After the introduction of the used mathematical formulation, an estimation of the impact of the displacement currents on the calculated electric fields inside the body is carried out. This estimation is crucial for the rest of this work, since it decides whether the displacement currents can be neglected, allowing to calculate the electromagnetic fields from a real-valued system or whether the complex-valued formulation has to be used. In a complex-valued system the number of unknows is doubled, when compared to a real-valued one for the same spatial resolution. Furthermore, for real-valued systems more advanced solvers and preconditioners are available, making them the preferred choice, when the displacement currents can be neglected. In Sec. 3.3, a subgridding scheme for low-frequency applications based on Lagrange multipliers is presented. It allows to finely resolve a region of interest, while the computational grid in the surroundings is kept rather coarse. The scheme is validated on an analytic example and applied to a realistic exposure scenario. In the last section of this chapter, simulations of bioimpedance spectroscopy are presented. These simulations allow to compare calculated impedances to measured ones. Furthermore, an analysis of the distribution of the current densities inside the body during bioimpedance measurements is performed and a simple stylized phantom for use in bioimpedance calculations is proposed.

3.1 Electro Quasi-Static Formulation

In the low-frequency regime (here: $f < 1$ MHz), the electromagnetic wavelength is much larger than the dimensions of the human body. As a consequence, wave propagation phenomena can be neglected and the electric and magnetic field can be treated as uncoupled. In the electro quasi-static formulation, the magnetic field is assumed to be not time dependent: $\frac{\partial \vec{B}(\vec{r},t)}{\partial t} = 0$, resulting in an irrotational electric field. For irrotational fields a scalar potential approach can be used. The electric field is described by the gradient of a scalar potential:

$$\vec{E}(\vec{r},t) = -\nabla\varphi(\vec{r},t) \tag{3.1}$$

Applying the divergence operator to Eqn. (2.7) and interpreting the current purely conductive results in the time dependent electro quasi-static equation:

$$-\nabla \cdot \left(\frac{\partial}{\partial t}(\varepsilon \nabla \varphi(\vec{r}, t)) + \kappa \nabla \varphi(\vec{r}, t) \right) = 0. \tag{3.2}$$

In the frequency domain, the electric field is represented by complex-valued phasors, while the time derivative of a function can be obtained by an algebraic multiplication with the factor $i\omega$. Assuming linear materials, this yields:

$$-\nabla \cdot (\kappa + i\omega\varepsilon) \nabla \underline{\varphi}(\vec{r}, t) = 0. \tag{3.3}$$

When the displacement currents originating from the $i\omega\epsilon$ term can be neglected with respect to the conduction currents κ, Eqn. (3.3) reduces into a real-valued problem, as:

$$-\nabla \cdot \kappa \nabla \varphi(\vec{r}, t) = 0. \tag{3.4}$$

All the presented equations can be straightforwardly translated into the framework of the FIT. For (3.3) this results in:

$$\widetilde{\mathbf{S}} \left[\mathbf{M}_\kappa + i\omega \mathbf{M}_\varepsilon \right] \widetilde{\mathbf{S}}^T \underline{\phi} = \mathbf{q} \tag{3.5}$$

The vector $\mathbf{q}$ depicts the excitation of the system. This can be fixed potentials or charges in the computational domain. Eqn. (3.5) defines a linear system of equations, that has to be solved, in order to obtain the potential at each primary node of the computational domain. Basically, it is the balance equation of the electric flux densities for each grid cell, as described by the Gaussian law (2.8). The system matrix $\widetilde{\mathbf{S}}(\mathbf{M}_\kappa + i\omega\mathbf{M}_\varepsilon)\widetilde{\mathbf{S}}^T$ is sparse, with seven filled bands. It is symmetric and positive (semi-) definite. A typical sparsity pattern of such a system matrix is depicted in Fig. 3.1.

The finite computational domain of an electromagnetic field problem has to be enclosed by some special condition at the boundary of the domain, in order to model the surrounding space. Here, only conservative boundary conditions are used:

- Dirichlet boundaries. The Dirichlet boundary condition is the specification of a potential value at the boundaries of the computational domain.

- Neumann boundaries. The Neumann boundary condition is the specification of a value to the normal derivative of the potential at the boundaries of the computational domain.

In the electro quasi-static formulation, a homogeneous ($\frac{\partial \varphi}{\partial n} = 0$) Neumann boundary is called natural, since it is automatically employed when building the system matrix. For a Dirichlet boundary in the electro quasi-static formulation the system matrix has to be slightly modified. When only conductive currents are of interest, Eqn. (3.4) can be used. In this cases, the Neumann boundary condition is automatically applied to the surfaces of the conductors, rather then to the boundaries of the computational domain.

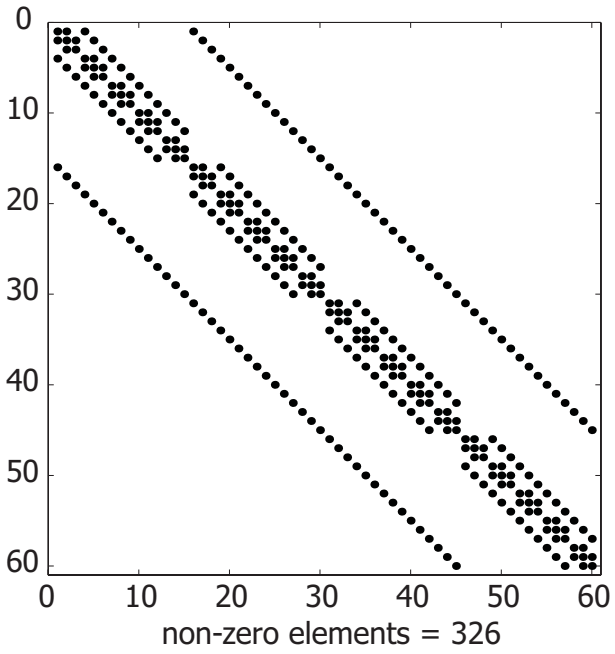

Figure 3.1: Sparsity pattern of a typical system matrix in the electro quasi-static formulation (nx=3, ny=5, nz=4).

3.2 Impact of the Displacement Current

In this section, an estimation of the impact of the displacement current on the magnitude of the calculated electric fields will be presented. In many publications concerning the calculations of low-frequency electromagnetic fields the displacement current is neglected, because the magnitude of the conductivity exceeds the effective permittivity (see below) by several orders of magnitude. While this is true for certain tissues, at extremely low frequencies and for, e.g. brain tissue, this assumption is far from being met. When the displacement current has to be explicitly considered, the complex-valued Eqn. (3.3) has to be solved, instead of to the real-valued Eqn. (3.4), in the case when only conductive currents are of interest. As will be shown at the end of this section, the time for the solution of a complex-valued system of equations, when compared to a real-valued one for the same grid resolution can be larger by a factor of three. Furthermore, a complex-valued system matrix requires double the memory of a real-valued one. This makes the choice of the right formulation not only crucial in terms of the computational time, but also in terms of achievable spatial resolution. The impact estimation is performed using a numerical example in which the current flows through the entire body.

In the frequency range from 10 Hz to 1 MHz, the relative permittivity values span over four orders of magnitude from 10^7 to 10^3 (Sec. 2.1). This is an unusual high value, since the highest relative permittivities of non-organic materials amount to approximately 4000. Due to these extremely high values, the term $\omega\varepsilon = \omega\varepsilon_r\varepsilon_0$ in Eqn. (3.3) is no longer negligible. From now on, this term will be referred to as the effective permittivity. At 50 Hz, in gray brain matter, κ equals to 0.075 S/m while the effective permittivity amounts to 0.034 S/m. It is clear, that for these values the displacement currents will not be negligible. Tab. 3.2 depicts the conductivity and effective permittivity values fore some selected tissues at 50 Hz. For most tissue types, the effective permittivity is indeed

substantially lower than the conductivity. However, due to the extreme inhomogeneity of the human body, a reliable error estimation, when omitting the displacement current cannot be obtained in a straightforward way.
For the error estimation, the current is injected into the model, by applying electrodes at the surface of the body. The electrodes are modeled by PEC (perfect electric conductor) patches, with fixed voltages. The model is standing on an electrode, with both feet touching the electrode, whereas the second electrode is located on top of the model's head. This results in a current flow along the coronal plane. The voltage difference between the two electrodes is U=2 V. The set-up is discretized with four different resolutions, ranging from 4 cm to 0.4 cm for the mesh step.

Table 3.1: Values of the conductivity κ and effective permittivity $\omega\varepsilon$ in S/m for selected tissues, as computed by the parametric Cole-Cole model at 50 Hz

Tissue type	κ / S/m	$\omega\varepsilon$ / S/m
Marrow	0.0016	0.0004
Fat tissue	0.0195	0.0004
Bones	0.0201	$2.4 \cdot 10^{-5}$
White matter	0.0533	0.0147
Eye	1.5000	$2.7 \cdot 10^{-7}$
Skeleton muscle	0.2333	0.0493
Blood	0.70000	$1.4 \cdot 10^{-5}$
Lung	0.2054	0.0024
Liver	0.0366	0.0050
Heart	0.0827	0.0240

Table 3.2: Global error of the electric field at various frequencies and model resolutions in %, for the case of neglecting the permittivity.

	model resolution			
Frequency / Hz	4.0 cm	2.0 cm	0.8 cm	0.4 cm
10	1.60	3.89	3.20	3.59
50	0.61	1.17	1.08	1.50
100	0.29	0.65	0.66	0.88
1000	0.35	0.48	0.28	1.33
10000	0.20	2.60	1.62	0.67
100000	0.06	0.78	0.92	0.55
1000000	2.50	1.41	1.19	1.45

All error estimations are performed on the computed electric fields inside the body. Using the real-valued formulation, electric fields can only be calculated inside the body, while in the case considering the displacement currents also fields in the surrounding space

are computed. Therefore, only the results calculated inside the body are compared, the fields in the surroundings are neglected. The errors are presented in the L_2-norm. Defining $\widehat{\mathbf{e}}_{\mathrm{diff}} = \widehat{\mathbf{e}}_{\mathrm{r}} - \widehat{\mathbf{e}}_{\mathrm{c}}$, the relative global error is calculated from

$$x = \sqrt{\frac{\widehat{\mathbf{e}}_{\mathrm{diff}}^T \cdot \widehat{\mathbf{e}}_{\mathrm{diff}}}{\widehat{\mathbf{e}}_{\mathrm{c}}^T \cdot \widehat{\mathbf{e}}_{\mathrm{c}}}}. \tag{3.6}$$

Here, $\widehat{\mathbf{e}}_{\mathrm{r}}$ denotes the electric field computed using only the conductivity, while $\widehat{\mathbf{e}}_{\mathrm{c}}$ denotes the electric field calculated using a complex-valued permittivity. In all performed simulations, a solver tolerance of 10^{-9} has been chosen. The global error x always remains below 5 %. It increases at both ends of the frequency range. In the low frequency regime, at 10 Hz and 50 Hz, this is due to the very high relative permittivity. On the other hand, at 1 MHz the factor ω contributes to a noticable increase of the displacement current.

Table 3.3: Evaluation of the error of the averaged electric field in % for selected organs at a resolution of 0.8 cm.

Tissue	10 Hz	50 Hz	100 Hz	1 kHz	10 kHz	100 kHz	1 MHz
Fat	1.91	0.28	0.10	0.00	0.14	0.16	0.59
Bones	1.50	0.80	0.50	0.10	0.18	0.19	0.62
White Matter	7.30	1.90	0.17	0.00	0.21	0.28	1.41
Gray Matter	11.10	3.50	0.68	0.09	0.36	0.35	1.68
Muscle	3.90	0.09	0.41	0.03	0.12	0.13	0.02
Lung	4.21	1.60	0.70	0.02	0.07	0.08	0.41
Liver	2.94	0.90	0.33	0.04	0.60	2.48	2.56
Spleen	1.18	0.40	0.16	0.01	0.00	0.74	4.03

Table 3.4: Evaluation of the error of the maximal electric field in % for selected organs at a resolution of 0.8 cm.

Tissue	10 Hz	50 Hz	100 Hz	1 kHz	10 kHz	100 kHz	1 MHz
Fat	1.55	1.00	1.30	1.37	6.62	2.49	1.58
Bones	2.90	2.30	1.17	1.49	7.42	5.88	1.44
White Matter	0.80	0.60	0.36	0.14	1.34	1.95	0.00
Gray Matter	1.10	0.09	0.19	0.19	3.18	7.68	0.70
Muscle	3.60	1.70	0.68	0.18	3.03	2.95	0.61
Lung	3.80	2.40	1.06	0.23	0.44	1.30	1.58
Liver	2.49	2.40	1.06	0.23	0.95	1.37	0.95
Spleen	3.57	2.80	1.62	0.20	0.49	0.28	0.93

A very common evaluation in dosimetric calculations is the analysis of the mean and maximal current densities in each organ separately. Particularly, the maximum computed electric field is an important quantity when comparing results to exposure restriction values. The errors of the averaged field are summarized in Tab. 3.3 and those of the maximal field values of each organ in Tab. 3.4. All errors of the averaged fields remain below 5 %, except for brain tissue at 10 Hz. This is expected, since the permittivity values of white and gray matter are an order of magnitude higher than those of other tissues. Aditionally, beacause the excitation electrode is located on top of the head, being partially immersed into head

tissue, staircasing errors can lead to very large fields in brain matter. The situation is very similar for the maximal field values. The error remains mostly below 5 % except at 10 kHz and 100 kHz. As expected, the error values for the maximal fields exhibit a larger variation than the averaged ones. Still, the order of magnitude of both errors is very similar.

Table 3.5: Calculation time in seconds and iteration count for the comparison of real-valued and complex-valued systems.

model data		real valued				complex	
		AMG		ILU		ILU	
resolution	# cells	iter	time / s	iter	time / s	iter	time / s
4 cm	10,200	8	0.03	39	0.15	44	0.41
2 cm	102,752	8	0.43	80	3.50	89	8.32
0.8 cm	1,019,424	9	4.35	187	79.12	270	239.40
0.4 cm	10,280,160	9	97.95	397	1660.00	540	4711.00

A comparison of the solution times for the real-valued and complex-valued problem at various resolutions is depicted in Tab. 3.5. All calculations were performed on a 64-Bit Intel Xeon 3.20 GHz machine, equipped with 12 GB RAM. For the iterative solution of the systems, the solvers contained in the PETSc (Portable, Extensible Toolkit for Scientific Computation) [63, 64] package were used. In the real-valued and complex-valued case the solution was obtained by a BiConjugate Gradient Stabilized (BiCGStab) method, along with an Incomplete LU (ILU) preconditioner. Additionally, to demonstrate the superior performance of multigrid in the real-valued case, an algebraic multigrid preconditioner (AMG) contained in the Hypre package [65] was used. For more information on the packages, see App. A. The solution times for the complex-valued system are larger by a factor of ≈ 3, than in the real valued case. At coarse resolutions, the iteration count is similar, while for large systems the ratio increases to 1.4. This can be explained by the increase in the condition number that automatically occurs for larger system matrices. This increase is not linear and it is more pronounced for the complex systems. Using a multigrid preconditioner reduces the solution times drastically: at coarse resolutions by a factor of eight, while for large systems the factor increases even to 18. The good performance of AMG for very large systems can be attributed to the optimal asymptotic complexity of multigrid methods (see App. A for further details). The implementation of an efficient multigrid code is very time consuming, therefore freely available software packages are used throughout this work. Unfortunately, at present time no complex-valued multigrid solvers were available to the author.
The estimation of the impact of the displacement current on the magnitude of the electric fields calculated inside the body showed, that the displacement currents may only become relevant at frequencies lower than 100 Hz. However, due to the uncertainties of the dielectric tissue data at very low frequencies and the fact that at higher frequencies the global and averaged error remain less than three percent, the real-valued formulation will be used throughout this work. The higher achievable spatial resolutions and the lower computational times of the real-valued approach prevail the accuracy loss due to the neglect of the displacement current.

3.3 Subgridding for the Electro Quasi-Static Formulation

A fine discretization of the whole body would result in a system of equations with several hundred millions of unknows. In chapter 4, this problem will be tackled by a more or less brute force approach, i.e. the implementation on a parallel computer architecture, which allows to exploit the resources of multiple workstations, simultaneously. In this section, a different approach has been chosen: a local subgridding scheme, in order to reduce the total number of unknowns, by finely resolving areas of particular interest, while keeping the rest of the computational domain coarsely resolved. In contrast to the finite elements method, in which a local grid refinement is straightforward and dependent on the performance of the used meshing tools,a dual orthogonal grid is needed for standard FIT. When an area of interest is resolved finely by a standard FIT grid, all regions below and above the finely resolved area have also to be discretized by this fine grid. Therefore, also regions of less interest are resolved finely, resulting in an unnecessary increase of the needed computational resources. In the work of Thoma [66] and Podebrad [67] subgridding was achieved by modifying the FIT, so that duality and orthogonality of the grids may be violated locally. In the here proposed approach, two different grids for the fine and coarse region are used, in which duality and orthogonality is satisfied. These grids are coupled by a condition enforcing the continuity of the potential at the interface of both grids. A bilinear interpolation is used in order to allow non-matching grid interfaces. In the following, the scheme will be derived for a electro static problem. It can be easily extended to the case of electro quasi-statics, by introducing a complex-valued permittivity. In the following, the subscript '$_\mathrm{c}$' denotes operators referring to the coarse grid, while '$_\mathrm{f}$' is used for the fine grid.

3.3.1 Saddle Point Formulation

The coupled system consisting of the fine and coarse grid will be formulated as a saddle point problem, allowing to obtain the potential distribution in both regions from the solution of one system of equations. For this task, the fine and coarse system matrices are collected into one system that is solved under the coupling condition. The coupling condition ensures the continuity of the potential at the planes, at which the coarse and fine grid have a common interface. Let $\mathbf{A}$ denote the system matrix in the according grid region as $\widetilde{\mathbf{S}}\mathbf{M}_\varepsilon\widetilde{\mathbf{S}}^T$, then both systems can be combined to one, yielding:

$$\begin{pmatrix} \mathbf{A}_\mathrm{c} & 0 \\ 0 & \mathbf{A}_\mathrm{f} \end{pmatrix} \begin{pmatrix} \tilde{\phi}_\mathrm{c} \\ \tilde{\phi}_\mathrm{f} \end{pmatrix} = \begin{pmatrix} \mathbf{b}_\mathrm{c} \\ \mathbf{b}_\mathrm{f} \end{pmatrix}. \tag{3.7}$$

In the above equation, the unknown potential values $\tilde{\phi}$ for each grid region and the excitation $\mathbf{b}$ on the right hand side are each collected in one vector. In order to select the primal grid nodes at the interface of the fine and coarse grid, a selection operator $\mathbf{Q}_\mathrm{f}^*$ for the fine grid and $\mathbf{Q}_\mathrm{c}$ for the coarse grid are used. Because the grid lines in the coarse and fine region do not have to coincide, an interpolation operator $\mathbf{B}$, that prolongates potential values from the coarse to the fine grid is also introduced. For more details on the interpolation operator and the needed modifications to the material matrices see the following Sec. 3.3.2. Using the both recently introduced operators, the interface condition can be

denoted as:

$$\mathbf{B}\mathbf{Q}_\mathrm{c}\tilde{\phi}_\mathrm{c} - \mathbf{Q}_\mathrm{f}^*\tilde{\phi}_\mathrm{f} = 0. \tag{3.8}$$

For a more convenient notation, the selection operator in the fine domain is rewritten as $\mathbf{Q}_f = -\mathbf{Q}_f^*$. Incorporating the interface condition into the system of equations (3.7) results in:

$$\begin{pmatrix} \mathbf{A}_\mathrm{c} & 0 \\ 0 & \mathbf{A}_\mathrm{f} \\ \mathbf{B}\mathbf{Q}_\mathrm{c} & \mathbf{Q}_\mathrm{f} \end{pmatrix} \begin{pmatrix} \tilde{\phi}_\mathrm{c} \\ \tilde{\phi}_\mathrm{f} \end{pmatrix} = \begin{pmatrix} \mathbf{b}_\mathrm{c} \\ \mathbf{b}_\mathrm{f} \\ 0 \end{pmatrix}. \tag{3.9}$$

In order to obtain a full coupling of both grids, the potential distribution in the fine region must also have an effect upon the coarse domain. For this purpose, the interpolation and selection operators from the fine to the coarse grid are introduced. Because of the duality of $\mathbf{Q}$ and $\mathbf{B}$ the transpose operators $\mathbf{Q}^T$ and $\mathbf{B}^T$ can be used for the restriction of the discrete charges from the fine to the coarse grid [68]. We finally obtain the symmetric system

$$\begin{pmatrix} \mathbf{A}_\mathrm{c} & 0 & \mathbf{Q}_\mathrm{c}^T\mathbf{B}^T \\ 0 & \mathbf{A}_\mathrm{f} & \mathbf{Q}_\mathrm{f}^T \\ \mathbf{B}\mathbf{Q}_\mathrm{c} & \mathbf{Q}_\mathrm{f} & 0 \end{pmatrix} \begin{pmatrix} \phi_\mathrm{c} \\ \phi_\mathrm{f} \\ \lambda \end{pmatrix} = \begin{pmatrix} \mathbf{b}_\mathrm{c} \\ \mathbf{b}_\mathrm{f} \\ 0 \end{pmatrix}. \tag{3.10}$$

This system corresponds to a Lagrange multiplier formulation, where the discrete surface charge variations at the fine grid side of the interface serve as Lagrange multipliers λ, see the next section for details. The coupled system preserves the sparsity and the structure of the coarse and fine system matrices. However, the introduction of Lagrange multipliers causes the system to become indefinite, even if positive definite system matrices are used.

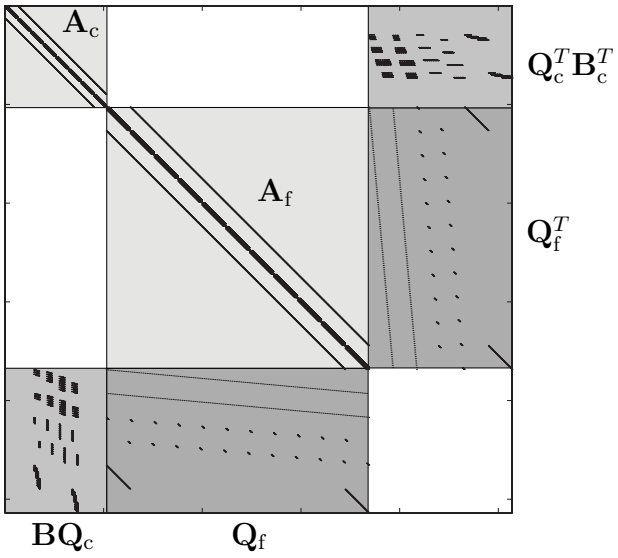

Figure 3.2: Sparsity pattern of a typical system matrix resulting from the subgridding approach.

The sparsity pattern of a typical system matrix constructed from Eqn. (3.10) is depicted in Fig. 3.2. In order to better visualize the various operators from which the matrix is assembled, gray rectangles have been underlaid. The here presented subgridding approach

can also be applied to more than two refinement levels. It would be possible to introduce a third region with an even finer resolution and couple the third domain to the region that has already been finely resolved. However, this case was not implemented and in the results section only a two-step refinement is presented.

3.3.2 Interpolation and Local Modifications

In this subsection, details of the interpolation and selection operators will be presented. Furthermore, the Lagrange multipliers introduced at the end of the last subsection will be physically interpreted as charges at the interface of both grids.
The selection operators $\mathbf{Q}_\mathrm{c}$ and $\mathbf{Q}_\mathrm{f}$ can be represented by sparse matrices, consisting only of 0 and 1 entries. They are constructed for each of the six interface planes separately. Care has to be taken for the nodes situated at the edges of the interface planes. Each node may only be selected once, otherwise the matrix will become overdetermined and no direct solution of the system can be obtained. In the existing implementation, $\mathbf{Q}_\mathrm{f}$ is assembled from the six operators at the interface planes, while $\mathbf{Q}_\mathrm{c}$ is constructed simultaneously with the interpolation operator $\mathbf{B}$.

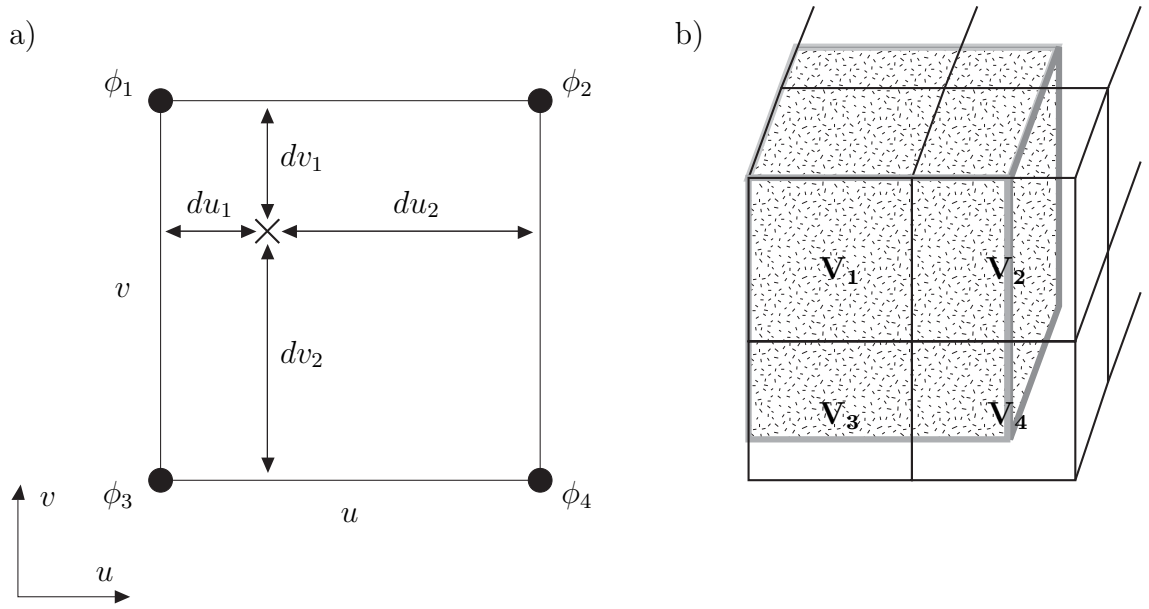

Figure 3.3: Interpolation schemes in the subgridding approach. a) Prolongation of the node based potential values. b) Restriction of volume based charges.

Fig. 3.3 a) visualizes the interpolation scheme from which the interpolation operator $\mathbf{B}$ is constructed, while part b) depicts the restriction of volume based quantities from a fine to a coarse grid. For the interpolation of the node based scalar potential values, a bilinear approach at the interface planes of the coarse and fine grid was used. The prolongation is performed at all six interface planes. However, since in the standard FIT the grid lines span over the complete computational domain, the edge lengths at two opposite planes are identical, leading to the same interpolation operator for these both interface planes. Therefore, only three interpolation operators have to be constructed. The opposite planes can still be distinguished by the selection operator $\mathbf{Q}_\mathrm{c}$. In bilinear interpolation, the potential values for each orthogonal grid direction can be interpolated separately. All

directions are commutative. For the point **X** in figure 3.3 a) this yields

$$\phi_x = \frac{du_2 dv_2}{uv}\phi_1 + \frac{du_1 dv_2}{uv}\phi_2 + \frac{du_2 dv_1}{uv}\phi_3 + \frac{du_1 dv_1}{uv}\phi_4. \tag{3.11}$$

The restriction of volume based quantities is drafted in part b) of Fig. 3.3. The restriction operator is constructed from weights $0 < w < 1$ acting on all fine grid volumes enclosed by the coarse volume, as indicated by the shaded region in Fig. 3.3. For a fine volume lying completely inside the coarse volume, $w = 1$. The weights for fine volumes lying only partially in the coarse volume are calculated as the fraction of the intersecting volume ΔV_f and the complete fine volume, as $w = \frac{\Delta V_f}{V_f}$. In the presented subgridding approach, the volume restriction operators act on the dual volumes, in which the discrete charges are allocated. To avoid discretization errors it is crucial that the dual volume of all cells in the fine grid has to match exactly with the complete dual volume of the coarse region. This is achieved by a displacement of the dual grid points situated at the boundaries in each grid and leads to a shortening of the dual grid edges and an adjustment of the volumes.

The coupling of both grids affects the balance equation of the electric fluxes for the grid cells at the interface. The Lagrange multipliers λ, introduced by the symmetrization of the system matrix play an important role in the coupling scheme. The balance equations of the electric fluxes for dual volumes situated at the interface of both grids, are augmented by a term containing the corresponding λ, multiplied with entries of the $\mathbf{Q}_\mathrm{c}^T\mathbf{B}^T$ operator for the coarse grid system matrix and the $\mathbf{Q}_\mathrm{f}$ operator for the fine grid system. In order to interpret the augmentation physically, the properties and the functionality of the Lagrange-multipliers λ and the restriction operator $\mathbf{B}^T$ have to be analyzed.

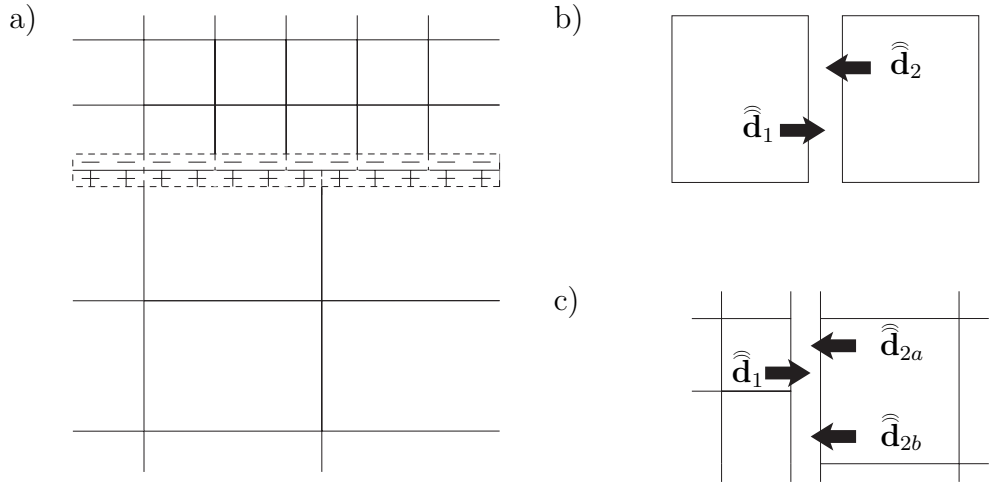

Figure 3.4: Details of the coupling. a) Interpretation of the Lagrange multipliers as surface charges. b) Flux balance in standard FIT. c) Flux balance at the interface of coarse and fine grid.

Due to the duality of the interpolation operators, $\mathbf{B}^T$ acts on dual volumes [68] as depicted in Fig. 3.3 b). However, because **B** was constructed for only a two-dimensional plane and not for a volume, the transposed operator acts as a restriction of infinitesimal volumes at the interface of both girds. This allows to interpret the Lagrange multipliers as surface charges at the fine grid side interface, while the interpolated multipliers $\mathbf{B}^T\lambda$ equal surface charges of opposite sign at the coarse grid side, as illustrated in Fig. 3.4 a). For

a correct coupling, the condition $\sum \lambda = \sum \mathbf{B}^T \lambda$ has to be satisfied, otherwise artificial, non-physical charges would be introduced at the interface. The additional contribution of the Lagrange multipliers to the balance equation of the electric fluxes inside a grid cell leads to a violation of Gauss law. For each dual volume, the sum of the six corresponding fluxes have to be equal to the enclosed charge, as $\sum_{i=1}^{6} \widehat{\widehat{\mathbf{d}}}_i = \mathbf{q}_{\tilde{V}}$. Solving this unmodified system results in a potential distribution that is distorted near the interfaces. It has to be ensured, that Gauss's law also holds for a combination of adjacent grid cells. In standard FIT, for two grid cells sharing a common dual facet the electric flux is conserved as depicted by Fig. 3.4 b). This is not the case at the interface of the coarse and fine grid. Here, the flux from the coarse grid facet has to be splitted into several fluxes at the fine grid side. This is illustrated by Fig. 3.4 c). It would be possible to interpolate the electric fluxes at the interface, this however would further complicate the proposed scheme. A much more elegant remedy for this problem is the removal of the coarse grid cells, that overlap with the fine grid region from the coarse system matrix $\mathbf{A}_c$. This is done by removing the corresponding rows from $\mathbf{A}_c$. After this modification, the coupling of both grids becomes unambiguously given by the Lagrange multipliers and Gaussian law is fulfilled again.

3.3.3 Results and Conclusions

In this section, the proposed scheme will be validated by comparing the calculated potential distribution to an analytic solution of a simple electro static example. Furthermore, the new method will be used for the calculation of the current densities in the hearth, when a power supply line with a voltage of 220 V is touched. The section ends with conclusions and some general remarks on the proposed scheme.

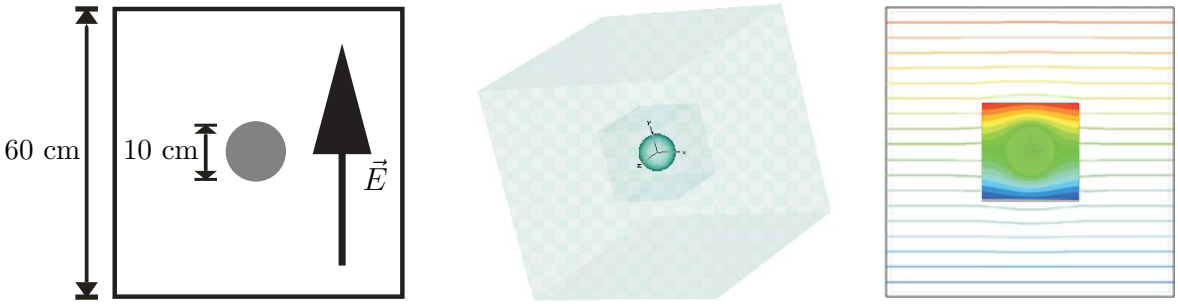

Figure 3.5: Validation example for the subgridding approach. a) Model dimensions b) Refinement regions c) Potential distribution.

For the validation of the proposed subgridding approach, a simple electro static example is used. A dielectric ball, with a relative permittivity of 100 and a radius of 10 cm is located inside the homogeneous electric field of a plate capacitor. The computational domain is a cube, with an edge length of 60 cm. The refinement region is situated around the center of the ball, with an edge length of 15 cm, see Fig. 3.5 a). The analytic solution of the potential distribution inside the dielectric ball in cylindrical coordinates is given by

$$\varphi_{\mathrm{i}}(r, \vartheta) = -\frac{3}{\varepsilon_{\mathrm{r}} + 2} E_0 \; r \; cos(\vartheta). \tag{3.12}$$

In the surrounding space the potential is described by

$$\varphi_{\mathrm{o}}(r,\vartheta) = E_0 \; cos(\vartheta) \left(\frac{\varepsilon_{\mathrm{r}} - 1}{\varepsilon_{\mathrm{r}} + 2} \frac{R^3}{r^2} - r \right). \tag{3.13}$$

In both equations, R denotes the radius of the ball, ε_{r} it's relative permittivity and E_0 the magnitude of the electric field. The equations are evaluated at each grid node and compared to the numerical solution. At this point it should be denoted, that the influence of the Neumann boundaries on the solution are also incorporated into the error estimation. However, due to the chosen dimension the influence is negligible, as can be concluded from the small error in the coarse domain. The maximum norm and the Euclidean norm of the error are calculated. For the convergence study, several spatial resolutions are used. Because the error is evaluated for the coarse and fine grid region separately, care is taken to keep the refinement ratio between the fine and coarse grid constant at all tested resolutions. Otherwise the influence of the coarse grid region on the fine grid domain can not be separated from the calculated errors. Because the ball in the center of the computational domain has only a small effect on the potential distribution in the coarse domain, the error in the coarse grid region remains less than 1 % at all resolutions. The relative error of the potential in the fine grid region at various resolutions, as estimated in maximum and euclidian norm is summarized in Tab 3.6.

Table 3.6: Error of the potential in % in the fine region, estimated in maximum and Euclidean norm. Ratio referrs to the refinement ratio of the fine and coarse grid.

resolution	max	euclidean	ratio
5.00 cm	31.06	14.38	2.00
2.50 cm	16.33	7.25	2.33
1.66 cm	14.00	5.26	2.22
1.11 cm	10.82	3.83	2.33
0.83 cm	8.20	2.84	2.40
0.71 cm	7.22	2.55	2.33
0.62 cm	6.10	2.08	2.38
0.55 cm	5.59	1.76	2.33

Plotting the estimated error versus the grid resolution in a double logarithmic plot, as in Fig. 3.6 allows to estimate the convergence order of the proposed method. From a least-squares fit of the estimated errors, a convergence of first order can be estimated. The discretization by standard FIT is expected to be between second and first order. The bilinear interpolation however, causes a consistency error at the interface, which only features first-order convergence. The numerical test shows, that the consistency error is dominating the convergence of the overall discretization error. Better interpolation methods for non-matching grids exist and have been reported in literature, like e.g. the mortar-element approach [69]. However, coupling methods with a second-order convergent consistency error are substantially more expensive than bilinear interpolation.

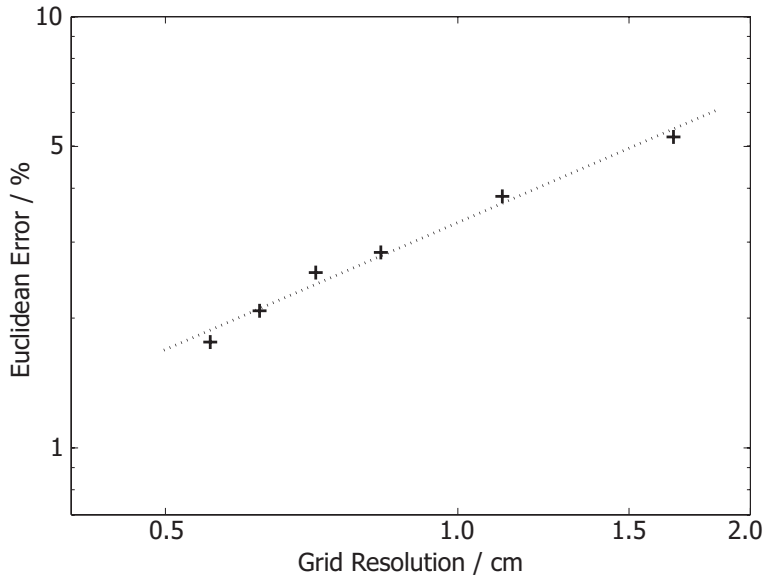

Figure 3.6: Convergence study for the presented subgridding approach. Relative error of the potential distribution in the fine grid region, estimated in Euclidean norm versus the grid resolution in a double logarithmic plot.

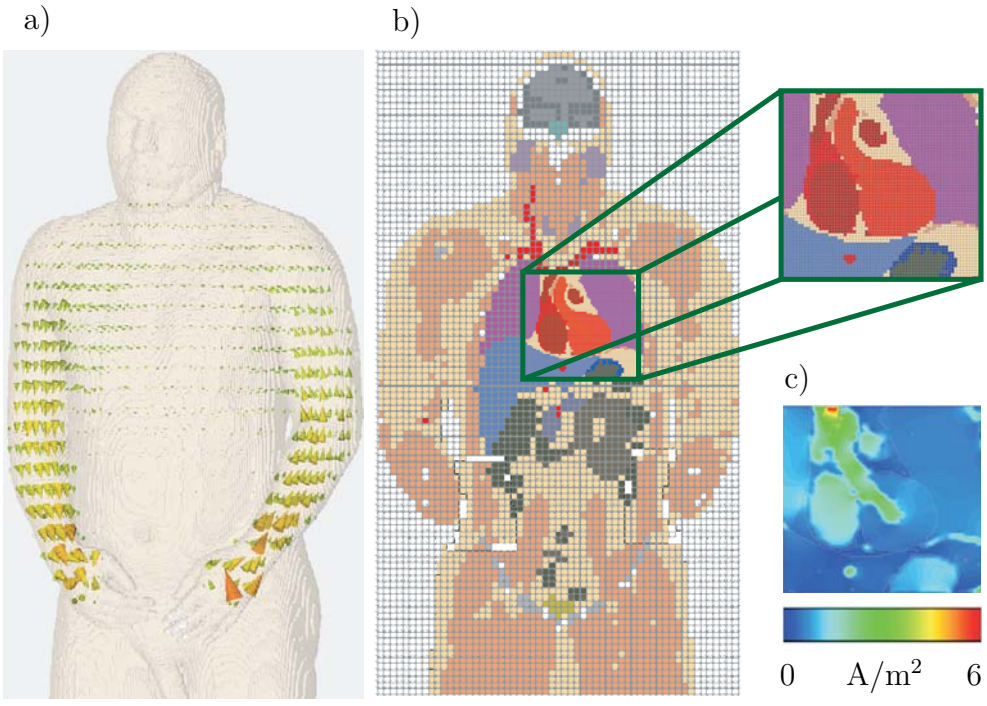

Figure 3.7: a) Plot of the current flow in the coarse model. b) Coarse and fine grid. c) Current density in the fine grid region.

Fig. 3.7 depicts the application of the proposed subgridding scheme to the calculation of current densities in the human body. In the presented example, the current densities occurring in the body when both hands are in contact to a potential difference of 230 V are calculated. Because in the original Visible Human model both arms are in electric contact with the legs, layers of insulating material have been added, in order to obtain a current flow through the arms from one hand to the other. The region of fine resolution is situated around the heart, see Fig. 3.7 b). The highest current densities flow through the hands and lower arms, with a maximal current density of 270 A/m^2 near the injection site. This very high value can be attributed to a staircasing error, that occurs due to a point-wise injection of the current. In the vicinity of the elbows, the current densities drop down to a value of 20 A/m^2. In the fine grid region around the heart, the maximal current density amounts to 8 A/m^2. Along with the tables presented in the introduction, this calculation confirms the well known fact, that the contact to a power line current can be life threatening.

In this section, a local grid refinement scheme based on a saddle point formulation was proposed. This scheme allows to finely resolve a particular area of interest in the computational domain, while keeping the grid in the surroundings at a coarse resolution. This approach however also exhibits some serious drawbacks. The introduction of the Lagrange multipliers leads to an indefinite system of equations, even with positive definite system matrices. For this types of systems, iterative solvers based on minimum residuals like MINRES or QMR can be employed. However, this type of solvers exhibits a far poorer performance than CG methods. A possible cure of this problems would be the incorporation of an adapted solution scheme, like the Schur complement formulation, the construction of a efficient preconditioner like proposed in [70] or the use of projected CG methods [71]. Still, due to the consistency error introduced by the bilinear interpolation, the efficiency of the entire scheme is not satisfactory. Therefore, this approach will not be used in the following, even it gained some popularity and has been lately extended to the case of magneto quasi-statics [72]. However, the system matrices in the magneto quasi-statics are inherently consistently singular. This fact, along with the disadvantages introduced by the coupling scheme make this newly proposed approach seem rather unsuited. In the next chapter, a fine spatial resolution in the calculations will be achieved by an implementation of the code on a parallel architecture.

3.4 Simulations of Bioimpedance Spectroscopy

After introducing a new approach for the improvement of the spatial resolution in the last section, an application example will be presented in this section. Bioimpedance spectroscopy labels the measurement of the complex-valued resistance of biological tissue at various frequencies. This method was first used in a clinical environment by Thomasset in the 1960s [73]. It is used as a low-cost, easy to use and non-invasive approach to estimate various body parameters. Because of the capacitive properties of the cell and other body membranes, the measured body impedance is higher at lower frequencies (Sec. 2.1). By measuring the impedance at various selected frequencies, it is possible to estimate the balance between intracellular (ICF $\approx$ 55 %) and extracellular fluids (ECF $\approx$ 45 %). This balance plays an important role in renal dialysis, where the blood not only has to be cleansed, but also excess fluid has to be removed from the body. A dehydration performed too fast can lead to headache, nausea or even to a shock. Up to now, the dehydration velocity was mostly based on the experience of the medical doctor. Latterly, bioimpedance

spectroscopy offers the possibility to non-invasively control the balance of ECF and ICF during dialysis. Furthermore, because fat tissue exhibits a lower admittivity than muscles, bioimpedance measurements allow to estimate the muscle and fat masses of the measured person [74]. This information is of importance in dietetic treatment and allows to monitor the state of health of nutritionally disturbed patients. In this case, simplified devices performing only single frequency measurements are commonly used. Most prominent in this sector are the widely available fat scales. However, in the commercially availiable scales the electrodes are located at both feet leading to a currentflow through the legs only and not the entire body. Therefore, the accuracy specifications given by manufacturers which can be as fine as 0.1 % should clearly be mistrust.
The simulation of bioimpedance measurements is very valuable in several views. It allows to compare simulation results directly to measurements, that were performed on living subjects. Such application set-ups are quite rare but very important, since they allow to estimate the accuracy of the modeling detail of the simulation. For the measurements, two probands from our institute were selected, that match best to the body shape of the Visible Human. However, as it will be pointed out in Sec. 3.4.2, some differences among the model and the probands were unavoidable. Furthermore, the simulations will be compared to results from empirically derived equations. The simulations also allow to gain insight into the distribution of the current among the various tissue types, that cannot be accessed by measurements. Furthermore, the sensitivity of the current distribution with respect to the tissue conductivities can be performed, allowing to estimate the impact of the uncertainties in the dielectric data onto the current distribution.

3.4.1 Simulation Results

For the measurement of the whole-body impedance, commonly four electrodes are used. Two for the injection of the current and two for the measurement of the voltage. In most cases they are attached to the ankle and the wrist, resulting in a current flow through the leg, torso and arm. The distance between the injection and measurement electrode has to be chosen large enough to allow the current to spread in the tissue. Empirical analysis showed, that this is already the case after some cm. Since we are interested in the impedance values calculated using the body model and the dielectric data, the following approach was chosen in order obtain a homogeneous current distribution shortly after the injection and to reduce the electrode effect: Near the injection site the ends of the limbs are cut off perpendicular to the direction of the current flow. Several slices of good conducting material that represents the electrode are attached to the cut plane. The current is injected into two points inside the electrode material. This approach ensures a fast spread of the injected current and allows to reliably calculate the impedance already at a short distance to the injection site.

For the simulations, the body is divided into three sections, that are simulated separately. This is, the leg from the ankle up to the torso, the torso starting at the upper thigh and the arm from the shoulder to the wrist. The sections have been selected with some overlap, allowing to combine the impedance calculations. This separation allows to simulate each section at a higher spatial resolution. Furthermore, in the Visible Human model, the hands and lower arms are touching the torso. For the simulations, this electric connection has to be removed. The calculations were performed on a 3 GHz Pentium IV machine, equipped with 2 GB RAM. Due to memory restrictions, the largest system size

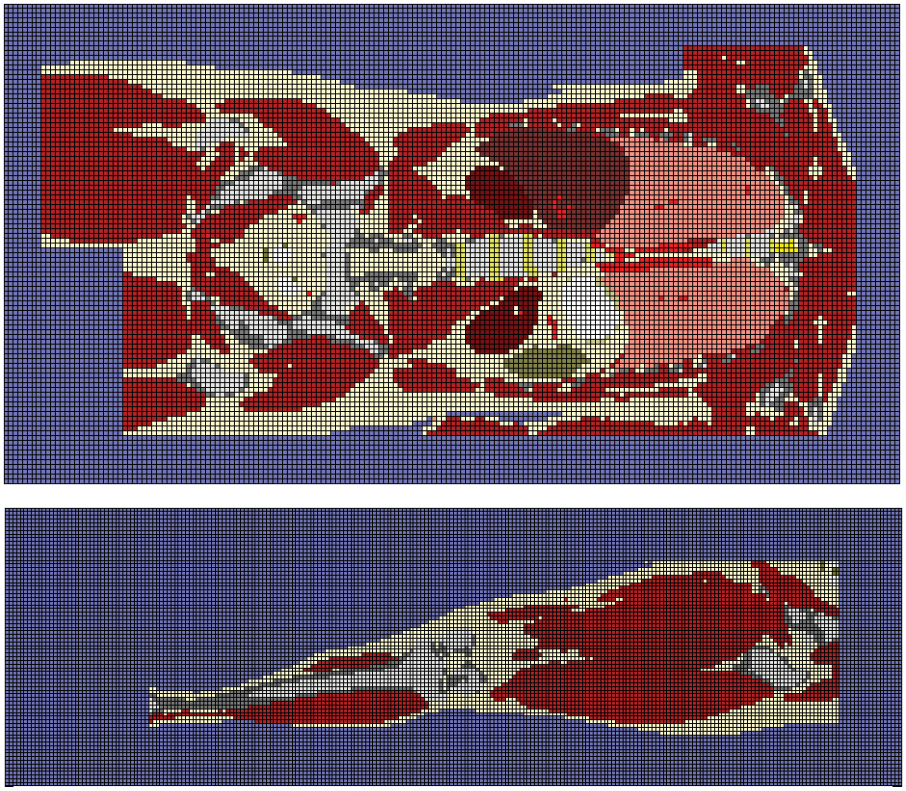

Figure 3.8: Slices through the tissue distribution in the leg and torso section at the actual computational resolution.

amount to approximately 1.5 million complex-valued unknowns. In the leg and arm region, a resolution of 4.5 mm was applied while in the torso, because of the larger size of this section a slightly coarser grid of 5 mm was used. See Fig. 3.8 for slice plots of the tissue. The impedance is calculated for each slice perpendicular to the direction of the current flow. A cross-check of the total current in each slice is performed. For the calculation of the impedance at each slice, the potential at the point carrying the largest current is used. This allows to estimate the impedance along the main current path, but sometimes produces discontinuities. Hence, also an interpolated curve is added to the plots. In the background of each plot, a drawing of the calculated body part depicts the connection of the impedance curve and the anatomy. The presented impedance values of the three segments were calculated at 50 kHz. This type of impedance calculation is only valid when the current flow is perpendicular to the slices. In a more rigorous analysis, it would be necessary to cut the tissue distribution at each slice and add electrodes to the second surface. This would however result in the need for more than 150 different models the leg section only. Fig. 3.13 depicts the direction of the current flow and the equipotential lines in the leg section, confirming the validity of the assumptions made for the calculation of the impedance. Minor deviation occurs only in the vicinity of the knee. In the other sections, some deviation can be found near the shoulder and at the lower arms.

Fig. 3.9 depicts the calculated resistance and reactance in the leg section. In the upper thigh, the resistance exhibits a linear increase. Here, the tissue composition and cross section is nearly identical for each layer, resulting in a very similar increase of the resistance at each layer. In the vicinity of the knee, the slope of the resistance curve is

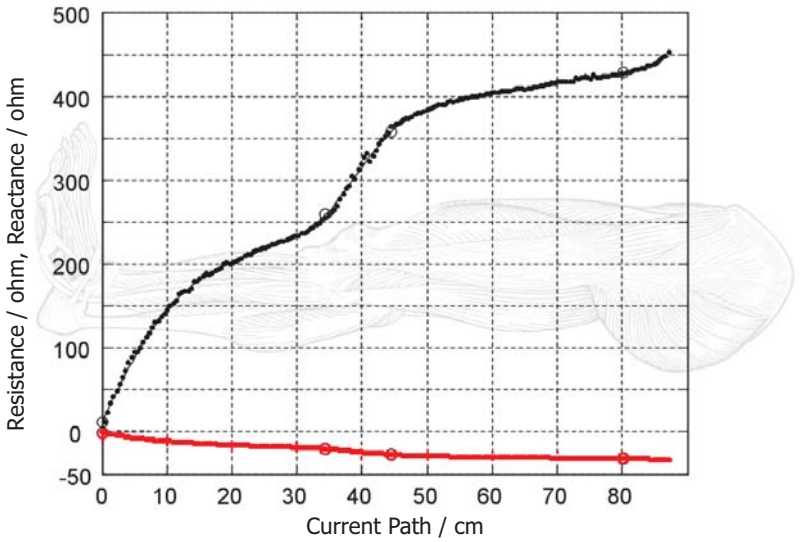

Figure 3.9: Calculated resistance (black line) and reactance (red line) in the leg section.

clearly higher than in the upper and lower leg. This is due to the narrowed cross section and the absence of muscle in the knee region, since muscle tissue exhibits the highest conductivity value, see Tab. 3.7. In the lower leg, a gradual increase of the resistance from the ankle up to the middle of the shin results from a change of the legs cross section in this region. From the middle of the shin up to the knee, the increase becomes linear as in the thigh region.

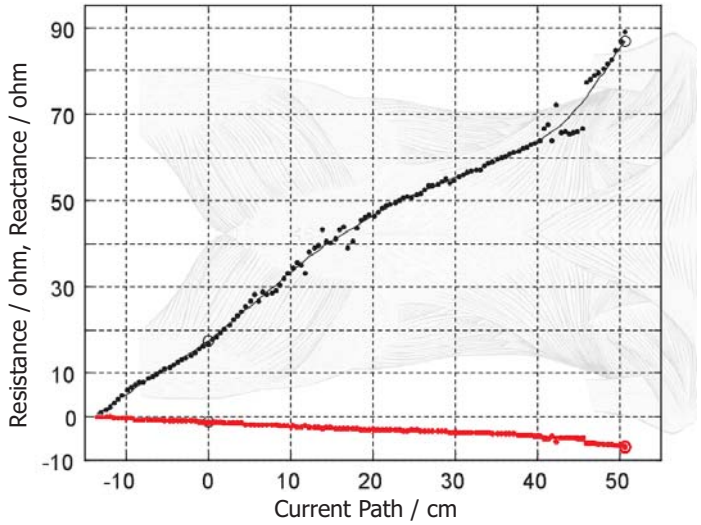

Figure 3.10: Calculated resistance (black line) and reactance (red line) in the torso section.

The calculated resistance and reactance in the torso section is plotted in Fig. 3.10. In this section, the current spreads among the various tissues and organs, resulting in a more or less linear increase, without any characteristic marks. Furthermore the overall total resistance is lower than 100 Ω, which is noticeable less then for the leg ($\approx$ 450 Ω), or the arm ($\approx$ 350 Ω). Thus, the contribution of the torso to the whole-body impedance is of minor importance.

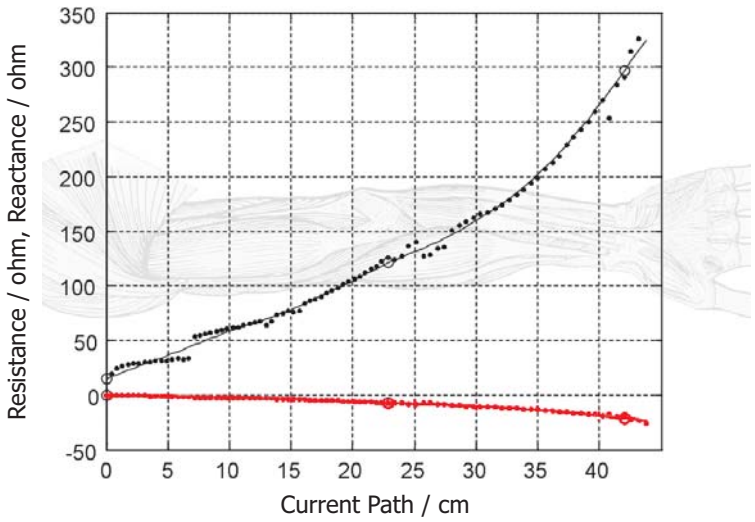

Figure 3.11: Calculated resistance (black line) and reactance (red line) in the arm section.

A plot of the calculated resistance and reactance in the arm section is depicted in Fig. 3.11. In the Visible Human model, the lower arm is bent at an angle of approximately 30 degrees from the elbow downwards. Therefore, the estimated impedance values have to be corrected, resulting in a slightly larger layer thickness, as can be seen by the larger distance of the data points in the lower arm. The resistance in the lower arm exhibits a similar behavior, as in the lower leg. A gradual increase found in the region where the limbs cross section narrows. Contrary to the knee, no change of the slope can be observed in the vicinity of the elbow. This can be explained by the presence of large muscles like the brachialis, the triceps brachii, the anconaeus and the supinator all covering the joint. In the upper arm the resistance increase is almost linear due to a constant cross section and tissue composition.

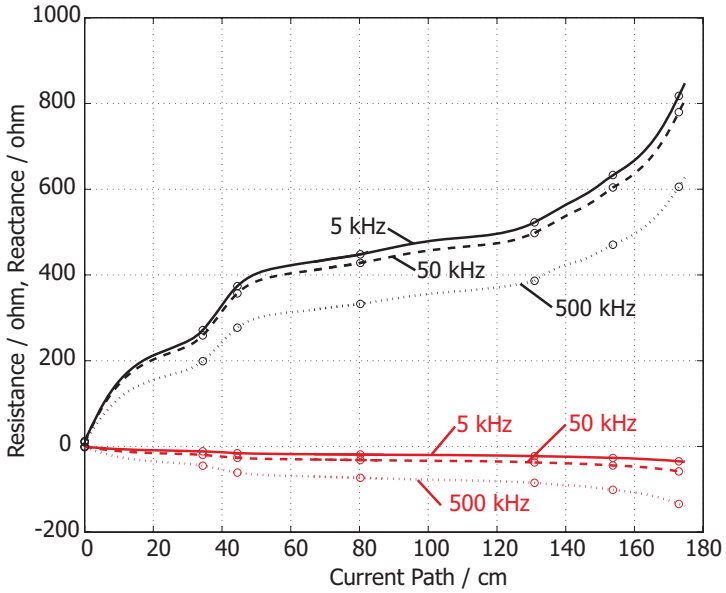

Figure 3.12: Calculated resistance of the whole body at various frequencies. Full line 5 kHz, dashed line 50 kHz, dotted line 500 kHz

The three sections can be combined in order to obtain the impedance curve of the whole-body as depicted by Fig. 3.12. In the plot of the combined impedance the leg section ranges from 0 cm to 80 cm, the torso from 80 cm to 130 cm and the arm from 130 cm to 170 cm. The open circles represent reference points, as depicted by Fig. 3.15. They are used to compare the measurements and simulations in the next section. As expected, the increase of the conductivity at higher frequencies results in lower resistance values. The shape of the curves at the various frequencies remains very similar. Thus, the change of the frequency of the current does not affect the analysis presented above.

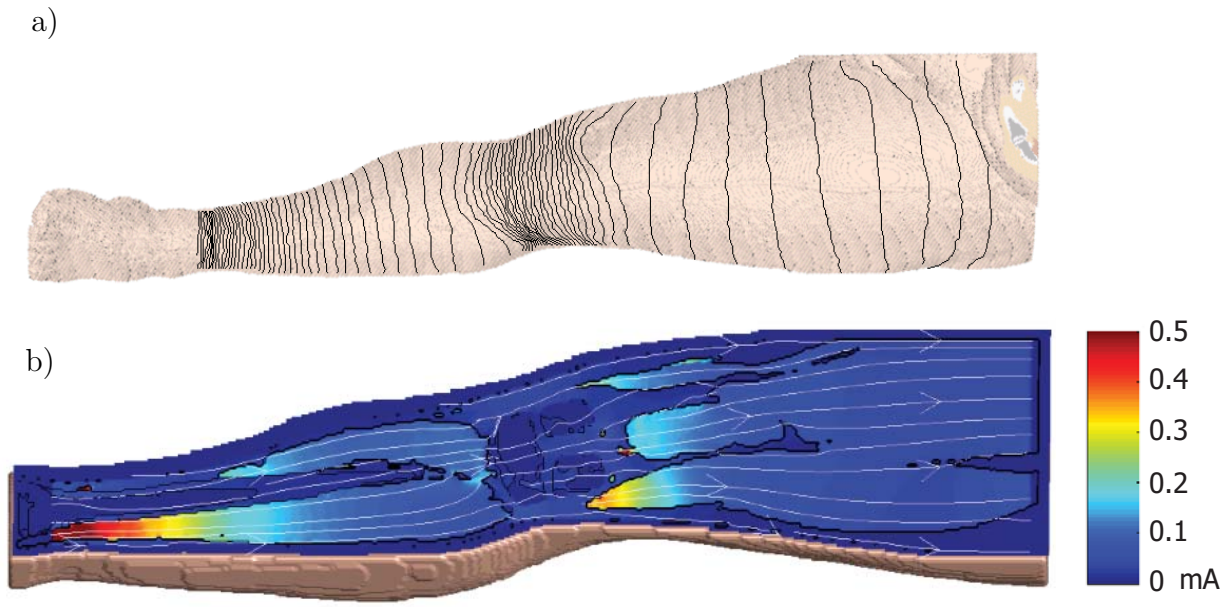

Figure 3.13: a) Equipotential lines on the surface of the leg section. b) Current in the leg section, calculated at 50 kHz for an injection current of 0.5 mA. White arrows depict the direction of the currentflow.

The simulations of bioimpedance spectroscopy not only allow to calculate the impedance values for each slice of the body, but also offer the possibility to analyze the distribution of the current among the various tissue types. Fig. 3.13 depicts the distribution of the current in a cross section of the leg. In the analysis of the three segments, the development of the impedance curves was strongly connected to the tissue composition of each layer. The sharp impedance increase in the knee region was interpreted by a narrowed cross-section of the leg and the absence of well conducting muscle tissue in this region. The plot in Fig. 3.13 further supports the second conclusion, as it is evident that muscle tissue carries the largest fraction of the current. The current distribution presented in Fig. 3.13 was obtained at 50 kHz, the conclusions however hold for all simulated frequencies from 5 kHz up to 1 MHz. As already pointed out in the discussion of the impedance curves at various frequencies (Fig. 3.12), the absolute values of the impedance change with the frequency. However, the shape of the impedance curves and the distribution of the current among the various tissues do not alter significantly. This is also the case inside the torso, where the total number of various tissue types involved in the conduction process is larger than in the limbs. Therefore, we conclude that the frequency dependence of the impedance occurs mainly due to a change of the tissues conductivity and not due to a re-distribution of the current among the various tissues.

Table 3.7: Tissue composition of the leg and conductivity values at 50 kHz.

Tissue type	fraction / %	conductivity at 50 kHz / S/m
Muscle	60.9	0.3518
Fat	31.9	0.0242
Marrow	03.9	0.0031
Bone	03.2	0.0206
Skin	00.7	0.0002
Blood	00.2	0.7008

In order to further elaborate the distribution of the current among the various tissues, a sensitivity analysis was performed. The conductivity values of fat and muscle tissue were calculated as usually using the model by Gabriel (Sec. 2.1) at 50 kHz and then varied by $\pm$ 50 %, at 5 % intervalls. Since little informations could be obtained from the reactance curves, the calculations in the sensivity analysis are carried our using only the conductivity. The analysis was performed in the leg section using a grid resolution of 2.5 mm. The tissue composition in the calculation domain and the non-modified conductivity values are presented in Tab. 3.7. Already from the absolute values of the conductivity it is evident, that muscle tissue will carry the largest fraction of the current, since it is the dominant tissue type and exhibits a conductivty that is larger by an order of magnitude than the conductivty of fat tissue.

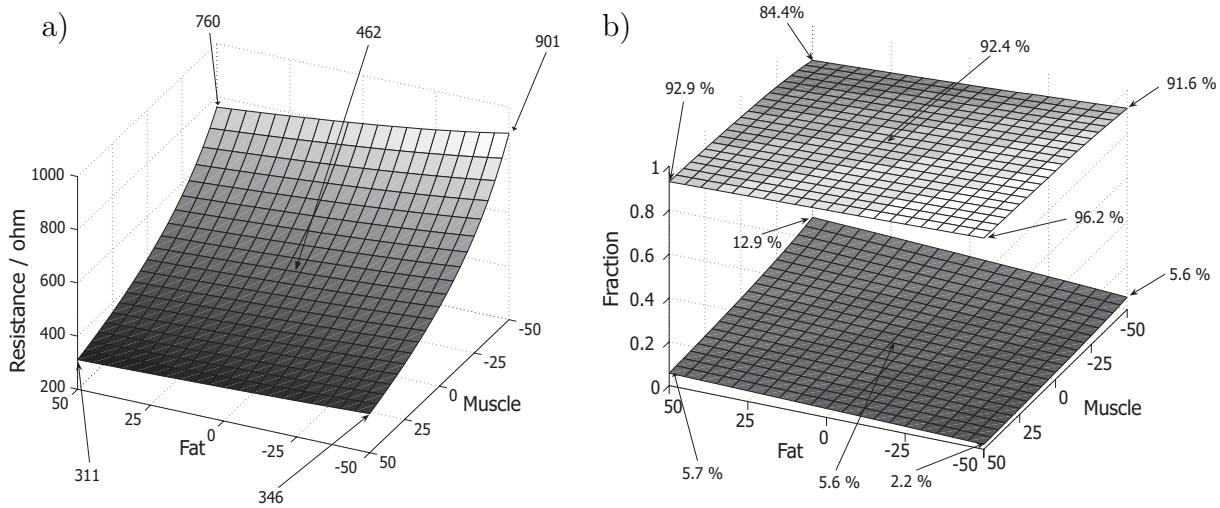

Figure 3.14: Results of the sensitivity analysis. a) Resistance of the leg section. b) Distribution of the current in muscle (upper plane) and fat (lower plane) tissue. The numbers on the x- and y- axis denote the variation of to the conductivity.

The results of the sensitivity analysis are summarized in Fig. 3.14. Part a) depicts the calculated impedance values for the leg section, while the spread of the current among the fat and muscle tissue is illustrated in part b). For the case of non-modified conductivity, the impedance amounts to 462 Ω, with muscle tissue carrying 92.4 % and fat tissue 5.6 %

of the total current. Only in the extreme cases in which the muscle conductivity is modified to very low values and the fat conductivity is very high, the current fraction carried by muscle tissue falls below 90 %. Assuming an accuracy of 25 % for the conductivities, as rated by Gabriel *et al.* (Sec. 2.1), it can be concluded that more than 90 % of the current flow in the leg will take place in muscle tissue.

3.4.2 Comparison of Measurements and Simulations

For a comparison of the results obtained from the simulations to measurements two colleagues from our institute were selected as probands. The measurements were performed with instruments produced by *Xitron Technologies*[1]. One injection electrode was placed at the ankle, the second one at the wrist. In order to obtain whole-body and segmental impedances, eight measurement electrodes were used, as depicted by Fig. 3.15 a). The following measurements were performed:

- whole-body (electrode 1→8)
- several leg segments (electrode 1→2, 1→3, 1→4, 1→5, 1→6)
- hip to shoulder (electrode 6→7)
- entire arm (electrode 7→8).

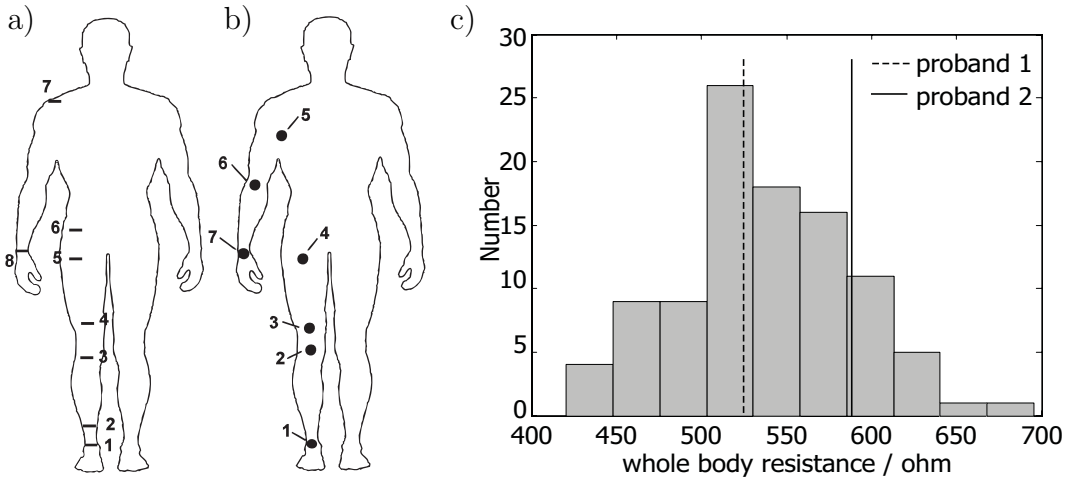

Figure 3.15: a) Electrode positions in the measurements. b) Reference points in the simulations. c) Measured whole-body resistance of both probands compared to a population of 100 males with a body height > 180 cm and a body weight > 90 kg.

The two selected probands were chosen to best match to the body shape of the Visible Human model. However, this was only partially successful as pointed out by Tab. 3.8. In case of the Visible Human, the data presented in Tab. 3.8 was obtained from a summation of the corresponding voxels in the 1 mm phantom. In the case of both probands, the whole-body measurement was evaluated using standard clinical software supplied with the measurement set-up. In oder to evaluate the quality of the measurements, the whole-body impedances of both probands are compared to a population of 100 males with a body

[1]HYDRA 4200 ECF/ICF Bioimpedance Analyser

height larger than 180 cm and a weight of more than 90 kg, see Fig. 3.15 c). The data set of the population was collected and kindly made available to the author by the *Fresenius Medical Care* company. The measured impedance values of both probands fall very well into the population data, confirming a good quality of the measurements. Still, the fat mass and fat ratios differ noticeably among the model and the probands. However, due to a lack of further suitable probands for the measurements, the measurement data will be compared to the simulations in the following.

Table 3.8: Various body parameters of the model and both probands.

	Visible Human	Proband 1	Proband 2
Height / cm	180.3	192.0	199.0
Weight / kg	90.3	93.2	103.2
Muscle mass / kg	35.3	52.2	48.8
Muscle ratio / %	39.2	56.0	47.3
Fat mass / kg	33.8	17.1	27.4
Fat ratio / %	37.5	14.6	23.3

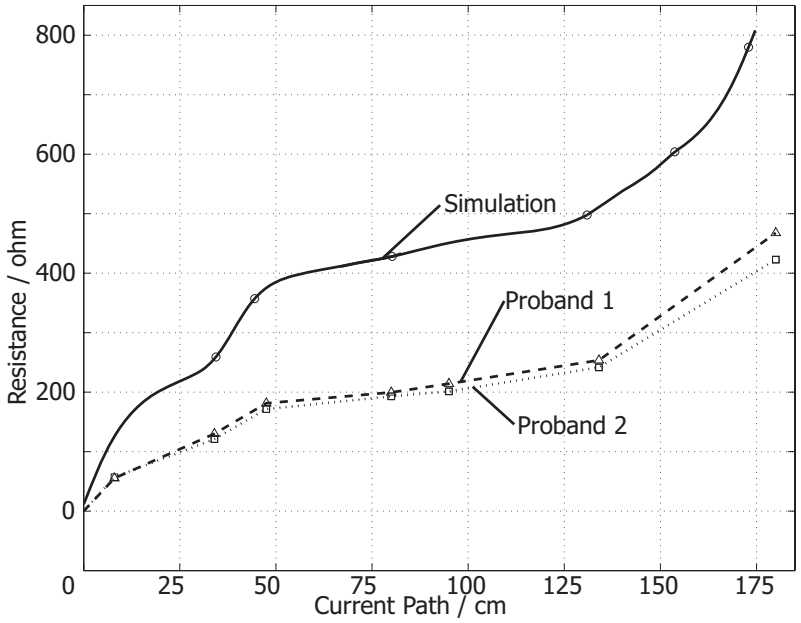

Figure 3.16: Comparison of the measured and simulated resistances. Full line depicts the simulated resistance, dashed and dotted line the measured values for both probands, respectively.

A comparison of the measured and simulated impedances is plotted in Fig. 3.16. The full line depicts the simulated impedance, while the dashed and dotted lines represent values obtained from the measurements on both probands, respectively. The markers on the curves represent reference points, as depicted by Fig. 3.15 a) and b). Both measured curves exhibit a very good agreement. However, the curve obtained from the simulations

differs in the absolute values from the measured curves by a factor of 1.5 to 2. Nevertheless, the form of the simulated and measured curves agree very well. As in the simulated curve, also in the measured curves an increase of the slope in the knee region and at the transition from the torso to the arm section can be observed. The deviation of the absolute values can be mainly attributed to the differences of the fat mass among the probands and the model. Still, the calculated whole-body impedance of the model lies inside the values of the measured 100 person population as presented in Fig. 3.15 c). Therefore, also a natural variation of the body impedance can contribute to the deviation of the simulated and measured values.

In the last part of this section, the simulated impedances are compared to results calculated by empirical formula, that have been obtained from fits to measured data of large proband populations. For the calculation of the fat-free mass from the impedance measurement using Xitron devices the following formula is used [75]:

$$FFM = -4.104 + \left(0.518 \cdot \frac{height^2}{\mathrm{m}} \cdot \frac{resistance}{\Omega}\right) + \left(0.231 \cdot \frac{weight}{\mathrm{kg}}\right) + \left(0.130 \cdot \frac{reactance}{\Omega}\right) + (4.229 \cdot sex), \tag{3.14}$$

where $sex = 1$ for men and 0 for women. The total fat mass is computed by $weight - FFM$ (Tab. 3.8). Applying this formula to the data obtained from the simulations (resistance= 770 Ω, reactance= 60 Ω), a fat mass of 39.4 kg is estimated for the Visible Human. This value is 16 % larger than the fat mass calculated from the voxel-ratios multiplied by the total weight as presented in Tab. 3.8. Based on the work of Segal [76], Pichard *et al.* have presented a modified formula for the calculation of the fat-free mass in overweight persons [77]. For the Visible Human a Body Mass Index (BMI) of 27.78 kg/m^2 was estimated. For a BMI >26 kg/m^2 the formula propsed by Pichard reads

$$FFM = 14.5244 + \left(0.000886 \cdot \frac{height^2}{\mathrm{m}}\right) - \left(0.02299 \cdot \frac{resistance}{\Omega}\right) + \left(0.42688 \cdot \frac{weight}{\mathrm{kg}}\right) - \left(0.07002 \cdot \frac{age}{\mathrm{a}}\right). \tag{3.15}$$

Using this equation a fat mass of 28.3 kg is calculated from the simulation results, 16 % less than the voxel-based evaluation.

Although the comparison of the absolute impedance values from simulations and measurements revealed some discrepancies, the overall quality of the simulations turned out to be satisfactory. The shape of the calculated impedance curves agrees well with the anatomical details of the model. Furthermore, it was possible to estimate the distribution of the current among the various tissues and perform a sensitivity analysis in terms of the tissue conductivity. In order to increase the modeling accuracy and allow further conclusions, future work on this topic should aim at a better compatibility of models and probands.

3.4.3 Simple Stylized Phantom for Segmental Impedance Calculations

In the last section dealing with bioimpedance simulations a simple body phantom for the calculation of segmental body impedances is presented. It is intended as an easy-to

use model, that allows to quickly estimate the segmental impedances without the need for sophisticated software. In the simulation results, six different sections in which the impedance exhibits a characteristic behavior can be distinguished. This is the lower leg, the knee, the upper leg, the torso, the upper arm and the lower arm. The sections in which the impedance is linear are modeled by homogeneous cylinders. In the lower limbs, where the impedance is increasing gradually, homogeneous cut-off cones are used. An overview of the sections is depicted in Fig. 3.17 a).

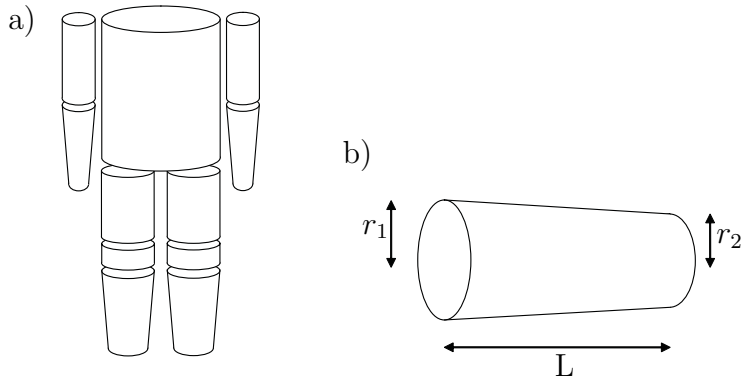

Figure 3.17: a) Simple phantom for the calculation of segmental impedances constructed from cylinders and cut-off cones. b) Geometry of a cut-off cone.

The resistance of a cylinder with the length L and a radius r is given by:

$$R_{\text{cyl}} = \frac{\rho L}{\pi r^2}, \tag{3.16}$$

where ρ is the specific resistivity of the material. The geometry of a cut-off cone is drafted in Fig. 3.17 b). Its resistance can be calculated using:

$$R_{\text{cone}}(l) = \frac{\rho L}{\pi(r_1 - r_2)} \left[\left(r_1 + \frac{r_2 - r_1}{L} \cdot l \right)^{-1} - \frac{1}{r_1} \right], 0 \leq l \leq L. \tag{3.17}$$

In case of the full cut-off cone this simplifies to

$$R_{\text{cone}} = \frac{\rho L}{\pi r_1 r_2}. \tag{3.18}$$

In order to fit the resistance values of the simple phantom to the simulation results, the geometry and conductivity of each section have to be estimated. This is done in several steps:

- L is measured.
- The resistance of the complete section R is obtained from the simulated curve.
- Cylinder: r is measured.
  Cone: The averaged radius $r_{av} = \sqrt{r_1 r_2}$ is measured, r_1 and r_2 are varied for an optimal fit.
- For the cylinders, ρ can be obtained from $\rho = \frac{\pi R r^2}{L}$, for the cones $\rho = \frac{\pi R r_1 r_2}{L}$ is used.

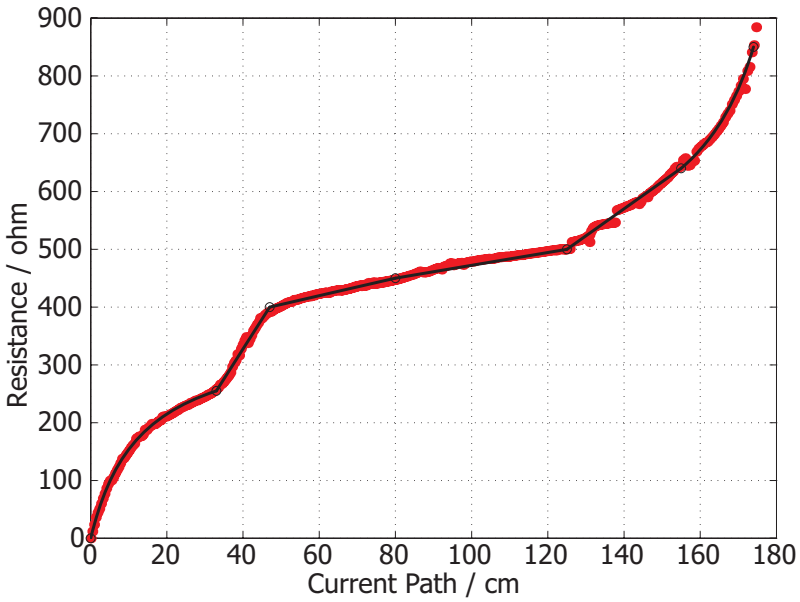

Figure 3.18: Comparison of the simulated impedances (red circles) to values obtained with the simple stylized phantom (dark line).

Tab. 3.9 summarizes the geometry and conductivity data for the six sections of the simple phantom obtained to fit the simulation data at 50 kHz. A comparison of the impedances estimated by the simulations and by the simple phantom is presented in Fig. 3.18. Red circles represent simulation data, the dark line depicts results obtained from the phantom. The resistance values calculated using the simple phantom agree very well with the results from simulation data, confirming the validity of the simple model. Even in the lower limbs, where the impedance increases gradually the agreement is excellent. The modeling using cut-off cones in this sections represents a more realistic approach than only using cylinders for the phantom.

Table 3.9: Parameters for the simple phantom at 50 kHz.

Segment	Type	L /cm	r_1 / cm	r_2 / cm	R / Ω	ρ / Ωm
lower leg	cone	33	2.25	7.84	255	4.28
knee	cylinder	14	7.00	7.00	145	15.94
upper leg	cylinder	33	9.00	9.00	50	3.86
torso	cylinder	45	25.00	25.00	50	21.83
upper arm	cylinder	30	3.50	3.50	135	1.73
lower arm	cone	20	3.50	1.79	215	2.11

Chapter 4

Magnetic Excitation

The exposure of the human body to a low-frequency magnetic field results in an eddy current distribution in the weakly conductive tissue. The induction of currents represents the cardinal interaction mechanism of low-frequency magnetic fields and tissue, labeled as magnetic excitation in this work. In this chapter, a new and efficient approach for the calculation of these currents will be presented. The new approach is a two-step algorithm, that combines the advantages of two well-known methods into one, namely the Scalar-Potential Finite-Differences (SPFD) method and the curl-curl approach. After introducing both methods at the beginning of the next chapter, they will be combined to the new, so-called Extended SPFD (Ex-SPFD) approach. This approach will be extensively tested and validated for several models at various frequencies and also for the case of highly conductive material in the computational domain, for which the classical SPFD method fails. After the validation, an alternative way to calculate the magnetic vector potential in the first step of the Ex-SPFD approach will be presented. The alternative way is based on a vector Poisson system, instead of the curl-curl equation and further accelerates the calculations, particularly in the case of very large systems, consisting of more than a hundred million unknowns. Systems of this size are solved in the application section of this chapter. Two application examples will be given. The first example is a dosimetric study of the body exposed to the magnetic field of an electric blanket. The blanket represents a fully three dimensional source of the magnetic field, which can not be modeled by the classical SPFD approach. Two possible wiring types will be examined, confirming the need for a realistic modeling of the magnetic field sources. Second, the calculation of currents induced in the brain during Transcranial Magnetic Stimulation (TMS) is presented. In a TMS treatment, the stimulation coil is excited by short current pulses. Since for transient pulses the time-harmonic solution is no longer valid, the time development of the induced currents will be calculated using a Fourier decomposition. From this calculations, the impact of the β-conductivity dispersion on the magnitude of the induced currents will be estimated. The last subsection of this chapter presents the simulations of a mapping study of the motor cortex. In a mapping study, the stimulation coil is positioned at various selected points at the surface of the head and the response in the motor cortex eliciting due to the applied magnetic field is measured as potentials in the hand muscles. The measured response will be compared to the calculated fields in the motor cortex.

4.1 Calculation of Induced Currents

4.1.1 Scalar-Potential Finite-Differences (SPFD) Approach

The SPFD approach was proposed by Stuchly and Dawson for the calculation of induced currents in the human body [51]. The approach is valid in the case when the eddy current losses are relatively small and do not significantly alter the magnetic source field. In this case, the currents can be calculated using a scalar potential. Starting with an additive decomposition of the potential into a rotational part represented by the vector potential $\underline{\vec{A}}_0$ and an irrotational part represented by the gradient of a scalar potential $\nabla\psi$, the electric field in the frequency domain can be expressed by

$$\underline{\vec{E}} = -i\omega(\underline{\vec{A}}_0 + \nabla\underline{\psi}). \tag{4.1}$$

The magnetic field can be calculated by applying the curl operator to the vector potential, as

$$\underline{\vec{B}}_0 = \nabla \times \underline{\vec{A}}_0. \tag{4.2}$$

The continuity equation expresses the conservation of the net current over a surface with a loss or gain of charge within the surface. In frequency domain this yields

$$\nabla \cdot \underline{\vec{J}} + i\omega\rho = 0. \tag{4.3}$$

Since no net charge is present in the cases considered here, the time derivative can be omitted. Furthermore, the current can be rewritten using Ohm's law, as

$$\nabla \cdot \underline{\vec{J}} = \nabla \cdot (\kappa\underline{\vec{E}}) = 0. \tag{4.4}$$

Inserting Eqn. (4.1) into (4.4) results in

$$-\nabla \cdot (\kappa\nabla\underline{\psi}) = \nabla \cdot (\kappa\underline{\vec{A}}_0). \tag{4.5}$$

This is the main equation of the SPFD approach that has to be solved inside the conductor. The induced currents can then be obtained from Ohm's law:

$$\underline{\vec{J}}_{\mathrm{ind}} = \kappa\underline{\vec{E}} = -i\omega\kappa(\underline{\vec{A}}_0 + \nabla\underline{\psi}). \tag{4.6}$$

The SPFD equation can be easily formulated in the framework of the FIT, as

$$\widetilde{\mathbf{S}}\mathbf{M}_{\kappa}\widetilde{\mathbf{S}}^T\underline{\psi} = \widetilde{\mathbf{S}}\mathbf{M}_{\kappa}\underline{\widehat{\mathbf{a}}}_0. \tag{4.7}$$

The system matrix is identical to the matrices in the electro quasi-static formulation (Eqn. 3.5), when the displacement current can be neglected. The incorporation of the displacement current is straightforward by using a complex permittivity. However, in the original formulation by Stuchly the problem was formulated without the displacement current and therefore the author has adopted this derivation. The same boundary conditions as in the electro quasi-static can be used, see Sec. 3.1. The main difference of the SPFD approach and the electro quasi-static equation, is the excitation of the system on the right-hand side of the corresponding equation. While in the electro quasi-static case the excitation consists of potentials or charges, in the SPFD approach the divergence of the vector potential multiplied with the conductivity is used on the right-hand side. The subscript 0

points out that the vector potential is an external quantity, that has to be known inside the computational domain. This fact limits the field sources to ones that are known analytically or semi-analytically, which is a serious drawback, since analytical solutions are only available for a very limited number of geometries. Furthermore, because the vector potential is treated as an external quantity, the shielding effects of conductive material on the magnetic field can not be modeled using the SPFD approach. The neglect of shielding effects is well justified in the case of the human body, where the conductivities are fairly low [51]. However, this disallows the presence of highly conductive material, like metallic implants, in the computational domain. The main advantage of the SPFD approach is its efficiency. Contrary to the curl-curl equation, which will be introduced in the next section, only a scalar-valued system has to be solved. Furthermore, the system matrix is symmetric and positive (semi-)definite, two features from which the performance of iterative solvers can greatly benefit.

4.1.2 Curl-Curl Equation

The curl-curl equation represents a more general approach for the calculation of the induced currents, than the SPFD method. It can be derived directly from Maxwell's equations, without incorporating any approximations. Faraday's law of induction (2.6) and Ampére's law (2.7) in the frequency domain can be rearranged to yield

$$\underline{\vec{B}} = \frac{i}{\omega}\nabla \times \underline{\vec{E}}\ ; \tag{4.8}$$

$$\nabla \times \underline{\vec{H}} - i\omega\underline{\vec{D}} - \underline{\vec{J}} = 0. \tag{4.9}$$

Using the material relation

$$\underline{\vec{H}} = \mu^{-1}\underline{\vec{B}}\ , \tag{4.10}$$

the magnetic component can be eliminated by inserting Eqn. (4.8) into (4.9), resulting in

$$\nabla \times \left(\mu^{-1}\frac{i}{\omega}\nabla \times \underline{\vec{E}}\right) - i\omega\underline{\vec{D}} - \underline{\vec{J}} = 0. \tag{4.11}$$

Denoting the source current as $\underline{\vec{J}}_s$, along with

$$\underline{\vec{J}} = \kappa\underline{\vec{E}} \tag{4.12}$$

$$\underline{\vec{D}} = \varepsilon\underline{\vec{E}} \tag{4.13}$$

results in the curl-curl equation

$$\left[\nabla \times \mu^{-1}\nabla \times + i\omega\kappa - \omega^2\varepsilon\right]\underline{\vec{E}} = -i\omega\underline{\vec{J}}_s, \tag{4.14}$$

formulated in terms of the electric field. As in the SPFD approach, the induced currents are calculated using Ohm's law

$$\underline{\vec{J}}_{\text{ind}} = \kappa\underline{\vec{E}}. \tag{4.15}$$

The transition into the framework of the FIT is straightforward and yields

$$\left[\widetilde{\mathbf{C}}\mathbf{M}_\nu\mathbf{C} + i\omega\mathbf{M}_\kappa - \omega^2\mathbf{M}_\varepsilon\right]\widehat{\mathbf{e}} = -i\omega\widehat{\widehat{\mathbf{j}}}_s. \tag{4.16}$$

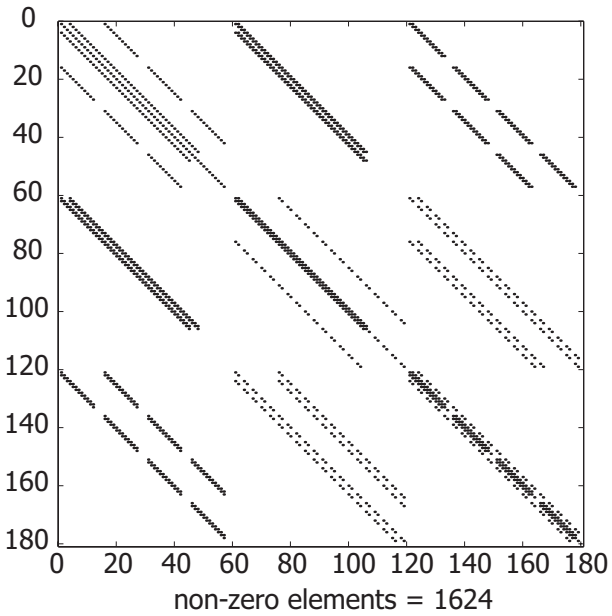

Figure 4.1: Sparsity pattern of a typical curl-curl system matrix. (nx=3, ny=5, nz=4)

Here, $\mathbf{M}_\nu$ denotes the material matrix of the inverse permeability $\nu = \mu^{-1}$. Since no approximations have been used for the derivation, the curl-curl equation is valid in the entire frequency range, allowing the calculation of wave propagation phenomena as well as problems in the magneto quasi-static case.

The sparsity pattern of a typical curl-curl system matrix is depicted in Fig. 4.1. Since the electric field is a vector, each field component represents one degree of freedom (dof). Therefore, the size of the curl-curl system matrix is three times the number of grid cells. The curl-curl stencil results in 13 filled diagonals. Commonly, two types of boundary conditions are used. Electric boundaries label the setting of the tangential component of the electric field to zero. The natural boundaries of the curl-curl equation are called magnetic, labeling a zero tangential magnetic field at the borders of the computational domain. As pointed out in Sec. 3.2, the displacement current can be neglected. Therefore, the term $\omega^2\mathbf{M}_\varepsilon$ will be omitted from now on. In case of conductive parts present in the computational domain, the system matrix becomes complex-valued symmetric, otherwise it is real-valued. Since the application of the curl operator onto a pure gradient field yields zero, the null-space of the curl-curl operator will contain discrete gradient fields corresponding to the non-conductive regions. Hence, the system is consistently singular. Effort has been undertaken to regularize the system matrix using tree-cotree condensation techniques as described in [78]. However, this regularization leads to a severe deterioration of the condition number of the system matrix [79]. An alternative, and more suitable way is the use of a discrete div-grad augmentation as proposed in [80]. For the solution of consistently singular systems, it has to be ensured that the excitation current on the right hand side is free of divergence, otherwise the system becomes unsolvable. In the FIT, this can be achieved by using closed current paths, which exactly match the grid. This approach was implemented in the software used in this thesis. If a spatially extended current source has to be modeled, a divergence correction has to be applied to the source current, prior to the solution of the curl-curl system. The accuracy of the divergence correction becomes the limit to the highest available solution accuracy of the curl-curl system.

Using the curl-curl equation, contrary to the SPFD approach, arbitrarily shaped field sources can be considered. Furthermore, also the shielding effect of the induced currents on the magnetic field is included. However, this generality has to be paid with faint efficiency. For the same spatial resolution, a three times larger system has to be solved than in the SPFD approach. Additionally, the curl-curl system is complex-valued, further increasing the computational time. For the case of low-conductive materials, like the human body even more numerical disadvantages arise. Consider a computational domain discretized with a resolution of 5 mm, containing no permeable material. Then, the magnitude of the entries in the $\widetilde{\mathbf{C}}\mathbf{M}_\nu\mathbf{C}$ operator will be in the order of $\approx 10^8$. For a conductivity of 0.1 S/m at 50 Hz the magnitude of the $i\omega\mathbf{M}_\kappa$ term is ≈ 0.1. This large contrast of the terms in the curl-curl equation leads to the problem, that a very high accuracy of the iterative solver (i.e. low relative residuum) is needed, in order to obtain reliable results for the induced currents. If the relative residuum was chosen too high, then the calculated induced currents will in fact only reflect numerical noise. A high solver accuracy leads to large computational times and can even result in the breakdown of the Krylov solver, when the chosen relative residuum is of similar magnitude as the accuracy used to represent the numbers in memory (e.g. 10^{-15} for double precision). The presence of permeable material in the computational domain further increases the contrast. For higher frequencies, the contrast decreases. The effect of this contrast on the computational time will be further discussed in the next section.

4.1.3 Extended-SPFD (Ex-SPFD) Approach

The proposed Ex-SPFD approach is a two step algorithm, that combines the advantages of the curl-curl equation and the SPFD approach. The basic idea is to calculate an approximate magnetic vector $\widehat{\underline{\mathbf{a}}}_{\text{app}}$ potential by solving the curl-curl Eqn. (4.16) with a fairly low accuracy in the first step of the algorithm. This approximate vector potential already describes the magnetic field distribution very well, but does yet not satisfy the continuity Eqn. (4.4). In the second step, the approximate vector potential is used on the right hand side of the SPFD Eqn. (4.7). From the solution of this system, a scalar correction potential $\underline{\psi}_{\text{corr}}$ is obtained. This step can be understood as a divergence correction applied to the approximate vector potential calculated in the first step. The induced currents are then obtained from the approximate vector potential minus the gradient of the correction potential. Summarizing the Ex-SPFD approach:

1. Solve
$$\left[\widetilde{\mathbf{C}}\mathbf{M}_\nu\mathbf{C} + i\omega\mathbf{M}_\kappa\right]\widehat{\mathbf{e}} = -i\omega\widehat{\underline{\mathbf{j}}}_s.$$
with a fairly low solver accuracy in order to obtain an approximate vector potential $\widehat{\underline{\mathbf{a}}}_{\text{app}} = \frac{i}{\omega}\widehat{\mathbf{e}}$.

2. Calculate the correction potential (divergence correction) by solving
$$\widetilde{\mathbf{S}}\mathbf{M}_\kappa\widetilde{\mathbf{S}}^T\underline{\psi}_{\text{corr}} = \widetilde{\mathbf{S}}\mathbf{M}_\kappa\widehat{\underline{\mathbf{a}}}_{\text{app}}.$$

3. Correct the approximate potential
$$\widehat{\underline{\mathbf{a}}} = \widehat{\underline{\mathbf{a}}}_{\text{app}} - \widetilde{\mathbf{S}}^T\underline{\psi}_{\text{corr}}.$$

4. Calculate the induced currents from

$$\underline{\hat{\mathbf{j}}}_{\text{ind}} = -i\omega \mathbf{M}_{\kappa} \underline{\hat{\mathbf{a}}}.$$

Validation

In the following, the Ex-SPFD approach will be validated for various scenarios. Furthermore, the shielding effect of the induced currents on the magnetic field will be analyzed. Because the Ex-SPFD approach works best for the case of low-conductive highly inhomogeneous materials, the presented calculations has been performed directly on the human body model. A comparison of the SPFD approach to an analytical test-case can be found in [51].

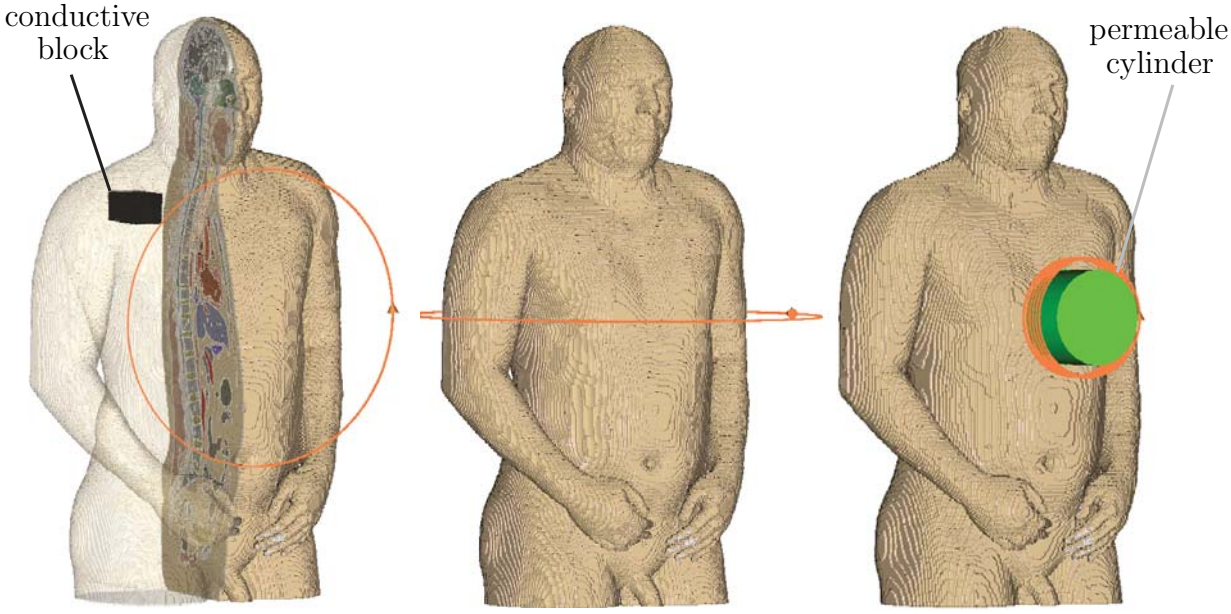

Figure 4.2: Models used for the validation of the Ex-SPFD approach.

The various models used for the validation of the Ex-SPFD approach are depicted in Fig. 4.2. All models consist of the upper body part of the Visible Human. In model 1 (left), the excitation is performed by one circular current path in front of the breast. In this model, a highly conductive block can be inserted into the right shoulder. This block can be e.g. the model of a metallic implant. Here, it is used for the validation of Ex-SPFD, when highly conductive material is present in the computational domain. Model 2 (center), is excited by a circular current path spun around the body at breast hight. The third model (right) is used for the validation of cases, in which also permeable material has to be modeled. The excitation consists of six circular paths forming a small coil that is filled with a permeable cylinder. All models have been meshed with a resolution of ≈ 1 cm, corresponding to $\approx 300{,}000$ grid cells. The exact numbers will be presented for each validation example. As a reference for all error estimations presented in the following, the solution of the curl-curl equation with the highest in double arithmetic available solver accuracy of 10^{-15} is used. This is well justified, since no approximations has been used for the derivation of the curl-curl equation from Maxwell's equations. The global error is presented in the relative L_2 norm, whereas the point-wise error is given in the maximum

norm. Defining $\underline{\hat{\hat{\mathbf{j}}}}_{\mathrm{err}} = \underline{\hat{\hat{\mathbf{j}}}}_{\mathrm{ref}} - \underline{\hat{\hat{\mathbf{j}}}}$, the relative global error x, the relative point-wise error x_{p} and the divergence x_{div} are given by

$$x = \sqrt{\frac{\underline{\hat{\hat{\mathbf{j}}}}_{\mathrm{err}}^T \underline{\hat{\hat{\mathbf{j}}}}_{\mathrm{err}}}{\underline{\hat{\hat{\mathbf{j}}}}_{\mathrm{ref}}^T \underline{\hat{\hat{\mathbf{j}}}}_{\mathrm{ref}}}}, \quad x_{\mathrm{p}} = \frac{max(\underline{\hat{\hat{\mathbf{j}}}}_{\mathrm{err}})}{max(\underline{\hat{\hat{\mathbf{j}}}}_{\mathrm{ref}})}, \quad x_{\mathrm{div}} = \sqrt{\underline{\hat{\hat{\mathbf{j}}}}^T \underline{\hat{\hat{\mathbf{j}}}}}$$

The solution of the curl-curl system is calculated by an ILU preconditioned COCG solver. For the solution of the divergence corrections in the second step of the Ex-SPFD approach, a Jacobi preconditioned BiCGStab solver was used. All calculations were run on a Pentium IV 3 GHz machine with 2 GB RAM. The calculation times refer to the wall-clock time.

Table 4.1: Errors and divergences of the curl-curl solution for model 1 and model 2 at 50 Hz

	model 1				model 2			
acc.	time / s	x / %	x_{p} / %	x_{div}	time / s	x / %	x_{p} / %	x_{div}
1E-15	18:13:47	-	-	1.4E-14	21:09:25	-	-	1.7E-14
1E-14	10:28:29	1.1E-4	5.0E-4	1.0E-13	16:46:48	4.9E-5	5.1E-4	9.6E-14
1E-13	07:48:29	1.5E-3	9.9E-3	8.4E-13	07:55:27	1.1E-3	4.2E-3	1.3E-12
1E-12	05:11:53	2.5E-2	0.12	8.7E-12	05:46:00	1.3E-2	6.1E-2	1.2E-11
1E-11	02:39:20	0.51	1.09	1.1E-10	03:27:06	0.22	0.43	1.3E-10
1E-10	00:36:55	4.00	6.13	1.6E-09	01:16:13	1.81	4.04	1.8E-09
1E-09	00:10:02	26.43	18.93	1.2E-08	00:25:31	14.18	20.47	1.7E-08
1E-08	00:02:33	99.50	42.03	3.7E-08	00:08:20	151.7	49.96	7.2E-08
1E-07	00:01:52	99.50	42.03	3.7E-08	00:03:12	261.5	70.29	1.4E-07
1E-06	00:01:29	99.50	42.03	3.7E-08	00:02:23	261.5	70.29	1.4E-07

The first validation scenario consists of the first and second model at a frequency of 50 Hz. The first model was discretized with 331,240 grid cells, the second model with 394,680. Tab. 4.1 summarizes the estimated errors and divergence values for the calculated induced currents, using only the curl-curl equation with different solver accuracies. The computational time to obtain the reference solution amounts to 18:13:47 for model 1 and 21:09:25 for model 2. The time does not increase linearly with the solver accuracy, the increase is larger at higher accuracies. The currents calculated with an accuracy of 10^{-7} or less exhibit very large errors. At this solver accuracies, the $i\omega\mathbf{M}_\kappa$ term has no effect on the solution, because it is numerically too small. This behavior can also be observed in the calculated divergences. Currents calculated from the electric field obtained at this solver accuracies are non-physical. From a relative residuum of 10^{-9} in model 1 and 10^{-8} in model 2 the divergence and the errors are reduced by roughly one order of magnitude for each accuracy step. The accuracy of 10^{-9} corresponds to the magnitude of the numerical contrast of the $\widetilde{\mathbf{C}}\mathbf{M}_\nu\mathbf{C}$ and $i\omega\mathbf{M}_\kappa$ operator, as explained in the previous section. This table confirms the need for a very low relative residuum in order to calculate the induced currents reliably. Such high accuracies lead to very large computational times.

Tab. 4.2 presents the errors and divergence values calculated using the Ex-SPFD approach for model 1 and model 2, at 50 Hz. The given computational time is the sum of the time needed for the curl-curl solution in the first step and the divergence correction in the second step. In these calculations, the field quantities are complex-valued. However, since the system matrix in the second Ex-SPFD step is real-valued, the complex and the

Table 4.2: Errors and divergences of the Ex-SPFD solution for model 1 and model 2 at 50 Hz

	model 1				model 2			
acc.	time / s	x / %	x_p / %	x_div	time / s	x / %	x_p / %	x_div
				curl-curl solution with 1E-3 acc.				
1E-12	00:03:51	2.04	2.29	3.4E-15	00:03:49	1.40	1.56	1.0E-14
1E-09	00:03:18	2.04	2.29	4.9E-15	00:03:34	1.40	1.56	1.0E-14
1E-06	00:02:59	2.04	2.29	4.9E-12	00:02:54	1.40	1.56	3.5E-12
1E-03	00:01:39	2.46	1.89	1.3E-10	00:01:27	2.02	2.32	3.8E-10
				curl-curl solution with 1E-6 acc.				
1E-12	00:04:43	6.9E-3	8.9E-3	3.9E-15	00:04:56	3.7E-3	2.6E-3	1.0E-14
1E-09	00:04:35	6.9E-3	8.9E-3	3.4E-15	00:04:44	3.7E-3	2.6E-3	1.1E-14
1E-06	00:04:14	9.3E-3	1.4E-2	3.8E-12	00:04:10	6.9E-3	7.0E-3	4.5E-12
1E-03	00:02:44	1.20	0.84	1.2E-10	00:02:41	1.33	2.46	4.1E-10
				curl-curl solution with 1E-9 acc.				
1E-12	00:12:36	1.8E-5	2.4E-5	2.6E-15	00:12:44	1.5E-5	3.1E-5	1.0E-14
1E-09	00:12:14	1.8E-5	2.4E-5	2.8E-15	00:12:23	1.5E-5	3.1E-5	7.1E-15
1E-06	00:11:56	3.4E-3	4.8E-3	2.0E-12	00:11:58	6.2E-3	8.9E-3	7.0E-12
1E-03	00:10:20	1.15	0.65	9.5E-11	00:10:22	0.84	1.31	1.8E-10

real part of the solution can be calculated successively. The accuracy in the first column of the table refers to the relative residuum used for the solution of the divergence correction. Three different solver accuracies were used for the solution of the curl-curl equation in the first step. As expected from the scheme, the divergence of the currents is reduced very effectively in all cases. However, using an accuracy of only 10^{-3} for the solution of the first step, the calculated currents exhibit an error of ≈ 2 %. Using such a low solver accuracy for the curl-curl solution, results in a magnetic vector potential that does not yet describe the magnetic field exact enough. Increasing the solver accuracy in the first step to 10^{-6} and using an accuracy of 10^{-6} or better for the divergence correction, the errors drop by five orders of magnitude to $\approx 10^{-3}$ %. For these accuracies, the calculation time remains below five minutes. A comparable error of the currents computed using only the curl-curl equation was obtained with a solver accuracy of 10^{-13} (Tab. 4.1). For the pure curl-curl solution, nearly eight hours were needed. Thus, the Ex-SPFD approach offers an improvement of the computational time by a factor of ≈ 100. Increasing the solver accuracy in both Ex-SPFD steps to 10^{-9} further reduces the error down to $\approx 10^{-5}$ %. This error is an order of magnitude better than the pure curl-curl solution at 10^{-14}, at a computational time of 12 minutes compared to 10.5 hours for the pure curl-curl solution. This validation scenario clearly confirms the substantial reduction of the computational time by the Ex-SPFD approach, when compared to a pure curl-curl solution at 50 Hz.
Because of the low conductivity of the human body, the shielding effect of the induced currents on the magnetic field is expected to be negligible. An analysis of the impact of the shielding effect can be performed, by neglecting the conductivity term in the first step of the Ex-SPFD approach and compare the so obtained results to the full reference solution. In this case, the curl-curl system becomes real-valued. The so-calculated vector potential corresponds to the free space solution. The neglect of the conductivity in the curl-curl equation drastically reduces the computational times at high solver accuracies, as depicted by Tab. 4.3 for model 1. At a solver accuracy of 10^{-3} and 10^{-6} no difference in the computational time among the solution incorporating the conductivity and the solution of the system neglecting the conductivity can be observed. This is another effect of the conductivity contrast of the both terms in the curl-curl equation.

Table 4.3: Calculation times for the free space solution of model 1

acc.	time / s
1E-15	00:03:54
1E-12	00:02:36
1E-09	00:01:58
1E-06	00:01:10
1E-03	00:00:36

Table 4.4: Errors and divergences of the Ex-SPFD solution for model 1 at 50 Hz, neglecting the conductivity in the first step.

acc.	time / s	x / %	x_p / %	x_div
	curl-curl solution with 1E-6 acc.			
1E-12	00:02:33	1.4E-3	1.3E-3	3.6E-15
1E-09	00:02:19	1.4E-3	1.3E-3	3.2E-15
1E-06	00:02:10	7.5E-3	1.5E-2	4.3E-12
1E-03	00:01:21	1.23	0.90	1.1E-10
	curl-curl solution with 1E-9 acc.			
1E-12	00:03:13	2.9E-5	2.4E-5	3.2E-15
1E-09	00:03:09	3.4E-5	2.4E-3	9.8E-15
1E-06	00:02:59	1.6E-2	3.5E-2	1.0E-11
1E-03	00:01:19	1.20	0.87	1.1E-10

The errors and divergences calculated using the Ex-SPFD approach, with omitted conductivity in the first step are summarized in Tab. 4.4. Using a solver accuracy of 10^{-6} in the first step, the estimated errors are even slightly lower than in the case when the conductivity term was present in the first step (Tab. 4.2). For a solver accuracy of 10^{-9} in the first step, the errors become slightly larger. From this results it can be concluded, that at 50 Hz the shielding effect is negligible and a free space solution of the magnetic field can be used, like it is the case in the classical SPFD approach. Omitting the conductivity in the first step also leads to a further decrease of the computational times, since all systems become real-valued.

The second validation scenario consists of model 1 at 100 kHz and model 2 at 10 kHz. The same grids as in the previously presented 50 Hz calculations were used. Tab. 4.5 summarizes the estimated error and divergence values for the calculated induced currents using only the curl-curl equation. The time needed to obtain the reference solution with an accuracy of 10^{-15} decreases with increasing frequency, as: 18:13:47 at 50 Hz, 08:42:50 at 10 kHz and 06:38:40 at 100 kHz. This is due to the effect of the eigenvalue distribution on a Krylov-type solver. For a large separation of the eigenvalues, the solvers performance decreases. Because the magnitude of the eigenvalues is directly connected to the magnitude of the operators, this can be understood as a further effect of the contrast between the

Table 4.5: Errors and divergences of the curl-curl solution for model 1 at 100 kHz and model 2 at 10 kHz

	model 1 at 100 kHz				model 2 at 10 kHz			
acc.	time / s	x / %	x_p / %	x_{div}	time / s	x / %	x_p / %	x_{div}
1E-15	06:38:41	-	-	8.4E-12	08:42:50	-	-	1.5E-09
1E-14	06:07:21	4.7E-7	3.3E-6	8.4E-12	08:00:49	9.2E-7	5.1E-6	1.5E-09
1E-12	05:01:06	8.5E-6	1.4E-7	2.7E-11	06:38:59	3.8E-5	3.6E-4	1.2E-11
1E-10	03:13:07	7.9E-4	2.8E-3	2.4E-09	03:05:11	7.1E-3	4.3E-2	1.3E-06
1E-09	02:44:00	7.9E-3	3.4E-2	2.4E-08	02:01:17	8.1E-2	0.19	1.7E-05
1E-08	01:19:15	0.16	0.47	1.7E-07	00:52:33	0.89	3.08	1.9E-04
1E-06	00:08:31	12.5	20.1	1.6E-05	00:07:49	53.2	30.5	1.6E-02
1E-04	00:00:46	93.0	53.0	9.8E-05	00:01:29	275	82.2	3.8E-02

curl-curl and the conductivity term. At higher frequencies, the contrast is lower, thus the divergence of the calculated currents is already reduced starting from a solver accuracy of 10^{-6} at 10 kHz, compared to 10^{-9} in the 50 Hz case. However, the computational time for the solutions at low accuracies also increases, e.g for a relative residuum of 10^{-9} at 50 Hz only 10 minutes are needed, for the same accuracy at 100 kHz the time amounts to 02:44:00.

Table 4.6: Errors and divergences of the Ex-SPFD solution for model 1 at 100 kHz and model 2 at 10 kHz

	model 1 at 100 kHz				model 2 at 10 kHz			
acc.	time / s	x / %	x_p / %	x_{div}	time / s	x / %	x_p / %	x_{div}
curl-curl solution with 1E-6 acc.								
1E-12	00:11:02	4.5E-3	1.6E-3	8.7E-12	00:10:46	1.6E-3	7.5E-4	3.1E-12
1E-09	00:10:47	4.5E-3	1.6E-3	1.1E-11	00:10:23	1.6E-3	7.5E-4	3.0E-12
1E-06	00:10:09	1.E-2	3.4E-2	2.1E-08	00:09:44	1.9E-2	3.2E-2	5.5E-09
1E-03	00:08:50	1.61	1.53	2.2E-07	00:08:06	0.93	3.08	6.8E-08
curl-curl solution with 1E-9 acc.								
1E-12	02:46:37	6.8E-6	1.3E-5	7.3E-12	02:04:04	6.8E-6	1.6E-5	1.3E-12
1E-09	02:46:13	6.8E-6	1.3E-5	7.3E-15	02:03:52	6.8E-6	1.6E-5	1.3E-12
1E-06	02:44:51	7.6E-6	1.3E-5	9.0E-12	02:02:22	6.2E-5	6.6E-5	1.2E-11
1E-03	02:44:07	2.9E-4	8.2E-4	8.5E-11	02:01:32	8.1E-3	1.2E-2	4.4E-10
curl-curl solution with 1E-6 acc. and neglecting the conductivity								
1E-12	00:02:37	7.0E-2	1.4E-3	9.2E-12	00:03:53	5.2E-3	1.3E-3	2.8E-12
1E-09	00:02:30	7.0E-2	1.4E-3	9.2E-12	00:03:28	5.2E-3	1.3E-3	2.9E-12
1E-06	00:02:17	7.0E-2	1.4E-3	1.2E-11	00:03:18	7.5E-3	5.9E-3	9.9E-10
1E-03	00:01:30	0.15	0.15	6.7E-08	00:02:22	0.77	3.05	8.8E-08
curl-curl solution with 1E-9 acc. and neglecting the conductivity								
1E-12	00:03:37	7.0E-2	5.8E-6	9.5E-12	00:05:35	4.8E-3	1.6E-5	2.6E-12
1E-09	00:03:23	7.0E-2	5.8E-6	9.6E-15	00:05:19	4.8E-3	1.6E-5	2.8E-12
1E-06	00:03:02	7.0E-2	2.8E-5	1.3E-11	00:05:07	5.7E-3	3.6E-3	6.1E-10
1E-03	00:02:17	0.15	0.15	6.7E-08	00:04:08	0.81	3.20	8.8E-08

The increase of the time needed for the curl-curl solution heavily affects the overall time of the Ex-SPFD approach, as can be concluded from Tab. 4.6, in which the errors and divergences of the Ex-SPFD results for model 1 at 100 kHz and model 2 at 10 kHz are collected. When the conductivity is included in the first Ex-SPFD step, the global and point-wise errors exhibit similar values as in the first scenario. For an error of $\approx 10^{-3}$ %, which is calculated by a pure curl-curl solution at a solver accuracy of 10^{-10}, we obtain a reduction of the computational time by a factor of 35. When a lower error is desired, the curl-curl equation has to be solved with an accuracy of 10^{-9} in the first step of the Ex-SPFD approach, resulting in a reduction of the computational time by only a factor of three. Neglecting the shielding effect of the induced currents, by omitting the conductivity in the first Ex-SPFD step, mainly affects the global error, but significally reduces the

computational time. The effect of the shielding can be directly observed in the global errors of the Ex-SPFD results obtained with an curl-curl accuracy of 10^{-9} (without conductivity) and a divergence correction of 10^{-9}. At 50 Hz the error amounts to $1.8{\cdot}10^{-5}$ %, at 10 kHz to $4.8 \cdot 10^{-3}$ % and at 100 kHz to $7.0 \cdot 10^{-2}$ %. However, the point-wise errors remain better than $3 \cdot 10^{-5}$ % at all times, allowing to conclude that the shielding effect can also be neglected at frequencies up to 100 kHz. Using a free-space magnetic field further increases the performance of the Ex-SPFD approach, as can be observed in the computational times presented in the lower half of Tab. 4.6.
The third and last validation scenario deals with models in which, besides the human body also other materials that affect the magnetic field are present in the computational domain. This is a highly conductive block inserted into the right shoulder of model 1 and model 3 containing a coil with a permeable cylinder. The conductivity of the block was set to 10^{-6} S/m, a typical value for metals. The model was meshed with 319,488 cells. For the permeable cylinder a relative permeability of 1000 was chosen. Model 3 was meshed with 334,800 cells. All calculations were performed at 50 Hz.

Table 4.7: Errors and divergences of the curl-curl solution for model 1 with inserted highly conductive block at 50 Hz and model 3 at 50 Hz

	model 1 with conductive block at 50 Hz				model 3 at 50 Hz			
acc.	time / s	x / %	x_p / %	x_div	time / s	x / %	x_p / %	x_div
1E-15	42:18:43	-	-	-	57:34:49	-	-	2.1E-14
1E-14	28:08:50	5.6E-5	8.1E-6	-	29:35:19	2.3E-5	1.7E-4	8.9E-14
1E-12	11:11:26	1.6E-2	4.0E-2	-	11:47:48	6.6E-3	1.2E-2	1.4E-11
1E-10	01:54:43	2.46	4.7	-	02:09:49	1.31	1.96	1.3E-06
1E-09	00:28:23	19.5	19.13	-	00:42:14	11.0	10.6	2.4E-8
1E-08	00:06:05	98.1	41.5	-	00:04:52	95.9	34.2	1.5E-07
1E-06	00:08:31	98.2	41.5	-	00:03:01	95.9	34.2	1.5E-07

Tab. 4.7 summarizes the results obtained for the third scenario using a pure curl-curl solution. Due to the large conductivity of the inserted block, very high currents are induced inside the block. These high values obscure the details of the solution inside the body, therefore the errors were estimated only for the currents in biological tissue. Setting the induced currents inside the conductive block to zero, affects the calculation of the divergences by locally modifying the balance equations. Therefore, the divergences are not presented for this case. Compared to the model containing no conductive block at 50 Hz, the computational time for the reference solution is doubled and amounts to 42:18:43. With the conductive block present, the entires of the $i\omega\mathbf{M}_\kappa$ operator span by approximately eight orders of magnitude. This leads to a drastic increase of the condition number of the system, that negatively affects the computational time in addition to the large contrast of the operators at 50 Hz. The permeable cylinder in model 3 further increases this contrast, leading to a time of 57:34:49 for the reference solution.
The errors and divergences of the Ex-SPFD approach for the third scenario are summarized in Tab. 4.8. Using the full curl-curl solution at a solver accuracy of 10^{-6} or 10^{-9} results in similar errors as in the previously presented scenarios. For an error of $\approx 10^{-3}$ % a curl-curl solution with a solver accuracy of 10^{-6} and a divergence correction with an accuracy of 10^{-9} is sufficient. For this accuracies, the computational time is decreased by a factor of 130 for the model with the conductive block and a factor of 180 for model 3. In the case of the conductive block and for higher accuracies in the divergence correction, the Jacobi preconditioned BiCGStab solver diverges in certain cases (indicated by a dagger in Tab. 4.8). For these cases, an algebraic multigrid preconditioner was used. As expected,

neglecting the conductivity in the first step of the Ex-SPFD approach in model 3 has nearly no effect on the error. Although the induced currents are larger due to the larger magnetic flux density, the ratio of the magnetic fields produced by the induced currents and the external field remains the same as in the case when only the body is present in the computational domain. Therefore, the shielding effect can be neglected for model 3. This is not the case for the model containing the highly conductive block. Neglecting the conductivity in the first step leads to an increase of the point-wise errors by at least three orders of magnitude up to 0.1 %. An alternative way to exactly model the shielding effect of the conductive block, is to include only the conductivity of the block and neglect the conductivity of the body in the first Ex-SPFD step. The so calculated currents exhibit a very similar error compared to the case when all conductive pieces were included in the first step, however at a lower computational time. In the case when only the block is present in the curl-curl equation, the contrast of both operators is greatly reduced. Furthermore, the increase of the condition number is not as distinct, since only one conductivity value is used.

Table 4.8: Errors and divergences of the Ex-SPFD solution for model 1 with a highly conductive block inserted at 50 Hz and model 3 at 50 Hz

	model 1 with conductive block				model 3 with permeable cylinder			
acc.	time / s	x / %	x_p / %	x_div	time / s	x / %	x_p / %	x_div
				curl-curl solution with 1E-6 acc.				
1E-12	00:08:25	2.4E-3	2.2E-3	-	00:05:37	4.2E-4	2.4E-4	1.3E-14
1E-09	00:06:57	4.0E-3	8.5E-3	-	00:05:31	4.2E-4	2.4E-4	4.1E-14
1E-06	00:05:10	0.15	0.51	-	00:04:59	3.7E-3	3.2E-2	5.5E-09
1E-03	00:04:07	7.21	39.7	-	00:03:22	1.55	0.72	3.6E-10
				curl-curl solution with 1E-9 acc.				
1E-12	00:28:59†	1.6E-5	2.0E-5	-	00:46:06	1.1E-5	8.9E-6	1.0E-14
1E-09	00:33:32	1.5E-2	3.1E-2	-	00:45:32	1.1E-5	8.9E-6	1.3E-14
1E-06	00:29:38	3.6E-2	0.11	-	00:45:03	7.4E-3	7.5E-3	1.7E-11
1E-03	00:28:48	2.73	14.3	-	00:42:48	1.41	0.76	2.6E-10
				curl-curl solution with 1E-6 acc. and neglecting the conductivity				
1E-12	00:01:46†	4.9E-2	0.13	-	00:05:36	1.9E-4	7.5E-5	1.3E-14
1E-09	00:01:45†	4.9E-2	0.13	-	00:05:08	1.9E-4	7.5E-5	2.1E-14
1E-06	00:02:13	0.15	0.34	-	00:04:07	6.4E-3	6.7E-3	1.4E-11
1E-03	00:01:44	7.21	39.5	-	00:04:18	1.36	0.68	3.2E-10
				curl-curl solution with 1E-9 acc. and neglecting the conductivity				
1E-12	00:02:41†	7.3E-2	0.19	-	00:09:40	2.5E-5	9.8E-6	1.3E-14
1E-09	00:07:58	7.0E-2	0.18	-	00:09:31	2.5E-5	9.8E-6	1.3E-14
1E-06	00:03:07	0.15	0.33	-	00:09:17	7.1E-3	5.8E-3	1.6E-11
1E-03	00:02:36	7.21	39.5	-	00:08:36	1.41	0.71	3.2E-10
				curl-curl solution with 1E-6 acc. and only block conductivity				
1E-12	00:04:34†	1.8E-3	1.6E-3	-	-	-	-	-
1E-09	00:10:65	6.1E-3	1.8E-2	-	-	-	-	-
1E-06	00:05:21	0.15	0.34	-	-	-	-	-
1E-03	00:04:18	6.86	37.9	-	-	-	-	-
				curl-curl solution with 1E-9 acc. and only block conductivity				
1E-12	00:08:28†	2.9E-5	2.0E-5	-	-	-	-	-
1E-09	00:14:57	9.2E-3	2.3E-4	-	-	-	-	-
1E-06	00:09:20	0.15	0.34	-	-	-	-	-
1E-03	00:08:18	6.93	38.2	-	-	-	-	-

The presented validation scenarios clearly confirm the superior performance of the Ex-SPFD approach. Due to the large numerical contrast of the $\widetilde{\mathbf{C}}\mathbf{M}_\nu\mathbf{C}$ and $i\omega\mathbf{M}_\kappa$ operator, a very high solver accuracy has to be used, when only the curl-curl equation is employed. Along with the fact that three degrees of freedom for each grid cell are needed in the curl-curl equation, this leads to large computational times. Applying a two-step procedure, like in the Ex-SPFD approach greatly decreases the computational time, since both operators

can act separately, leading to a much faster convergence. From the analysis of the impact of the shielding effect of the induced currents, it was concluded that the shielding can be neglected, when only biological tissue is present in the computational domain. This allows a simplification of the Ex-SPFD scheme by neglecting the conductivity in the first step and leads to a further performance gain. Tab. 4.9 summarizes the computational times and needed solver accuracies of all presented models for a global and point-wise error of better than $5 \cdot 10^{-3}$ %. In the curl-curl column the accuracy and the time of the pure curl-curl solution is presented. An asterix at the accuracy of the first Ex-SPFD step is used, when the conductivity was omittted in the first step. In the model containing the conductive block only the block conductivity was used in the first step, denoted with a plus sign. For the same model, an AMG preconditioner was used for the divergence correction. This only slightly modifies the complete calculation time of the Ex-SPFD approach, since the first step is the more time consuming one. In the "acceleraton factor" column, the speedup factor of the computational time is given. It is evident, that the Ex-SPFD approach works best for a high contrast of both operators.

Table 4.9: Summary of the validation scenarios.

	curl-curl		Ex-SPFD			acceleration
model	acc	time / s	acc. 1^{st}	acc. 2^{nd}	time / s	factor
50 Hz	1E-14	37709	1E-6*	1E-9	139	202
10 kHz	1E-11	15071	1E-9*	1E-9	319	47
100 kHz	1E-10	11587	1E-6	1E-9	647	17
permeable	1E-13	62049	1E-6*	1E-9	308	201
conductive	1E-13	57336	1E-9$^+$	1E-12	508$^+$	112

When the conductivity is omitted in the first step of the Ex-SPFD approach, the calculated vector potential corresponds to a free-space solution that equals to the static magnetic field. For the calculation of static magnetic fields also a scalar potential approach can be used, however scalar magnetic potentials can not be used in a straightforward way for the divergence correction. Since in the first Ex-SPFD step a system of the size three times the number of grid cells has to be solved and in the second step the system size is equal to the number of grid cells, the first step limits the applicable spatial resolution due to the larger memory requirement. Furthermore, the solution of the curl-curl equation is more time consuming than the solution of a Poisson system. Therefore, an alternative way to calculate the magnetic vector potential, using a vector Poisson system will be presented in the following subsection.

4.1.4 Vector Poisson System

In order to further increase the available spatial resolution and decrease the computational time, an alternative way to calculate the vector potential is presented in the following. It is based on a vector Poisson system, that allows to calculate the three components of the vector potential successively. The alternative way is valid in the case when the

permeability in the computational domain is constant. Then, using the general vector analytical property

$$\nabla \times \nabla \times \vec{A} = \nabla(\nabla \cdot \vec{A}) - \Delta \vec{A} \tag{4.17}$$

along with the Coulomb gauge condition $\nabla \cdot \vec{A} = 0$ leads to a decoupling of the three components of the magnetic vector potential. In principle, this approach can also be employed when shielding effects of highly conductive material have to modeled. Then, the vector potential is complex-valued and the conductivity term is added to the vector Poisson system (4.18). However, this case was not implemented since in most calculations using only the human body and the source of the magnetic field yields accurate results. For the calculation of the free-space magnetic vector potential we obtain

$$\Delta A_n = -\mu_0 J_n \tag{4.18}$$

where n denotes the three spatial components $\{x, y, z\}$. Following the solution of the three systems, the components can be collected into one vector, resulting in a vector potential as obtained from the curl-curl equation. However, some modifications have to be applied: In the vector Poisson approach, the components of the vector potential and the excitation current become node based. This is contrary to the standard FIT, where $\vec{A}$ is allocated at the primal grid edges and $\vec{J}$ at the dual facets. When applying incidence operators to the vector potential obtained from the vector Poisson approach, like e.g. for the calculation of the magnetic field from $\widehat{\widehat{\mathbf{b}}} = \mathbf{C}\widehat{\mathbf{a}}$, the incidence operators have to be scaled with the edge lengths. To avoid the need for such modifications, an elegant workaround is the use of an equidistant grid, for which all edge lengths are equal. Also the boundary conditions need special treatment. In order to apply a global boundary condition to the vector potential, adequate boundary conditions have to be set for each system of the vector Poisson approach. In the actual implementation, an electric boundary condition is obtained by setting homogeneous Neumann and Dirichlet boundaries for each Poisson system in the following way:

- x component: Neumann condition at the x boundaries, Dirichlet condition at the y and z boundaries;
- y component: Neumann condition at the y boundaries, Dirichlet condition at the x and z boundaries;
- z component: Neumann condition at the z boundaries, Dirichlet condition at the x and y boundaries;

Tab. 4.10 summarizes the computational times for the free-space magnetic vector potential of the electric blanket presented in Sec. 4.2.1, calculated using the curl-curl equation and the vector Poisson system at various resolutions. A relative residuum of 10^{-6} was chosen for the solution, obtained using a Jacobi preconditioned BiCGStab solver in both cases. All calculations were run on Intel Xeon 3,2 GHz processors with 8 GB RAM connected by Infiniband. Using the vector Poisson approach on a single processor accelerates the solution by a factor of ≈ 1.7. For the large systems in the lower part of Tab. 4.10, 22 processors were used in parallel. At the finest presented resolution, corresponding to 111 million grid cells, no curl-curl solution could be obtained due to memory restrictions. For a high grid cell count, the acceleration factor increases, up to 2.7 at 88 million grid cells. The reason

Table 4.10: Computational times of the curl-curl equation and the vector Poisson approach at various resolutions.

# grid cells (mil.)	# processors	curl-curl time / s	vector Poisson time / s	acceleration factor
1.03	1	188	114	1.6
2.05	1	510	293	1.7
3.02	1	779	462	1.7
4.05	1	1164	746	1.6
5.09	1	1474	883	1.7
21.62	22	850	373	2.3
45.24	22	2060	892	2.3
66.19	22	3490	1384	2.5
88.19	22	5674	2064	2.7
111.13	22	-	2741	-

for this increase can be attributed to the degrees of freedom of the compared systems. Because three dofs are used in the curl-curl formulation, the number of the matrix elements is $39N_p$, while for the vector Poisson approach it amounts to $7N_p$. Thus, the vector Poisson system is very well suitable for the calculation of the free-space magnetic vector potential at fine resolutions. Additionally to the disadvantageous increase of the system matrix size in the curl-curl formulation, also strict restrictions for the possible preconditioners and solvers apply to curl-curl systems. Due to the singular character of the curl-curl equation, only a limited combination of solvers and preconditioners from the used PETSc package can be employed. This further disadvantage will be elaborated in App. A, along with an analysis of the computational times for various preconditioner-solver combinations.

4.2 Applications

In the following, the presented Ex-SPFD approach will be applied to selected problems. A dosimetric study of the currents induced inside the body by an electric blanket will demonstrate the need for an exact modeling of the field sources. This is followed by a calculation of induced currents in the brain during a TMS treatment. For this case, a way to obtain the transient behavior of the induced currents using the Fourier transform in a post-processing step will be presented. Finally, simulations of a mapping study of the motor cortex will show, that a connection between the calculated induced current densities and neural activity can be established.

4.2.1 Dosimetric Analysis of an Electric Blanket

In the first application example, induced currents inside the body originating from an electric blanket are calculated. Electric blankets are quite widely spread throughout households and typically cover nearly the entire body when used, leading to a large exposition area. Simulation results of electric blankets computed by the impedance method can be found

in [47]. Two different wiring configurations are considered: In the first configuration, the ends of the heating windings are closed by a straight wire, while in the second configuration the back and forth wires are arranged close to each other. The wiring of the blanket is arranged at a constant distance to the body, therefore, the blanket geometry is not planar, resulting in a fully three dimensional field source, see Fig. 4.3.

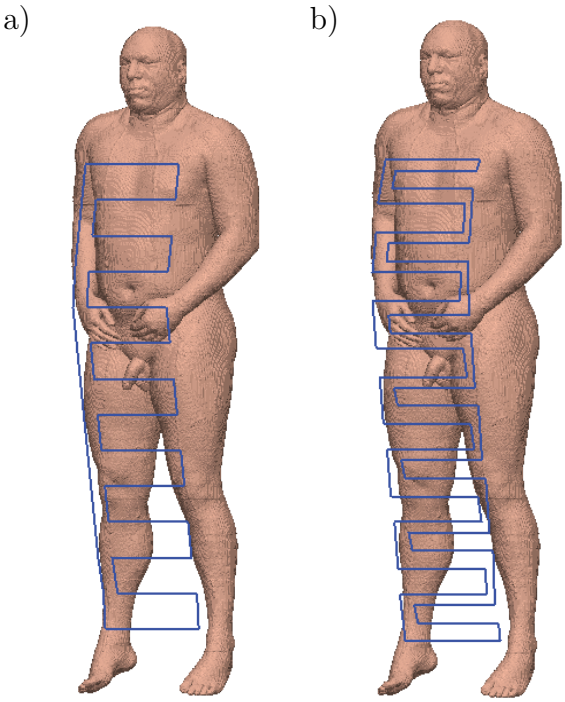

Figure 4.3: The two different wiring scenarios considered. a) One straight wire connecting the endpoints. b) All wires aligned parallel to each other.

The current inside these wires is set to 0.65 A, corresponding to 150 W heating power. The calculation domain is discretized homogeneously with 208 million grid cells, corresponding to a resolution of 1.5 mm. This is by far the finest ever achieved resolution in calculations of this type. The magnetic vector potential is calculated using the vector Poisson approach presented in Sec. 4.1.4. All simulations were run on 24 compute nodes equipped with a 3.2 GHz Intel Xeon processor and 8 GB RAM connected by gigabit ethernet. Using a Jacobi preconditioned Conjugate Gradient method for the solution of the linear equation systems, all three components of the magnetic vector potential are calculated in 120 minutes with a relative residuum of 10^{-6}. The solution of the SPFD Equation is obtained using Successive Over Relaxation (SOR) preconditioned Bi-Conjugate Gradient Stabilized method (BiCGStab). For a relative residuum of 10^{-6} a calculation time of 84 minutes is needed.

The organ-wise evaluated results of the simulations are summarized in Tab. 4.11. The largest induced current densities are found in blood and muscle tissue: $5.7 \cdot 10^{-5}$ A/m^2 in blood for wiring case a) and $3.3 \cdot 10^{-5}$ A/m^2 in muscle tissue for wiring case b). Both values are situated well below the *ICNIRP* restriction for the general public ($2.0 \cdot 10^{-3}$ A/m^2). With the used parameters, the maximal magnetic field strength in close proximity to the wires amounts to 73.7 μT in case a) and 78.1 μT in case b). Although the maximal

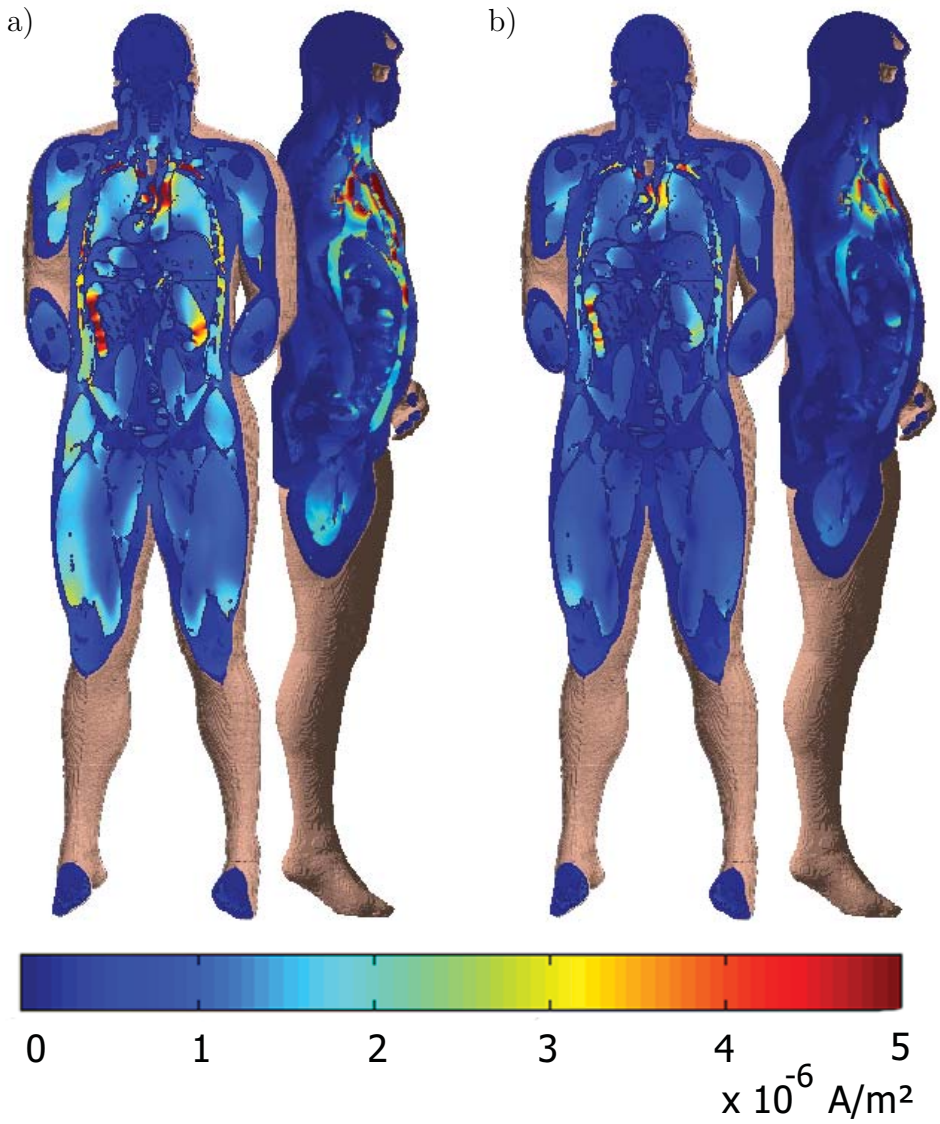

Figure 4.4: Plot of the induced current densities in the coronal and midsgittal planes.

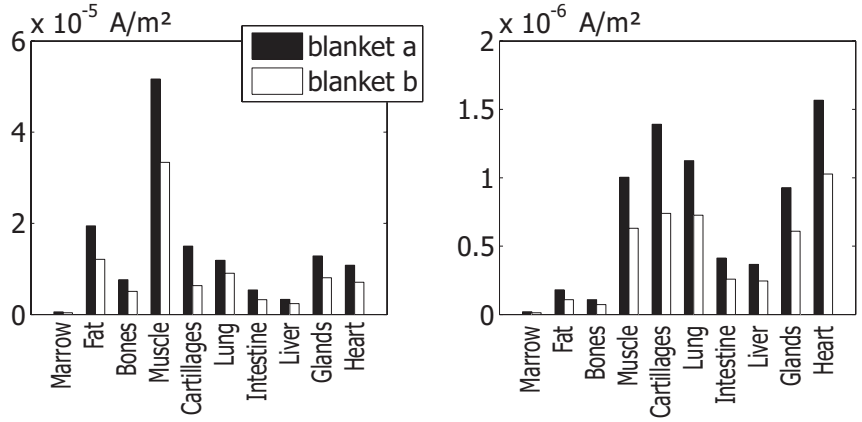

Figure 4.5: Tissue-wise maximum (left) and mean (right) induced current densities for selected tissue types.

Table 4.11: Organ-wise induced current densities originating from an electric blanket. The used wiring configurations are depicted in Fig. 4.3.

	induced current density / A/m^2				
	case a)		case b)		
Tissue Type	mean	max	mean	max	# voxel
Whole Body	**5.60e-7**	**5.70e-5**	**3.67e-7**	**3.34e-5**	**31,108,782**
Skeleton Muscle	1.00e-6	5.16e-5	6.31e-7	3.34e-5	12,822,593
Fat Tissue	1.80e-7	1.94e-5	1.08e-7	1.20e-5	11,593,463
Bones	1.09e-7	7.63e-6	7.21e-8	5.06e-6	1,248,882
Lung	1.13e-6	1.19e-5	7.26e-7	9.06e-6	1,092,476
Marrow	2.01e-8	5.85e-7	1.26e-8	3.79e-7	908,116
Skin	2.82e-14	4.54e-12	1.91e-14	2.69e-12	581,189
Intestine Contents	2.03e-6	2.09e-5	1.23e-6	1.25e-5	574,895
Liver	3.67e-7	3.31e-6	2.45e-7	2.38e-6	559,470
Intestine	4.12e-7	5.38e-6	2.58e-7	3.26e-6	389,820
Blood	1.81e-6	5.70e-5	1.16e-6	3.30e-5	224,750
Heart	3.91e-6	3.81e-5	2.57e-6	2.46e-5	197,838
Grey Substance	6.19e-8	4.54e-7	4.80e-8	3.58e-7	187,688
White Substance	4.60e-8	1.47e-7	3.57e-8	1.17e-7	159,931
Cartilages	1.39e-6	1.50e-5	7.39e-7	6.32e-6	117,893
Kidney	4.71e-7	2.74e-6	3.01e-7	1.69e-6	105,679
Spleen	5.69e-7	2.35e-6	3.58e-7	1.54e-6	70,477
Neuronal Fabric	3.46e-8	1.98e-7	2.45e-8	1.55e-7	50,364
Stomach	1.29e-6	1.23e-5	9.42e-7	9.01e-6	47,990
Nervus Opticus	3.81e-8	4.80e-7	2.65e-8	2.67e-7	46,673
Glands	9.27e-7	1.28e-5	6.09e-7	8.06e-6	38,635
Pancreas	8.12e-7	7.58e-6	5.92e-7	4.86e-6	27,344
Mucous Membrane	5.63e-11	6.72e-10	4.98e-11	5.03e-10	26,524
Bladder	3.87e-7	2.21e-6	1.69e-7	7.54e-7	25,282
Gall Bladder	2.01e-6	1.21e-5	1.56e-6	1.48e-5	6,595

magnetic field is very similar in both cases, the induced current densities are approximately 30 % larger in wiring case a). This effect is mainly due to the reduced area enclosed by the current paths in case b) and demonstrates the necessity of a geometrically realistic modeling of the field sources. The only value larger in case b) than in case a) is the maximal current density in gall bladder. However, the gall bladder is a very small organ, situated in the main exposition area of both blankets, so this deviation can occur due to a local field maximum. For a better overview, a graphical representation of the calculated values for selected tissue types can be found in Fig. 4.5. These results also suggest, that the use of derived reference levels as proposed by the *ICNIRP* guidelines (see section 1.3.2) can sometimes lead to an inaccurate estimation of the basic dosimetric quantity. In such cases, a more detailed analysis is needed. Plots of the induced current densities in the coronal and midsagittal planes for both wiring configurations are depicted in Fig. 4.4. The used color ramp can be found beneath the plots. Blue represents areas of lowest current densities, while red domains stand for the maximal current densities of $5 \cdot 10^{-6}$ A/m^2.

4.2.2 Introduction to Transcranial Magnetic Stimulation (TMS)

As already pointed out in Sec. 1.3.2, currents of high magnitudes inside the body can lead to a stimulation of muscle and nerve tissue. Targeted stimulation of certain areas is used in many medical applications, most prominent in cardiac pacemakers. Other applications include pain treatment [81, 82], wound healing [83], Alzheimer's disease [84], Parkinson's disease [85, 86] and stroke recovery [87, 88], just to name a few. For the case of electrical stimulation, the current is injected into the body through surface, needle or implanted electrodes. It has been in widespread clinical use for many years. However, this technique suffers from serious drawbacks. Surface electrodes can not be used for the stimulation of deeper structures and the implantation of electrodes comes along with the need of surgical treatment. The first non-invasive magnetic stimulation of human and animal peripheral nerves were reported by Bickford and Freeming in 1965 [89]. Throughout the 1970's Barker analyzed the interaction of short, pulsed magnetic fields for use in nerve stimulation, leading to the first demonstration of cortical magnetic stimulation in 1985 [90]. Over its 20-years history, TMS has evolved into a tool for human brain mapping, a way to dissect cognitive and perceptual processes and as a treatment for psychiatric diseases [91]. Contrary to electrical stimulations, TMS treatments are relatively painless and easy to perform.

a) b)

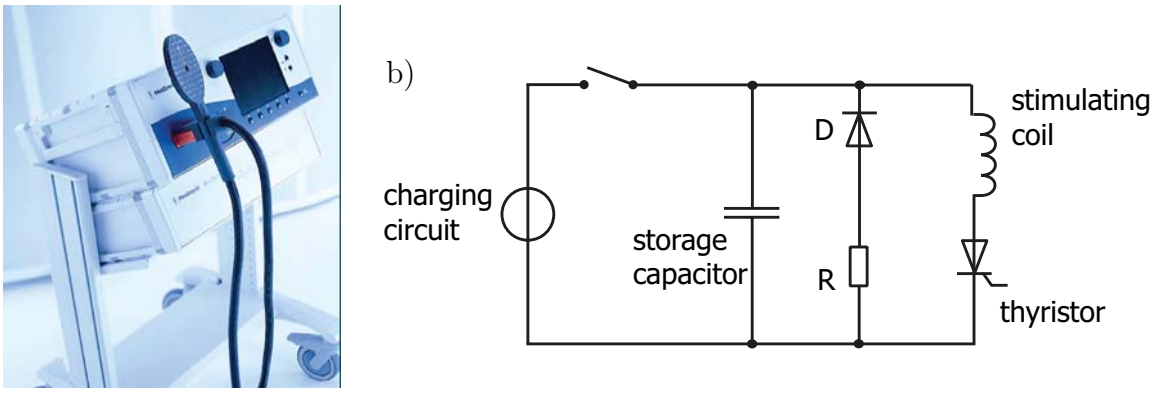

Figure 4.6: Typical TMS equipment. a) Main unit and a connected circular coil. b) Simplified schematic diagram of a magnetic nerve stimulator.

A typical TMS equipment consists of a main unit creating a high current pulse connected to a hand-held stimulation coil, see Fig. 4.6 a). A simplified schematic diagram depicting the four functional units of a magnetic stimulator, is drafted in Fig. 4.6 b). It consists of a charging circuit, an energy storage, a discharging circuit and the stimulating coil. In all commercially available stimulators the energy is stored in large, high-voltage capacitors, typically fed by a charging system connected to the power line. During the discharge, the energy stored in the capacitor is transferred into the coil, typically using a thyristor, which is capable of switching large currents in a few microseconds. The stimulation coil is normally housed in a plastic cover. Due to its low electrical resistance and high heat conduction capacity, copper is the material of choice for the coil windings.

Two different coil designs are in widespread use: a circular coil and a figure-of-eight coil. Circular coils typically consists of approximately ten windings with a radius ranging from 3-5 cm. The size of a figure-of-eight coil is similar, typically consisting of two times

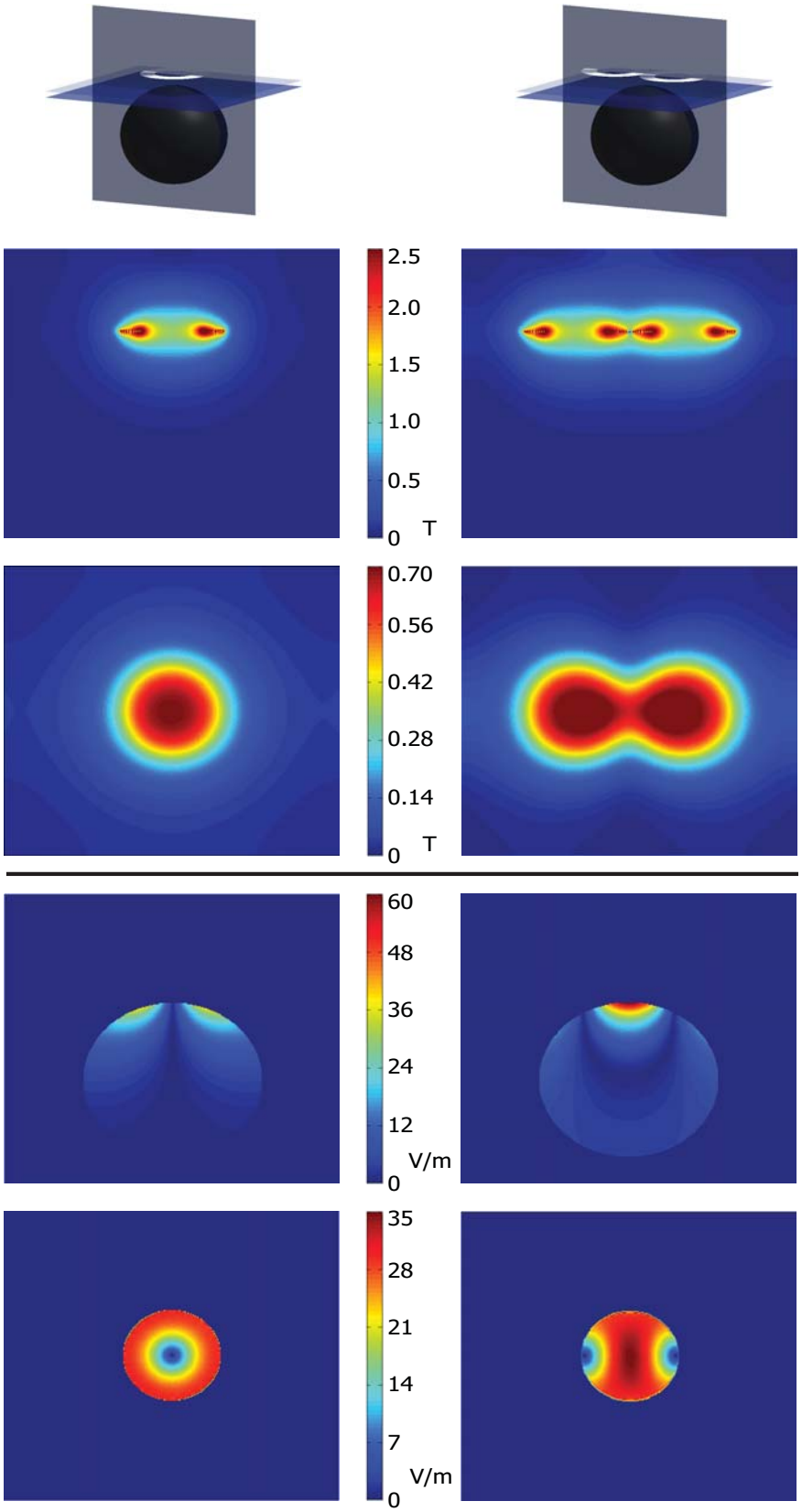

Figure 4.7: Fields of a circular (left) and figure-of-eight coil (right). First and second row: Magnetic field. Third and fourth row: Induced electric field.

ten windings. To illustrate the effect of the coil geometry, the magnetic field and the electric field induced in a homogeneous sphere are plotted in Fig. 4.7. The geometry of the model is sketched in the first row. Cutplanes demonstrate the locations, at which the fields in the plots below are presented. The coil is positioned 2 cm above a sphere with a cross section of 16 cm, that is the typical size of a human head. The conductivity of the sphere was set to 0.0625 S/m, which is the value for white brain matter at 1000 Hz. Typical coil dimensions, as given at the beginning of the paragraph were used, the current in each winding was set to 8000 A. This is the maximal value for the current, as given in common TMS literature. It seems rather high, however, since all calculations are linear, the calculated fields can be easily scaled to a lower excitation current. The computational domain was discretized with a equidistant mesh of 1 mm resolution. Row two depicts the magnetic field calculated using the vector Poisson approach, in the vertical cross-section. Row three in a horizontal cross section at the surface of the sphere. From the horizontal cut, it is evident that the figure-of-eight coil produces a higher magnetic field. Row four and five present the induced electric field inside the sphere. The horizontal plane lies 1 cm below the top of the sphere. The field induced by the figure-of-eight coil is larger than for the circular coil, with a peak at the center of the sphere, below the center of the coil. The maximum amounts to 60 V/m, corresponding to a current density of 3.75 A/m^2. This is higher by more than a factor of thousand than the *ICNIRP* limit. The highest induced field of the circular coil is situated below the winding, with a minimum below the center of the coil. Clinical results have shown, that figure-of-eight coils can be used more accurately, since the stimulated region is situated directly below the center of the coil, where both loops meet. This is in good agreement with the calculated fields.

4.2.3 Transient Calculation of Induced Currents during TMS

Several authors have calculated the induced current distribution during a TMS pulse in a high resolution model of the human brain using numerical methods [92] [59]. However, due to the high computational effort of these calculations only the dominant frequency in the spectrum of the TMS pulse was taken into account. Because of the short pulses used in TMS, a time-harmonic approximation is no longer valid and transient effects have to be considered. The high efficiency of the Ex-SPFD approach makes it possible to perform a full Fourier analysis of the induced currents in a reasonable time. The so obtained results, allow to estimate the impact of the conductivity dispersion on the calculated current densities. Since the stimulation coil is driven by a discharge capacitor, the current pulse inside the coil will exhibit a damped sinusoidal shape, with a peak value of 5-8 kA. In most commercially available stimulators, the pulse duration is approximately 1 ms with a rise time of 50-100 μs. Therefore, the time development of the current inside the coil is calculated by the damped circuit equation

$$I(t) = \frac{V_o}{\omega L} \exp\left(-\frac{Rt}{2L}\right) \sin(\omega t) \tag{4.19}$$

$$\omega = \sqrt{\frac{1}{LC} - \frac{R^2}{4L^2}}.$$

The resistance R, the capacity C and the inductance L of typical equipment, as described in [59] were used (L=185 μF, C=23 μH). In order to produce a so-called monophasic pulse, Kowalski has denoted a resistivity of 0.05 Ω. However, using this value does not

result in the pulse plotted in the same work. Most probably, this is a typesetting error and has to be corrected to a value of 0.5 Ω, which was used here. Other pulse forms, like biphasic or even polyphasic are sometimes used, but have not been considered in this work. Absolute values of the current were normalized to the peak value. For presentation reasons an additional zero current of 12.5 μs duration at the beginning and end of the pulse was added. The transitions from zero current to the pulse calculated by Eqn. (4.19) were filled by intermediate values, in order to reduce the effects of the Gibbs phenomenon. This results in a total signal duration of 1.25 ms sampled by 1000 points, corresponding to a fundamental frequency of 800 Hz. The signal is transformed into the frequency domain using the Fast Fourier Transformation. Since the induced currents are proportional to the time derivative of the current in the coil, the time development of the induced current is obtained by multiplying each frequency component with the factor $i\omega$ and transforming back to the time domain.

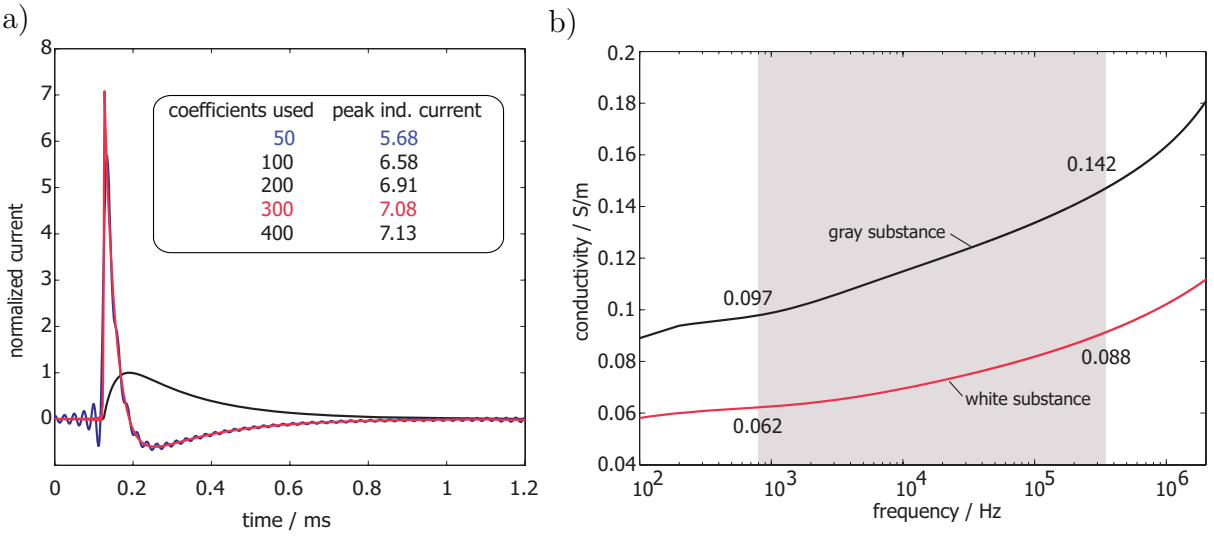

Figure 4.8: a) Time development of the current in the coil (black line) and the induced current constructed using 50 Fourier coefficients (blue line) and 300 Fourier coefficients (red line). b) Conductivity values of white substance (red line) and gray substance (black line) in the frequency range from 100 Hz to 1 MHz. The gray background depicts the frequency range used in the simulation.

Fig. 4.8 a) depicts the time development of the current in the coil and of the induced current calculated using 50 and 300 Fourier components. The inset summarizes the dependence of the peak induced current on the number of used frequency components. Because a high-resolution field calculation has to be performed for each frequency component, the number of used components was limited to 300. For this value, the deviation in the peak current is less than 1 % and the osciallations at the beginning of the signal due to the Gibbs phenomenon are negligible. The frequency dependence of the conductivity of brain tissue is plotted in Fig. 4.8 b). In the frequency range used in the calculation of the induced currents, that is marked by the light gray box, the conductivity increases by almost 50 %. This behaviour can be attributed by the so called β-dispersion arising in biological tissue due to a polarization of large cellular molecules and the cell membrain itself [9]. Since the cerebral spinal fluid (CSF) mainly consisty of water, it does not exhibit this conductivity increase. In this section, an estimation of the impact of the β-dispersion on the magnitude

of the calculated induced currents will be performed. Because white matter mainly consists of directed neurons, commonly packed into bundles, the conductivity is highly anisotropic [93]. Unfortunately, the segmented model can not resolve this anisotropy and an isotropic model was used in the calculations.
In the calculations presented in this section the brain model distinguishing three tissue types was used (brain model one, Sec. 2.2). The excitation is performed by a typical figure-of-eight coil with a current of 8000 A. The coil was placed in an axial plane above the model, at a distance of 4 cm to the brain surface, that corresponds to a distance of approximately 3 cm to the surface of the head. The calculation domain was discretized with an equidistant mesh of 1 mm resolution. In order to minimize the effects of the boundary conditions, free space was added to the computational domain around the brain model. The distance of the boundaries was chosen so, that the induced currents change by less than 1 %. The spatial dimensions of the computational domain amount to 29 cm x 31.5 cm x 24.5 cm, resulting in 22 million grid cells. In the case of magnetic brain stimulation, only low conductive biological tissue is present in the computational domain. Therefore, the shielding effects of the induced currents can be neglected, as described in Sec. 4.1.3. This allows to use the same magnetic vector potential for the calculation of the induced fields at all 300 frequencies. Solutions of the divergence correction for each frequency component are obtained on a cluster consisting of 22 Intel Xeon CPUs running at 3.2 GHz and equipped with 8 GB RAM. Each system of equations is solved using a Successive Over Relaxation (SOR) preconditioned Bi-Conjugate Gradient Stabilized (BiCGStab) method. A relative solver tolerance of 10^{-7} was used. For one frequency component, a calculation time of approximately 5 minutes is needed, resulting in a total time of 25 hours for all frequencies. The largest induced currents occur in the CSF, since CSF exhibits a larger conductivity than white and gray brain tissue (2.0 S/m vs. 0.062 S/m and 0.098 S/m respectively, at 1000 Hz). In order to compare the results to publications by other groups, time-harmonic results at 800 Hz are presented first: Due to this conductivity contrast and the fact that the segmentation process has produced some isolated CSF voxels at a short distance to the coil, the highest current density of 250 A/m^2 in CSF seems rather large, when compared to the current densities inside brain tissue. These amount to 6.99 A/m^2 for white tissue and 32.41 A/m^2 for gray tissue. This values coincide well with results published by Nadeem *et al.* [92]. Nadeem reports a maximum current density in the range of 30-130 A/m^2.
In the first part, the magnitudes of the current densities calculated at the fundamental frequency are compared to the maximal value calculated using the Fourier approach neglecting the conductivity dispersion and to ones incorporating all details. The time development of the induced current densities calculated neglecting the conductivity dispersion can be obtained by taking the solution at the fundamental frequency and multiplying it with $i\omega$ for the needed frequencies. In order to take the conductivity dispersion into account the current densities calculated by the Ex-SPFD approach have to be used for each frequency component. The comparison is performed for a set of selected points. The time development of the induced current density in a point in white matter is plotted is Fig. 4.9. The inset illustrates the spatial position of this point. The dotted horizontal line represents the value of the induced current density at the fundamental frequency of 800 Hz. The red line depicts the time development of the induced current density regarding the conductivity dispersion, while the black line was obtained from a calculation neglecting the dispersion effects. For the both latter results, the calculated pulse form is nearly identical. However, the peak current in the calculation considering the dispersion effects is larger by 14 %.

This value can be interpreted as the impact of the β-dispersion on the magnitude of the induced currents. The absolute (peak) values amount to 0.42 A/m^2 for the single frequency solution, 3.02 A/m^2 for the calculation neglecting dipsersion effects and 3.44 A/m^2 for the full model.

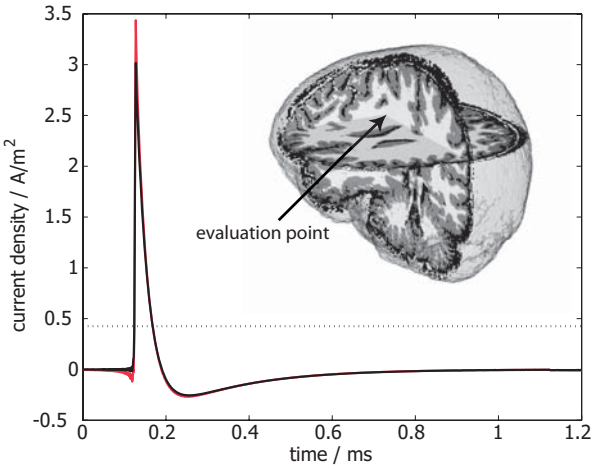

Figure 4.9: Time development of the induced current in a point in white matter.

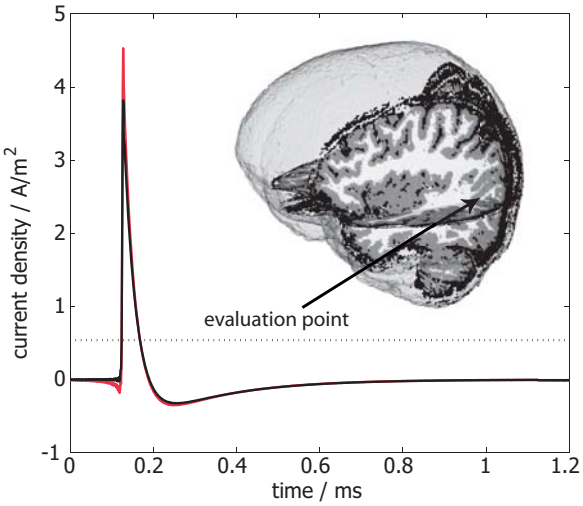

Figure 4.10: Time development of the induced current in a point in gray matter.

The time development of the induced currents for a selected point within the gray tissue is depicted in Fig. 4.10. The labeling is identical to the one used in Fig. 4.9. The absolute (peak) values for the point in gray matter amount to 0.53 A/m^2 for the single frequency solution, 3.82 A/m^2 for the calculation neglecting dispersion effects and 3.53 A/m^2 for the full model. At this point, taking the conductivity dispersion into account results in a peak current that is larger by 18.6 %. Fig. 4.11 depicts the results for a point in the CSF. The chosen point is situated directly below the stimulation coil and since the conductivity of CSF is nearly 20 times higher as the conductivity of gray matter, the induced current densities are substantially higher: 33.83 A/m^2 for the single frequency solution, 239.6 A/m^2 for the solution neglecting the dispersive effects and 240.6 A/m^2 for the full solution. As expected, the effect of the conductivity dispersion on the induced current densities is the CSF is negligible, since it mainly consists of water and does not contain molecules which are polarizable in the kHz frequencies.

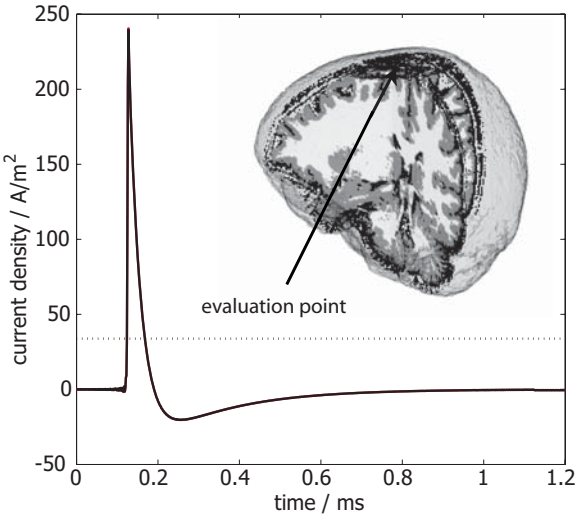

Figure 4.11: Time development of the induced current in the cerebral spinal fluid.

In the second part, the impact of the conductivity dispersion is evaluated for the whole brain model. We compare the difference in the peak currents calculated using the dispersive model to ones calculated neglecting the dispersive effects.

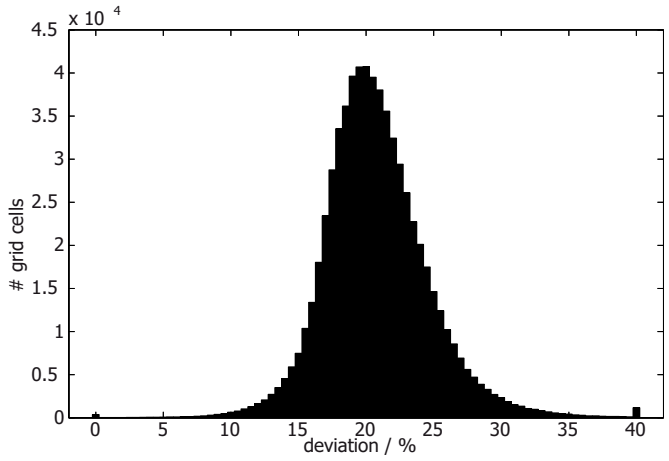

Figure 4.12: Impact of the conductivity dispersion on the peak induced current densities in gray matter.

The impact of the conductivity dispersion on the calculated peak induced current densities in all gray matter cells is depicted using a histogram, presented in Fig. 4.12. On the x-axis, the relative deviation between the dispersive and the non-dispersive model is plotted. The bars on the y-axis give the number of cells in the model exhibiting this deviation. The total number of grid cells filled with gray tissue amounts to 668,710. The arithmetic mean value of the relative deviation in gray tissue was estimated as 20.8 %.

Fig. 4.13 summarizes the impact of the conductivity dispersion on the peak induced currents in white brain matter. A total of 437,400 cells are filled with white matter, the mean value of the relative deviation is 17.3 %, sligthly less than the mean value estimated for gray matter. Surprisingly, the distribution of the deviation in white matter is, contrary to the distribution in gray matter, not symmetric. This effect can be explained by the geometry of the magnetic field and the spatial distribution of the tissue in the brain.

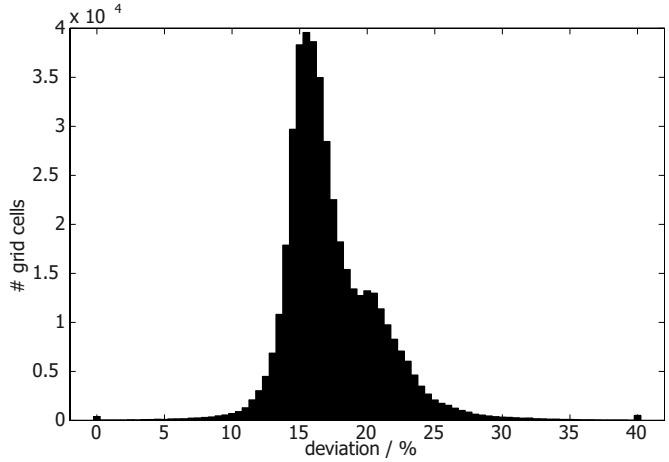

Figure 4.13: Impact of the conductivity dispersion on the peak induced current densities in white matter.

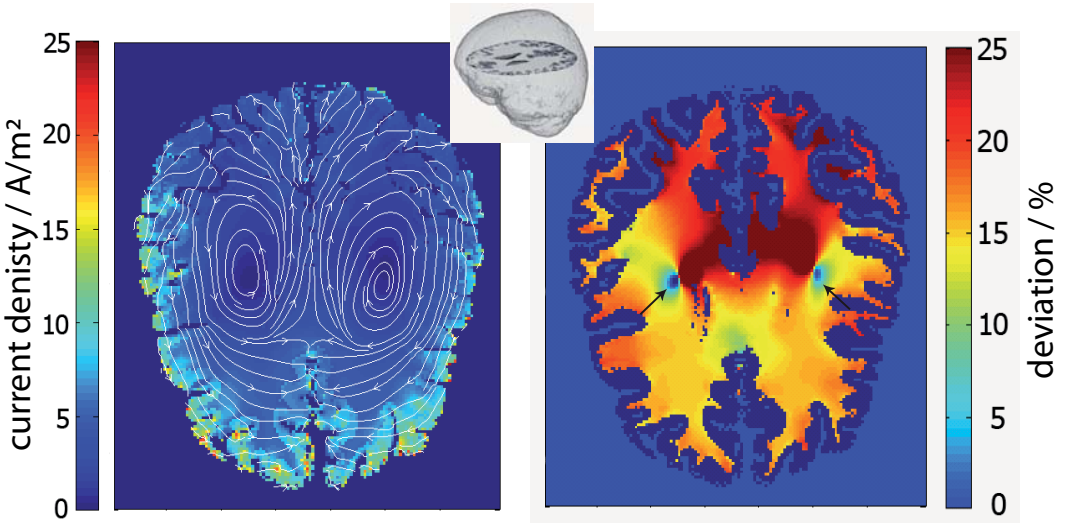

Figure 4.14: Current density distribution and direction (left). Distribution of the impact of the conductivity dispersion (right).

The left side of Fig. 4.14 illustrates the distribution and direction of the peak induced current density in an axial slice of the brain. The position of the slice is depicted by the inset in the upper part of the figure. Since the conductivity of CSF is higher than the conductivity of gray and white matter by almost a factor of 20, the current densities induced in the CSF have been set to zero, in order to better visualize the distribution in brain matter. On the right side of Fig. 4.14, the distribution of the deviation due to the conductivity dispersion in white brain matter is shown. For clarity, also the spatial distribution of gray matter tissue is shown as dark blue areas around the white matter. In the distribution of the plotted deviation two characteristic points at which the deviation changes from zero to more than 20 % are marked by black arrows. Both points are situated below the center of each loop of the coil, where the magnetic field exhibits a minimum. At these points, the direction of the induced currents is spiral with a high radius of curvature. This characteristic distribution is the reason for the non-symmetry of the deviation observed in white

matter, as depicted by Fig. 4.13. This effect can only be observed in white matter, because the spatial distribution of white matter is more homogeneous than the distribution of gray matter. Gray matter is mainly situated around the white matter creating the so-called gyri. In this wound distribution, the effect of the deviation contrast below the loop centers tend to cancel out, resulting in a symmetric distribution of the deviation, as presented in Fig. 4.12.

4.2.4 Mapping Study of the Motor Cortex

After calculating the transient development of the induced currents inside the brain during TMS, simulations of a mapping study of the motor cortex will be presented in this section. TMS mapping of cortical motor areas is based upon the idea of stimulating different regions of the brain, by moving the coil on the head surface and measuring the amplitude of the Motor Evoked Potential (MEP) as the measure of the motor response. The measured MEP's can be compared to the calculated fields inside the motor cortex, allowing to establish a connection between the calculated fields and measured quantities. The presented measurements have been performed at the University of Regensburg, Department of Psychiatry on a healthy male volunteer. Using an electrode on the skin surface, the potential in the nerve of the index finger of the right hand was measured (Muskulus Interosseus 1). By varying the position of the coil on the head surface, the stimulation point eliciting the maximal potential was estimated. Then, the potential in the finger nerve was recorded for an array of 5x5 points around the hot spot, at a distance of one centimeter from each other, using five stimulation pulses at each point. A contour plot of the normalized, arithmetic mean values of the measured MEP's is presented in Fig. 4.15 a). The point eliciting the peak potentials is clearly situated in the center of the stimulated array. The head of the same volunteer was scanned using MRI and a model consisting of the brain, skull bone and dura was constructed, as described in Sec. 2.2. Additionally to the standard MRI scan, also a functional MRI (fMRI) recording was performed. fMRI allows to detect the blood-oxygen-level-depended (BOLD) contrast in the brain, by utilizing the fact that hemoglobin is diamagnetic when oxygenated but paramagnetic when deoxygenated. The BOLD can be interpreted as an indirect measure of neural activity. For fMRI measurements, the used scanner[1] offers a spatial resolution of 3 mm, at a time resolution of several seconds. The relatively poor time resolution can be attributed to the time constants of the blood flow, however in this study it does not represent a drawback, since only the spatial information is of interest. During the fMRI scan, the subject was performing finger tapping movements (touching the thumb with the index finger) in both hands alternatingly. The recorded data was evaluated using the SPM software [26], resulting in a dataset depicting the position of the motor cortex for the left and right finger. The position of the motor cortex was then manually transferred to the brain model used in the calculation. The manual transfer of the spatial position allows to consider the anatomical facts more precisely, than a simple interpolation of the data. For example, neural excitation can not occur in the CSF, therefore care was taken to mark the corresponding positions in white and gray matter only. The so-estimated position of the motor cortex of the right hand is marked by a blue spot in Fig. 4.15 b).

[1] Siemens Allegra

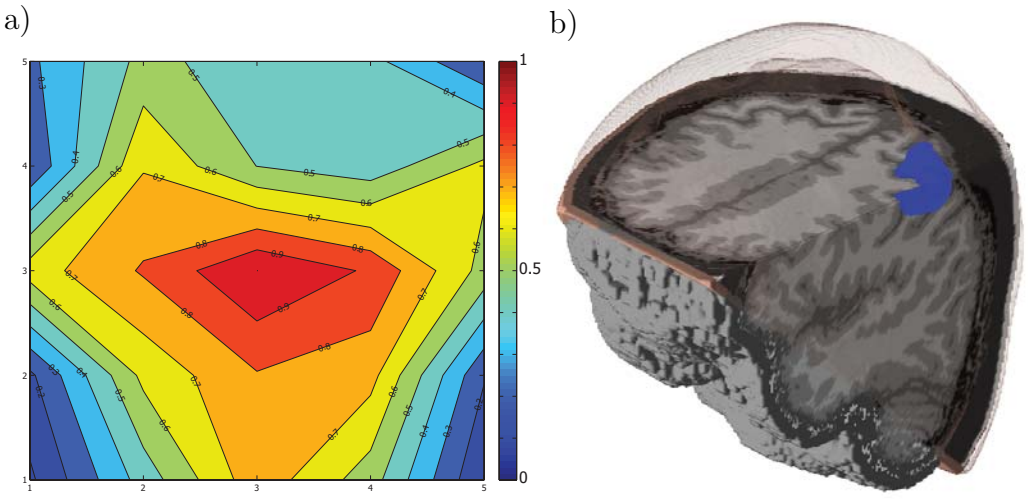

Figure 4.15: a) Measured motor evoked potential in the right index finger. b) Position of the motor cortex of the right hand in the brain model.

In the presented calculations, a spatial resolution of 1 mm was used. Since in the mapping study the position of the coil varies, more free space than in the calculations presented in the previous section was added to the model. The spatial dimensions of the computational domain amount to 32 cm x 35 cm x 36 cm, resulting in 40 million grid cells. The volume of the motor cortex is represented by a total of 2647 voxels, 1057 in white matter, 1590 in gray matter. All calculations are run on 22 compute nodes, equipped with 3.2 GHz Xeon processors with 8 GB RAM. The magnetic vector potential is calculated using the vector Poisson approach. All solutions are obtained using SOR-CG. For a solver tolerance of 10^{-6} in the calculations of the vector potential and a solver tolerance of 10^{-9} for the divergence correction, a total time of 10 minutes is needed for each coil position. In order to minimize the computational effort, only the time-harmonic solution at 1000 Hz is calculated for each position. However, the results from the previous section will later be used to estimate the magnitude of the induced electric field more precisely.

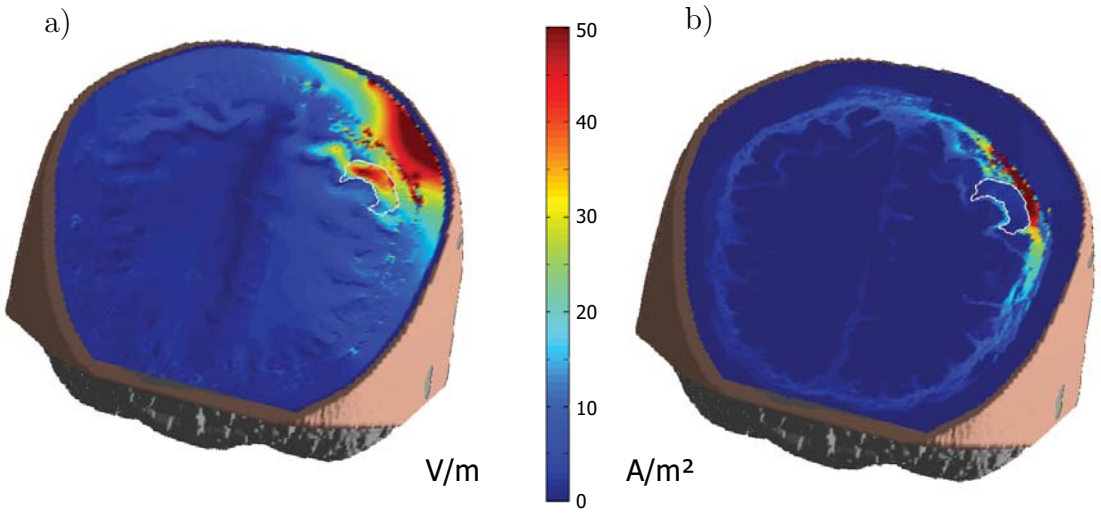

Figure 4.16: a) Induced electric field. b) Induced current density.

As pointed out at the end of Sec. 1.3.2, during the evaluation of the simulation results of the mapping study, the electric field turned out to be the more appropriate quantity for this study. Since the conductivity of the CSF is larger by a factor of 20 than the conductivity of brain matter, a plot of the current density only visualizes the currents in the CSF. In the previous section this problem was circumvented by plotting the current density only in the brain tissue. The use of the electric field however, seems to be the more 'natural' approach, as depicted by Fig. 4.16. The left part of this figure presents the induced electric field for one coil position, the right side the induced current density. The position of the motor cortex in the shown slide is depicted by white contour lines. The plot of the current density only visualizes the currents inside the CSF, while in the plot of the electric field the maximal electric field is clearly visible in the skull bone at the position where the maximal magnetic field is penetrating the tissue. The distribution of the electric field inside the motor cortex is also clearly visible. The use of the electric field also seems to be the physically more meaningful approach, since it is the electric field that imposes a force on the charge carriers and membranes inside the tissue, that lead to a depolarization of the neuron. However, the exact mechanisms of the stimulation, leading to the measured MEP's are still not fully understood and represent an area of active research.

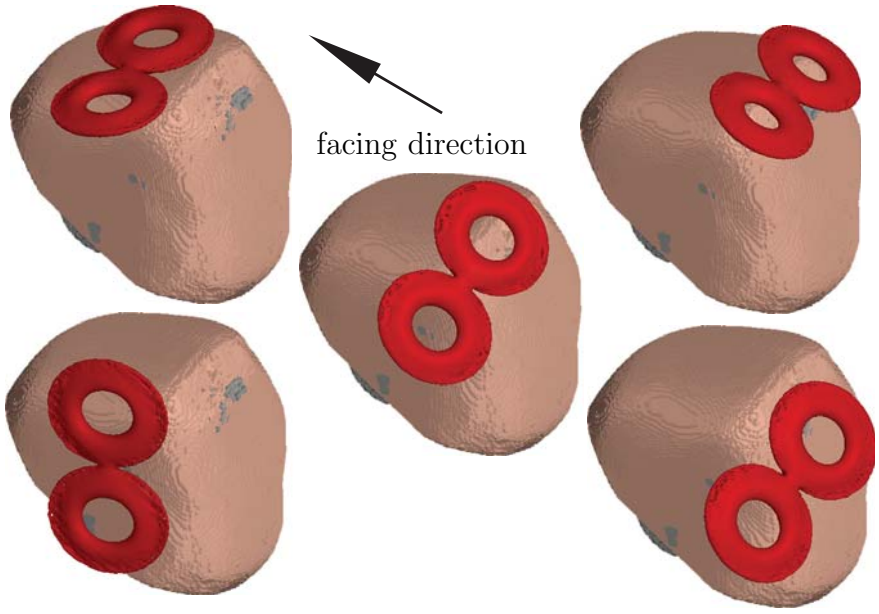

Figure 4.17: The corner and central coil positions in the mapping study. The red surfaces depict the iso-value of the magnetic field of 1 T.

In order to exactly model the geometry of the coil, an X-Ray photography of the coil was acquired. From this image, the exact dimensions of the coil windings were estimated. The loops of the used coil are slightly elliptic with an inner radius of 2.4 cm and an outer radius of 3.85 cm for the smaller axis and 2.75 cm and 4.5 cm for the the larger axis. Notice, that the inner radius of the windings differs noticeably from the inner radius of the plastic cover. During the study a stimulator output of 55 % was used. Assuming a maximal current of 8000 A at 100 % output, the value of 4400 A was used throughout the calculations. For the presentation of the results of the study, the time-hamronic values at 1000 Hz will be used. At the end of the section an evaluation of the transient effects will be performed. The positions used during the study were recorded using a neuro-navigation

system, utilizing two cameras to localize the cartesian position of a rod used to mark each position of the coil. The system displays the position of the rod over the previously acquired MRI dataset. However, the coordinates estimated from these images were clearly spatially misplaced. Therefore, for the positioning of the coil in the simulations, the same approach as in the measurement was chosen. A position on the skull's surface, directly above the estimated site of the motor cortex was selected. Then, the coil position was slightly varied, until the position inducing the largest electric field in the motor cortex was found. Around this position an array of 7x7 points, at a distance of 1 cm from each other was selected. The coil was aligned tangentially to the surface of the skull, at a distance of ≈ 1 cm, with the long axis perpendicular to the anterior-posterior direction. The positions of the coil at the four corners and in the center of the simulated array is depicted in Fig. 4.17. The red surfaces indicate the iso-value of the magnetic field at 1 T.

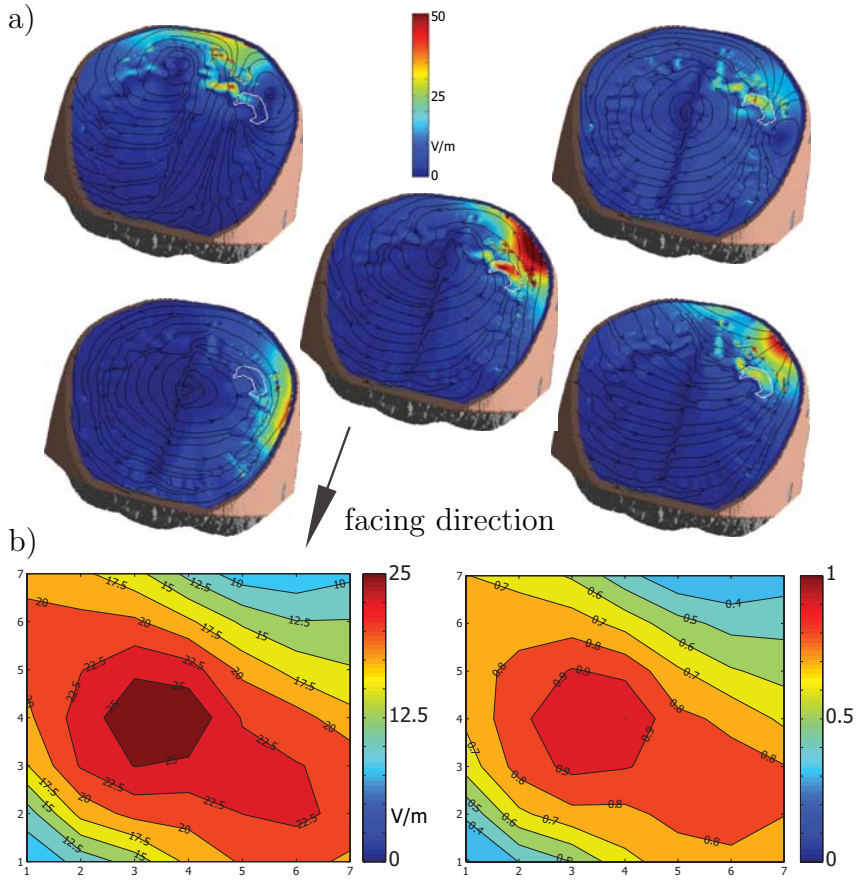

Figure 4.18: a) Induced electric field in an axial cutplane for the coil positions depicted in figure 4.17. b) Mean electric field and normalized mean electric field in the motor cortex.

The induced electric field in an axial cutplane for the coil positions depicted in Fig. 4.17 is plotted in Fig. 4.18 a). The motor cortex is outlined by white contours, the direction of the electric field is depicted by black arrows. The coil in the central position clearly induces the highest electric field in the motor cortex area. A contour plot of the mean electric field and normalized mean electric field inside the motor cortex is presented in part b) of Fig. 4.18. For this plot, the mean value of the electric field in all voxels of the motor cortex was calculated for each coil position. As in the measured MEP's presented in Fig. 4.15 a), the calculated electric field exhibits a maximum in the center of the array and falls of at

the corners. The decrease of the MEP is however more pronounced than the decrease of the mean electric field, when moving away from the central position, as can be observed in the normalized plots. In the corners of the measured array, the normalized MEP takes a value of less than 0.3, while at the same distance from the center of the simulated array the normalized electric field amounts to ≈ 0.7 (remember: measured array: 5x5, simulated array 7x7). The mean electric field in the motor cortex at the central position amounts to 27.1 V/m, the maximal value found in the motor cortex is 74.0 V/m. This are values of the time harmonic solution at 1000 Hz. The contour plots in Fig. 4.18 b) indicate, that the electric field decreases faster when moving to the lower left and upper right corner, than for positions in the upper left and lower right direction. This effect can be attributed to the used positioning technique. A surface mesh produced by FMRIB was used for the estimation of the tangential vector. Unfortunately, the current release of FMRIB can construct the mesh only with a coarse resolution. Thus, in areas in which the skull exhibits a high curvature (Fig. 4.17), the tilt angle of the coil can vary significantly, even for a small displacement. Additionally, the rotational angle of the coil with respect the coil's center have been found to have a distinct effect on the MEP [94]. Therefore, the effect of the coil's tilt and rotational angle on the induced electric field in the motor cortex will be analyzed in the following.

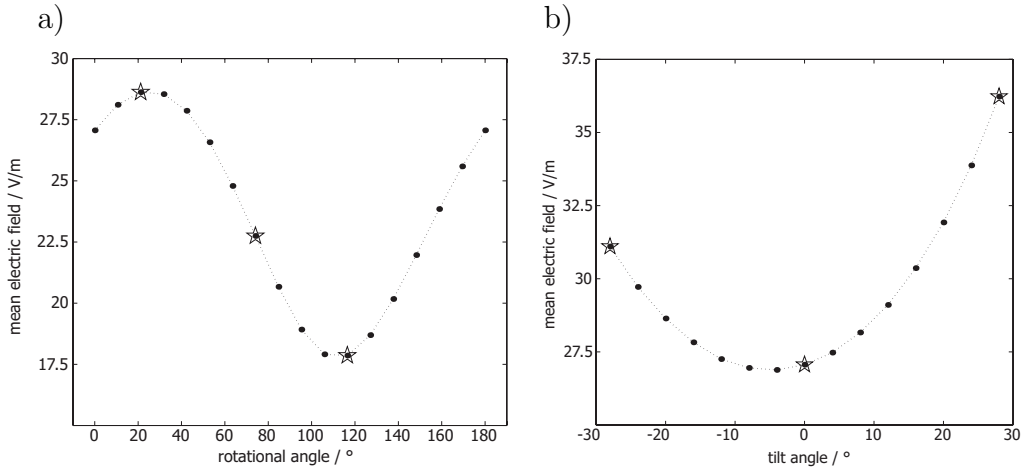

Figure 4.19: Mean induced electric field in the motor cortex a) Effect of the rotational angle. b) Effect of the tilt angle.

The effect of the rotational angle of the coil is depicted in Fig. 4.19 a). The star shaped markers in the curve refer to the positions plotted in Fig. 4.20 a). For the study of the effect of the rotational and tilt angle, the coil was positioned in the center of the 7x7 array. The rotational angle used for the positions of the array was selected as the starting point. A half-circle consisting of a total of 18 rotational angles, with a variation of 10 degrees each was simulated. Since the evaluation of the electric field in the volume of motor cortex can be understood as a projection of the field values, the obtained curve exhibits a sinusoidal profile. The smoothness of the curve indicates that the used spatial resolution is sufficient and that the effects of the stair-case mesh do not affect the solution negatively. The maximal electric field in the motor cortex amounts to 28.6 V/m and is obtained for the third coil position. For a perpendicular coil orientation, the induced electric field is minimal, with a value of 17.8 V/m. The field distribution in an axial cutplane for both extreme cases is plotted in the left and right part of Fig. 4.20 a), respectively. From

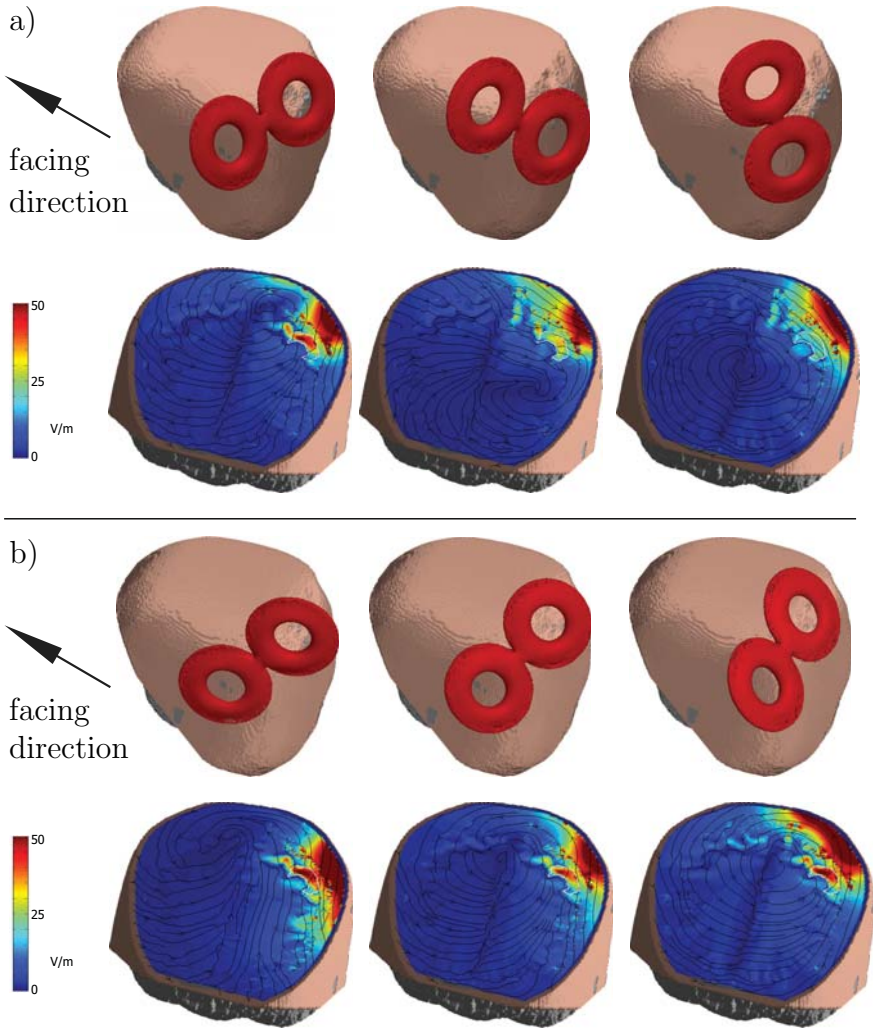

Figure 4.20: Coil orientation and induced electric field in an axial cutplane. a) Effect of the rotational angle. b) Effect of the tilt angle.

this results, it can be concluded, that the rotational angle of the coil, with respect to the anterior-posterior direction has a distinct influence on the magnitude of the induced electric field, coinciding well with experimentally obtained results [94]. The magnitude of the electric field for the extreme orientations varies by more than 10 V/m. Comparing this value to the results obtained from the study of the coil position, the variation due to the rotational angle corresponds to a displacement of the coil that can be larger than 2 cm. The effect of the tilt angle of the coil is depicted in Fig. 4.19 b). The star shaped markers in the curve refer to the positions plotted in Fig. 4.20 b). Also here, the tilt angle used in the study of the coil position was selected as a starting point. The coil's orientation was then tilted by four degrees at each step, with a total of seven steps in each direction. The resulting curve exhibits a parabolic profile, as expected from the geometry. For small angle variations, the variation in the induced electric field also remains low. Only for the three extreme orientations with a positive tilt angle and for the outer point at a negative tilt angle, the variation of the mean electric field in the motor cortex becomes larger than 2.5 V/m. Thus, the effect of the tilt angle is less pronounced than the effect of the rotational angle of the coil.

From the results of the transient calculations performed in the last section, it can be concluded that the actual peak values of the induced fields are larger by a factor of 7, than the time-harmonic solution. Therefore, the peak mean value of the electric field can be estimated as ≈ 150 V/m, the peak maximal value as ≈ 414 V/m. Using the conductivity of white matter at 1000 Hz, the current densities read $\approx 14.7\text{A/m}^2$ and ≈ 40.5 A/m^2 for the peak mean and peak maximal values respectively. Since the excitation of nerves follows an all or nothing law [95], an alternative way to evaluate the simulation results which reflects the mechanism of stimulation in a physiologically more meaningful way than using the mean induced electric field was also performed. This is done by counting the number of grid cells lying above a certain threshold and comparing the so-obtained distribution with the measured MEP's. For the comparison, the peak values as obtained from the transient calculations were used.

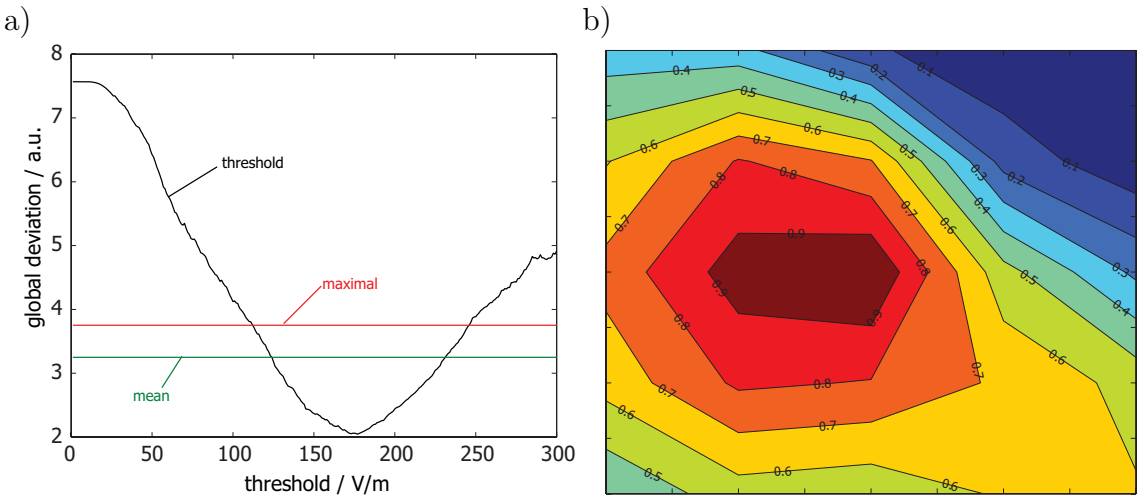

Figure 4.21: a) Global deviation of the normalized, calculated distributions of the electric field to the measured MEP distribution. b) Contourplot of the normalized number of grid cells with an induced electric field larger than 177 V/m.

Fig. 4.21 a) depicts the global deviation of the normalized, calculated electric distributions of the electric field to the measured MEP distribution. The global deviation is obtained by summing the quadratic deviation at each of the 25 positions in the array, as:

$$D = \sum_{n=1}^{25} \left(x_n^{\text{measured}} - x_n^{\text{simulated}} \right)^2 . \tag{4.20}$$

This value can be understood as a measure of the similarity of the calculated distributions to the measured distribution. The global deviation was calculated for thresholds in the range from 1 to 300 V/m. In the plot presented in Fig. 4.21 a) a minimum of the global deviation can be observed at 177 V/m. Thus, for this threshold value, the agreement of the calculated and measured distribution is maximal. The distibution of the normalized voxel count for this threshold can be found in Fig. 4.21 b). In [96], a threshold value for the stimulation of neural tissue of 100 V/m is given, however, without any details on the pulse form, or duration. Therefore, both values can not be compared directly. For the estimation of the threshold values, the peak electric fields, as obtained from the transient analysis were used. These peak values occur only for a few μs (see Fig. 4.8) and may

overestimate the actual threshold. In order to evaluate the maximal and mean electric fields, as presented in Fig. 4.18, the global deviation was also calculated in these both cases. The distribution of the mean electric field exhibits a lower global deviation than the distribution of the maximal electric field. However, the deviation obtained from the threshold analysis at suitable thresholds is substantially lower.

The results presented above, indicate that a link between the electric field calculated inside the motor cortex and the measured MEP's can be established. However, due to the lack of accurate input data, only qualitative conclusions could be drawn. Still, the performed study showed that at the spatial resolution applied in the simulations, the calculated induced electric field in the motor cortex exhibits a significant variation due to the orientation and position of the coil. In future work, the performed study should be repeated, while taking care to record all details that have been neglected in the presented calculations. First, the used MRI data was slightly rotated with respect to the voxel coordinates. A new scan, with the world space aligned to the voxel space would lead to more accurate results. Second, the recorded positions of the coil using a rod were clearly spatially misplaced. In the future study, the coil position and also it's orientation should be recorded in a more suitable way, for example by using markers on the surface of the head. Third, the shape of the current in the coil has to be estimated more precise. This could be performed by recording the actually used stimulator output, along with data of the built-in inductance, capacity and resistivity. Or, even better, by measuring the actual current in the coil. Taking all this points into account promises to accurately estimate the electric field strength leading to a given MEP. Furthermore, the study should be performed on several probands, allowing to compare the calculated fields and optimal thresholds among various persons. Additionally, the evaluation of the calculated electric fields could be refined. All results presented in this section were based on the magnitude of the induced electric field. However, also the direction of the induced electric field is supposed to play a role in the activation mechanisms. Other concepts, like Rattay's "activation function" [97] should also be tested for it's applicability.

Chapter 5

Summary and Outlook

Summary

The here presented thesis contributes to the modeling of the interaction of low-frequency electromagnetic fields and the human body in several aspects: Two novel computational methods which allow for a finer spatial resolution in the simulations were proposed. The impact of approximations applied to the modeling of the electromagnetic fields was analyzed and two application set-ups that allow to compare the simulation results to measurements were proposed.

At the beginning, after a short historical introduction, the low-frequency regime was classified in the electromagnetic spectrum. Using simplified mathematical models, the magnitudes of the fields inside biological tissue were estimated. In a short discussion of the effects of low-frequency electromagnetic fields on the human body, the current density was introduced as the commonly used dosimetric quantity and basic restriction levels proposed by international agencies were presented. Most of the results throughout this thesis were presented in terms of the induced current density. However, during the evaluation of the mapping study in Sec. 4.2.4, the electric field turned out to be probably the more appropriate quantity, particularly when the stimulation of neural tissue is of interest.

In the second chapter, the applied modeling framework was presented. Literature about the dielectric properties of tissue, representing crucial input for the simulations was shortly reviewed, along with some remarks on the measurement techniques used. The parametric Cole-Cole model proposed by Gabriel, which is used throughout this thesis was introduced. It was followed by a section dealing with phantoms of the human body, that are used to map the geometry of the human anatomy to a model that can be used for the calculation of physical quantities. Throughout this thesis, two phantoms of the human brain were constructed from MRI data using semi automated tissue segmentation. Both models were used in Sec. 4.2 for the calculation of induced fields inside the brain during a TMS treatment. The last part of the modeling chapter was devoted to the basic properties of the FIT, which is used as a geometric discretization scheme of the Maxwell equations in the presented calculations. Finally, a short overview of computational methods used by other groups for the calculation of electromagnetic fields in the human body was given.

Several aspects of electrically excited systems were treated in chapter 3. The term electric excitation labels applications set-ups in which the current flow inside the body is imposed by a contact of the body with a potential difference. After an introduction of the electro quasi-static formulation, the impact of the displacement current on the magnitude of the calculated fields was analyzed. Only at the extreme low frequency of 10 Hz the

deviation of the complex-valued and real-valued model was larger than 5 %. However, this deviation can be mainly attributed to the uncertainties in the dielectric data at such extreme frequencies. For all other frequencies, the error due to a neglect of the displacement current is $\approx 2-3\%$. This findings are independent of the model resolution and can also be applied to organ-wise evaluations, that are common in dosimetric publications. Therefore, the displacement current was neglected throughout this work, allowing to use real-valued systems for which efficient solution techniques can be employed.
In order to increase the spatial resolution in the simulations, a local subgridding approach for electro quasi-statics was proposed. In this approach, a particular region of interest is resolved finely, while the mesh in the surrounding is kept coarse. Both regions are coupled by an interface condition at the corresponding boundaries. The system matrices in both regions, along with the coupling condition are all assembled into one matrix, resulting in a saddle-point formulation that allows to obtain the potential distribution in both domains from the solution of one system of equations. The used interpolation scheme and the modifications applied to the computational grids, necessary for the coupling were presented. However, due to the consistency error introduced by the bilinear interpolation at the interface of both grids the proposed approach exhibits only a first order convergence, as could be concluded from a validation with an analytic example. Additionally, the re-assembled system matrix becomes indefinite, requiring special solution techniques that turn out to be inefficient.
In the last part of the third chapter, the bioimpedance was used as a direct link between simulations and measurement results. The segmentally performed analysis showed a good agreement of the calculated impedance values and the anatomic details of the body. In order to reflect the uncertainties in the values of the dielectric properties, a sensitivity analysis in the leg section was performed. From this analysis, it was concluded that during a bioimpedance measurement more than 90 % of the current flows in muscular tissue. A comparision of the caclulated and measured impedance revealed a discrepancy by a factor of 1.5 to 2. The discrepancy could be attributed to the differences in body composition of the used model and the probands and also to the general uncertainities of the dielectric data. Finally, a simple geometric phantom for the calculation of segmental impedance was presented.

An exposure of the body to a time-varying magnetic field results in the induction of currents inside the weakly conductive tissue. In this thesis, this process was labeled as magnetic excitation. Two approaches for the calculation of induced currents were presented in the fourth chapter. The SPFD approach, originally proposed by Stuchly and Dawson and the electromagnetic curl-curl equation derived directly from Maxwell's equations. Both approaches were then combined to yield the Ex-SPFD approach. Ex-SPFD is a two step algorithm, allowing to efficiently calculate the induced currents originating from a low-frequency magnetic field exposure. In the first step, an approximate vector potential is calculated from the curl-curl equation. This approximation already describes the magnetic field with a sufficient accuracy and is then used on the right hand side of the classical SPFD equation. Thus, the second step can be understood as a divergence correction inside the conductive material. The Ex-SPFD approach was extensively validated for several scenarios at different frequencies and for computational domains including highly conductive or permeable materials, for which the classical SPFD approach fails. Applying the two step strategy, drastically reduces the computational time. For the calculation of the induced currents at 50 Hz, an acceleration factor of 200 was obtained, when com-

pared to a pure curl-curl solution. The validation also addressed the question whether the shielding effect of the induced currents can be neglected, or should be incorporated in the calculations. It was found, that for a computational domain including only the biological material, the shielding effect is negligible and thus a free-space magnetic field can be used, which can be calculated from a real-valued formulation. Following the validation, an alternative way to calculate the magnetic vector potential using a vector Poisson approach was presented. It can be employed, when the permeability in the computational domain is constant. In the vector Poisson approach, the three spatial components of the vector potential are calculated successively, rendering this approach more memory efficient than using the curl-curl equation in the first Ex-SPFD step. Furthermore, the system matrices in the vector Poisson approach are positively (semi)definite, reducing the computational time needed for the calculation of the vector potential by a factor of $\approx$ two when compared to curl-curl, especially for very large systems. The Ex-SPFD approach was implemented in a parallel environment, allowing to solve one system by simultaneously exploiting the resources of several workstations. A study of the performance of several solver-preconditioner combinations using different processor numbers can be found in App. A.
Two different applications were analyzed using the Ex-SPFD approach. For the dosimetric analysis of an electric blanket, a whole-body model consisting of 208 million grid cells, corresponding to a resolution of 1.5 mm was solved. Using two different wiring scenarios, it was demonstrated that the exact modeling of the magnetic field sources is essential. An organ-wise evaluation of the results was also performed, showing that under the simulated exposure conditions, the calculated induced currents are lower by nearly thee orders of magnitude than the basic restriction levels. The second part of the application section in this chapter was devoted to the simulation of Transcranial Magnetic Stimulation (TMS), a medical treatment in which high magnetic fields produced by a hand held coil are used to stimulate cortical areas by inducing currents in brain tissue. In order to analyze the geometry of the induced fields from two different coil designs, a simplified sphere model was used. Since the stimulation coil is fed by a discharge capacitor, the current in the coil was modeled by the damped circuit equation. A typical monophasic pulse was decomposed in 300 Fourier coefficients, from which the transient development of the induced currents was calculated. The peak current densities were estimated to be larger by a factor of six than the time harmonic solution at the fundamental frequency. Furthermore, the impact of the β-(conductivity)dispersion on the magnitude of the induced currents was estimated to lie in the vicinity of 20 %. In the last part, a mapping study of the motor cortex was simulated. During a mapping study the position of the coil on the surface of the head is varied and the elicting motor evoked potentials are measured by electrodes on the skin's surface. This measurements were compared to the mean induced electric field in the motor cortex volume which was estimated from a fMRI scan. The comparison exhibitited a qualitative agreement. Applying a threshold for the evaluation of the electric field, it was shown that the agreement of measured and simulated data becomes better. Additionally to the simulated positions, also the effect of the orientation of the coil was analyzed.

Outlook

Particularly the performed mapping study of the motor cortex, presented in Sec. 4.2.4 promises to provide further insight into the interaction of electromagnetic fields and the human body. The study should be repeated with the coil positions and orientations used in the actual measurements. From such a comparison, it would be possible to estimate a macroscopic threshold value of the electric field, that leads to a stimulation of neural tissue. Furthermore, it was observed that the stimulator output needed to elicit a given MEP varies significantly among probands. By comparing the fields obtained in models from different probands, the question whether the observed differences can be attributed to the personal brain geometry or rather to a difference in the threshold value could be clarified. Once a threshold value is estimated, the proposed method could be used to optimize the coil positions in treatments of cortical sections other than the motor cortex. Additionally, an optimization of the coil's geometry could be performed and the applicability of multiple coils could be tested.

Throughout the presented thesis, the need for more accurate dielectric data was stressed in several sections. The dielectric properties of tissue represent a crucial input parameter in all simulations. Especially in the low frequency regime, the used data is affected by measurement uncertainties and for some tissue types even no measurements are available. More accurate dielectric data would significantly increase the quality of the calculated results. Sekino's approach, to measure the electric conductivity with diffusion gradients in a MRI, which was briefly introduced in Sec. 2.2 is a possible way to obtain a phantom along with the appropriate dielectric data from one single measurement. However, at the moment the spatial resolution in this measurements is not satisfactory.

From the numerical point of view, the research should concentrate on efficient solution techniques for large systems of equations. The implementation on a parallel architecture allows to even further increase the system size by simply adding more processors. Nowadays, this seems to be even cheaper than developing new codes. However, as the system sizes increase beyond 200 million unknowns, the performance of CG-type solvers furthers decreases, resulting in the need for robust and efficient multigrid methods.

Appendix A

Solution of Large, Linear Systems of Equations

A very fine spatial resolution inherently leads to very large systems of equations. For the calculation of the induced currents using the Ex-SPFD approach, not the computational time but the memory requirement becomes the limiting factor. Therefore, the Ex-SPFD scheme was implemented in a parallel environment. This allows to distribute the system of equations along multiple workstations and solve it simultaneously. The implementation uses libraries from the PETSc [63] and Hypre [98] packages. PETSc offers a collection of data structures for parallel matrices and vectors and also several preconditioners and (Krylov-) solvers. Hypre is a collection of high-performance preconditioners, that can be accessed from PETSc by an interface. Although PETSc offers 18 different solvers and 19 different preconditioners, not all of them work in parallel and not all combinations can be used. In the following the performance of four different preconditioner-solver combinations will be tested for the vector Poisson system and the divergence correction:

- Symmetric Successive Over-Relaxation (SSOR) - Conjugate Gradient (CG)
- Incomplete LU (ILU) - Conjugate Gradient (CG)
- Jacobi (Jacobi) - Conjugate Gradient (CG)
- Algebraic Multigrid (AMG) - Flexible Generalized Minimal Residual (FGMRES)

Since the examined systems are all positive (semi-)definite, the Conjugate Gradient (CG) method exhibits the best performance, as expected from theory. However, CG requires a positive definite preconditioner and could not be used along with the Algebraic Multigrid (AMG) preconditioner contained in Hypre. Numerical tests showed, that for AMG a FGMRES solver yields the best results. The performance of AMG-FGMRES seems to be connected to the fact that FGMRES is the only implemented solver that can deal with non-linear preconditioners.
The exposure of the body to the magnetic field of an electric blanket, as presented in Sec. 4.2.1 was selected as the test scenario for the performance measurements. In all tests, the model was meshed with an equidistant grid. All calculations were performed on Intel Xeon 3,2 GHz processors equipped with 8 GB memory and connected by Infiniband. All presented times refer to the wall-clock time.

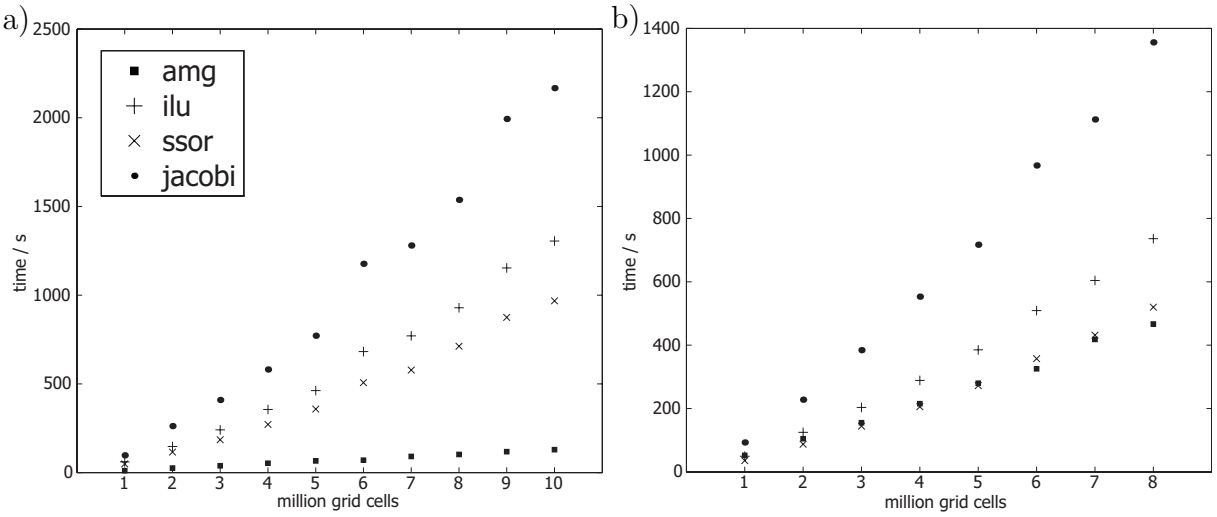

Figure A.1: Calculation times on single processor. a) divergence correction, b) vector Poisson system (three components).

Fig. A.1 depicts the calculation times for the vector Poisson system and the divergence correction on a single processor, for the four tested solver types. The divergence correction was calculated with a solver accuracy of 10^{-9}, the relative residuum in the solution of the vector Poisson system was chosen to 10^{-6}. This are typical values used in the Ex-SPFD approach. For the divergence correction, the AMG-FGMRES method exhibits the by far best performance. For 10 million grid cells, it is faster by a factor of 7.5 when compared to SSOR-CG, for ILU-CG by a factor of 10.1 and for Jacobi-CG by a factor of 16.8. It is well known from theory that multigrid methods offer an asymptotic complexity of ≈ 1, thus for a system of doubled size the computational time is also doubled [99]. For the presented AMG results a value of 1.06 was estimated from a double logarithmic least-squares fit, which is nearly optimal. For the Conjugate Gradient method, the estimated asymptotic complexity amounts to 1.34 for ILU and Jacobi and 1.31 for SSOR. Therefore, the increase of the computational time is not linear, as can be concluded from the CG results, where the curves exhibit a rather parabolic profile. However, at this system sizes the effect is not very distinct. The presented times for the vector Poisson system are a summation of the time needed for all three components. Here, the SSOR-CG and the AMG-FGMRES solution exhibit a similar performance. The AMG-FGMRES solution time for the three systems of the vector Poisson approach is larger, than three times the solution time for the divergence correction, although a higher relative residuum was used for the vector Poisson systems. It is a typical feature of multigrid methods, that the set-up times are larger than the solving times, contrary to the other tested preconditioners, where the set-up times are approximately one third of the solution time. Therefore, AMG will perform better for higher solver accuracies. However, the set-up time of the AMG for the vector Poisson systems is substantially larger than for the divergence corrections. Furthermore, the memory consumption is larger in the vector Poisson case. This allows to conclude, that the used coarsening strategy for the construction of the coarse levels needed in the multigrid scheme works better for matrices with some contrast in their entries, as it is the case in the system matrix of the divergence correction. The entries in the matrices of the vector Poisson approach are all equal, making it hard to find so-called strongly connected nodes that are used for the construction of the coarse levels. A simplified

coarsening strategy, would be a possible remedy for this problem. However, the interface between PETSc and Hypre does not allow such sophisticated tweaking. The effect of the asymptotic complexity can also be observed in the vector Poisson results: The time for the AMG solution at 1 million cells is larger than the time needed for SSOR-CG. At 5 million cells it is equal, while for 8 million cells AMG becomes faster. The estimated asymptotic complexities of all CG based solutions exhibit an improvement from 1.33 to 1.28, while the AMG complexity remains at 1.06.

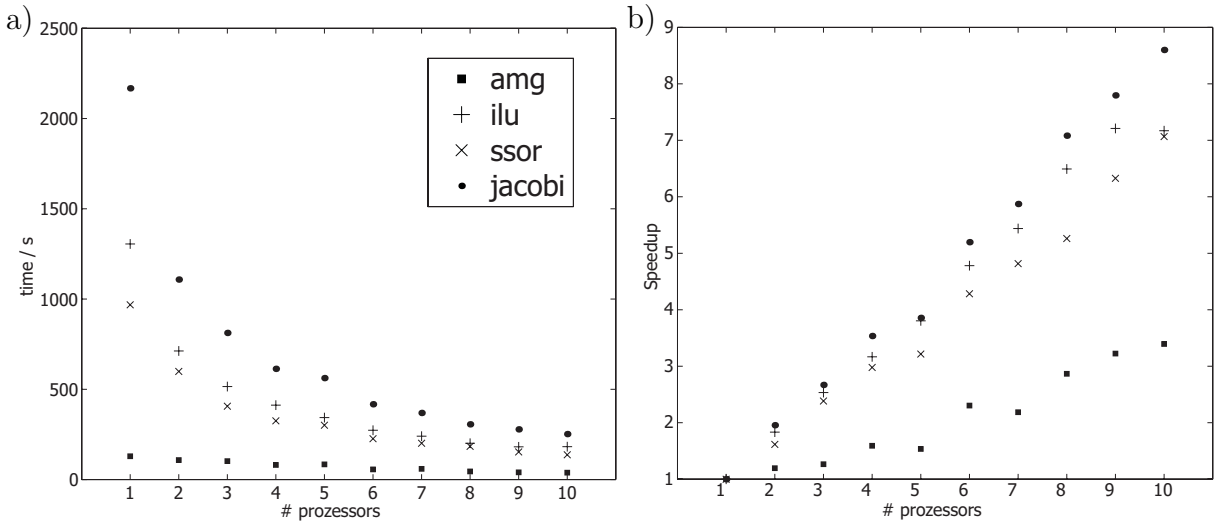

Figure A.2: Results on multiple processors for divergence correction. a) calculation times, b) speedup.

The computational times and the speedup for the divergence correction of a system consisting of 10 million cells on 1 to 10 processors is summarized in Fig. A.2. Speedup labels the acceleration of the calculations, when multiple processors are used. It is defined as

$$S_n = \frac{execution\ time\ on\ one\ processor}{execution\ time\ on\ n\ processors}. \tag{A.1}$$

As in the single processor case, the AMG-FGMRES combination yields the best results. Even the single processor solution using AMG is slightly faster than SSOR-CG on 10 processors (129 s vs. 137 s). However, the speedup of AMG is rather poor. Using 10 processors, a speedup by a factor of only 3 is obtained. The poor speedup of AMG results from the fact, that the preconditioning on multiple processors is performed only block-wise on each processor, with a very small overlap of the blocks. This transition from a global to a local preconditioning severely affect the performance of this preconditioner. As expected, the Jacobi-CG results exhibit the best speedup of 8.5 in the 10 processor case, however also the largest computational times. Jacobi preconditioning is a simple multiplication with the inverse of the main diagonal of the system matrix. This operation can be performed locally on each processor, therefore the deviation of the speedup from the optimal value of 10 can be directly attributed to the time needed for the communication among the processors. For the ILU and SSOR preconditioners the effect of the transition from global to local preconditioning is not as pronounced as in the AMG case, resulting in a speedup of ≈ 7 for 10 processors.

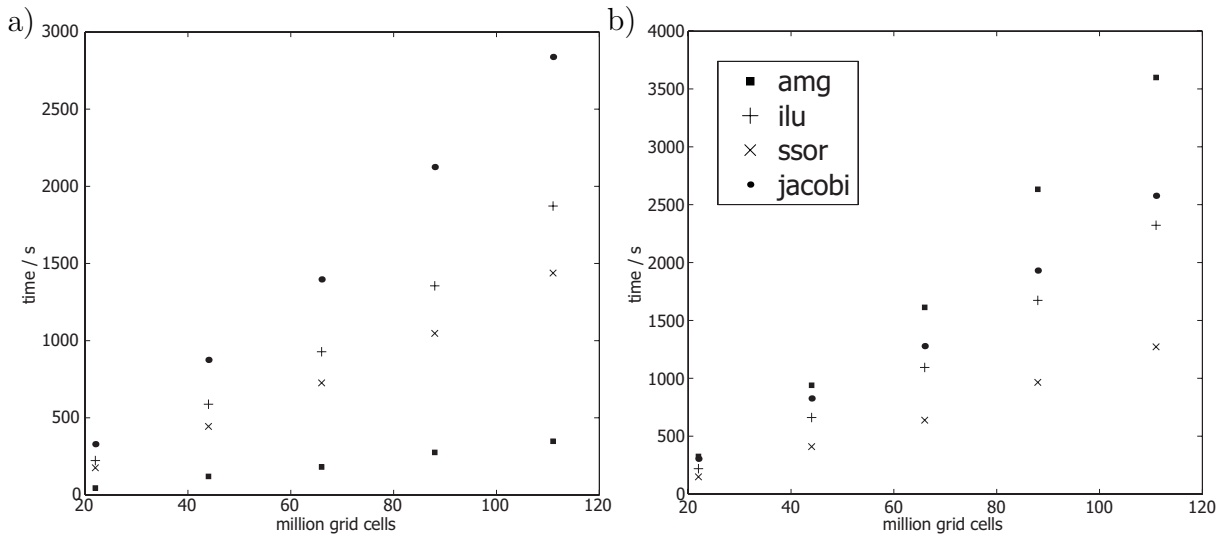

Figure A.3: Calculation times of very large systems. a) divergence correction, b) vector Poisson system (three components).

The last presented study of computational times deals with very large systems consisting of 22 - 111 millions unknows, all solved using 22 processors. As before, AMG performs best for the divergence correction. However, due to the poor speedup of this preconditioner, the asymptotic complexity is noticeably decreased from 1.06 on a single processor to 1.26. For the largest system, consisting of 111 million grid cells, the AMG solution is faster by a factor of 4.1 when compared to SSOR, 5.3 compared to ILU and 8.1 when compared to Jacobi. Thus, the acceleration factor is roughly halved, when compared to single processor results at 10 million grid cells. The asymptotic complexity of the CG based solutions remains around 1.3. For the large vector Poisson systems, AMG exhibits the worst performance, even slower than Jacobi-CG. At this system sizes, the large set-up time of and the poor speedup of the AMG preconditioner further degrade the asymptotic complexity to 1.49, substantially higher than the value of 1.32 estimated for SSOR-CG. For the largest system, the SSOR-CG solution is the fastest, with an acceleration factor of 1.8 when compared to ILU, 2.0 compared to Jacobi and 2.8 when compared to AMG.
The analysis of the computational times for the various systems presented here indicates, that the choice of the optimal solver for large systems of equations is problem depended. For matrices not containing any material coefficients, as in the vector Poisson system the SSOR-CG solver performs best. For matrices with large coefficient variations, as in the divergence correction AMG-FGMRES yields the best results.

Applied Notations and Symbols

General Mathematical Symbols

$\mathbb{R}, \mathbb{C}$	Set of real, complex numbers
$\vec{r}, \mathbf{r}$	Spatial vector
$\vec{n}$	Unit vector of an area
$\mathbf{M}, \mathbf{D}$	Matrix, diagonalmatrix
$\mathbf{x}^T, \mathbf{M}^T$	Transpose of vector $\mathbf{x}$ and matrix $\mathbf{M}$
$\mathbf{M}^{-1}$	Inverse matrix of $\mathbf{M}$
∇, Δ	Nabla operator, Laplace operator
$d\vec{s}, d\vec{A}, d\vec{V}$	Infinitesimal length, surface and volume elements
$\partial A, \partial V, \partial\Gamma$	Boundary of the area, volume, domain

Continuous Field Theory

$\vec{E}$	Electric field strength
$\vec{D}$	Electric flux density
$\vec{H}$	Magnetic field strength
$\vec{B}$	Magnetic flux density
$\vec{J}$	Electric current density
$\vec{I}$	Electric current
q	Electric charge
ρ	Electric charge density
P	Power
φ	Electric scalar potential
$\vec{A}$	Magnetic vector potential
ψ_{corr}	Correction potential
λ	Wavelength
f	Frequency
ω	Angular frequency
$\vec{P}$	Electric polarization of the medium
$\vec{M}$	Magnetization of the medium
μ, μ_0, μ_r	Permeability, permeability of vacuum, relative permeability
$\varepsilon, \varepsilon_0, \varepsilon_r$	Permittivity, permittivity of vacuum, relative permittivity
κ	Electric conductivity
ρ	Specific resistivity
ρ_m	Mass density

Finite Integration Technique

G,$\widetilde{G}$	Primary grid, dual grid
N_p	Total number of nodes
P_n,$\tilde{P}_n$	Primary / dual grid nodes
L_n,$\tilde{L}_n$	Primary / dual grid edges
A_n,$\tilde{A}_n$	Primary / dual grid facets
V_n,$\tilde{V}_n$	Primary / dual grid cell (volume)
$\widehat{\mathrm{e}}, \widehat{\mathbf{e}}$	Element, vector of electric grid voltage
$\widehat{\mathrm{h}}, \widehat{\mathbf{h}}$	Element, vector of magnetic grid voltage
$\widehat{\widehat{\mathrm{d}}}, \widehat{\widehat{\mathbf{d}}}$	Element, vector of electric facet flux
$\widehat{\widehat{\mathrm{b}}}, \widehat{\widehat{\mathbf{b}}}$	Element, vector of magnetic facet flux
$\widehat{\widehat{\mathrm{j}}}, \widehat{\widehat{\mathbf{j}}}$	Element, vector of facet currents
$\widehat{\mathrm{a}}, \widehat{\mathbf{a}}$	Element, vector of magnetic grid potential
$\mathrm{q}, \mathbf{q}$	Element, vector of electric grid charges
$\underline{\phi}$	Nodal, electric scalar potential
$\underline{\psi}$	Correction potential
$\underline{\widehat{\mathbf{a}}}_{\mathrm{corr}}$	Approximate vector potential
$\widehat{\mathbf{a}}_{\mathrm{app}}$	Averaged permittivity
$\bar{\varepsilon}$	Averaged conductivity
$\bar{\kappa}$	Discrete curl operator on the primary / dual grid
$\mathbf{C}, \widetilde{\mathbf{C}}$	Discrete divergence operator on the primary / dual grid
$\mathbf{S}, \widetilde{\mathbf{S}}$	Diagonal matrix of primary/dual grid facets
$\mathbf{D}_A, \mathbf{D}_{\widetilde{A}}$	Diagonal matrix of primary/dual grid edges
$\mathbf{D}_S, \mathbf{D}_{\widetilde{S}}$	Diagonal matrix of averaged permittivities
$\mathbf{D}_{\varepsilon}$	Diagonal matrix of averaged conductivities
$\mathbf{D}_{\kappa}$	Material matrix of permittivity
$\mathbf{M}_{\varepsilon}$	Material matrix of conductivity
$\mathbf{M}_{\kappa}$	Material matrix of reluctivity
$\mathbf{M}_{\nu}$	

Dielectric Dispersion Theory

$\underline{\varepsilon}_{rel}$	Complex-valued relative permittivity
$\varepsilon^{'}$	Real part of the complex relative permittivity
$\varepsilon^{''}$	Complex part of the complex relative permittivity
ε_{s}	Static permittivity
ε_{∞}	Permittivity at infinite frequencies
τ	Relaxation time constant
α	Broadening parameter

Subgridding Scheme

$_{\mathrm{c}}$	Subscript for the coarse domain
$_{\mathrm{f}}$	Subscript for the fine domain
$\mathbf{A}$	System matrix
$\tilde{\phi}$	Potential in the uncoupled system
$\mathbf{b}$	Excitation of each system
$\mathbf{Q}$	Selection operator
$\mathbf{Q}^*$	Modified selection operator
$\mathbf{B}$	Interpolation operator
λ	Lagrange multiplier

Acronyms

FIT	Finite Integration Theory
FEM	Finite Element Method
FDTD	Finite-Difference Time-Domain
SPFD	Scalar-Potential Finite-Differences
Ex-SPFD	Extended Scalar-Potential Finite-Difference
PEC	Perfect Electric Conductor
AMG	Algebraic Multigrid
BiCGStab	BiConjugate Gradient Stabilized
CG	Conjugate Gradient
FGMRES	Flexible Generalized Minumum Residuals Method
ILU	Incomplete LU
MINRES	Minimum Residuals Method
QMR	Quasi-Minimum Residuals Method
SOR	Successive Over-Relaxation
SSOR	Symmetric Successive Over-Relaxation
SAR	Specific Absorbtion Rate
CT	Computed Tomography
MRI	Magnetic Resonance Imaging
fMRI	functional Magnetic Resonance Imaging
BOLD	Blood Oxygen Level Depended
TMS	Transcranial Magnetic Stimulation
MEP	Motor Evoked Potential
EEG	Electroencephalogram
MEG	Magnetoencephalogram
ECG	Electrocardiogram
MCG	Magnetocardiogram
ICF	Intracellular Body Fluid
ECF	Extracellular Body Fluid
CSF	Cerebral Spinal Fluid
ICNIRP	International Comission on Non-Ionizing Radiation Protection
WHO	World Health Organisation
FMRIB	Functional Magnetic Resonance Imaging of the Brain
PETSc	Portable, Extensible Toolkit for Scientific Computation
SPM	Statistic Parametric Mapping

Bibliography

[1] J. Malmivuo and R. Plonsey. *Bioelectromagnetism, Principles and Applications of Bioelectric and Biomagnetic Fields*. Oxford University Press, New York, 1995.

[2] ICNRIP. Guidelines for limiting exposure to time-varying electric, magnetic, and electromagnetic fields (up to 300 GHz). Technical report, ICNIRP, 2001.

[3] C. Polk and E. Postow. *Biological Effects of Electromagnetic Fields, Second Edition*. CRC Press, Boca Raton, London, New York, Washington DC, 1996.

[4] S. Gabriel, E. Corthout, and C. Gabriel. The dielectric properties of biological tissues: I. literature survey. *Phys. Med. Biol.*, 41:2231–2249, 1996.

[5] S. Gabriel, R. W. Lau, and C. Gabriel. The dielectric properties of biological tissues: II. measurements in the frequency range 10 Hz to 20 GHz. *Phys. Med. Biol.*, 41:2251–2269, 1996.

[6] S. Gabriel, R. W. Lau, and C. Gabriel. The dielectric properties of biological tissues: III. parametric models for the dielectric spectrum of tissues. *Phys. Med. Biol.*, 41:2271–2293, 1996.

[7] H. P. Schwan. Linear and nonlinear electrode polarization and biological materials. *Ann. Biomed. Eng.*, 20:269–288, 1992.

[8] L. A. Dissado and R. M. Hill. Non-exponential decay in dielectrics and dynamics of correlated systems. *Nature*, 279:685–689, 1979.

[9] S. Grimnes and O. G. Martinsen. *Bioimpedance and Bioelectricity Basics*. Academic Press, San Diego, 2000.

[10] V.C. Motrescu and U. van Rienen. Computation of currents induced by elf electric fields in anisotropic human tissues using the finite integration technique (FIT). *Advances in Radio Science*, 3:227–231, 2005.

[11] W.S. Snyder, M.R. Ford, G.G. Warner, and H.L. Fisher Jr. Mird pamphlet no.5: Estimates of absorbed fractions for monoenergetic photon sources uniformly distributed in various organs of a heterogeneous phantom. *J. Nucl. Med.*, 10:1, 1969.

[12] M. Christy. Mathematical phantoms representing children of various ages for use in estimates of internal dose. *ORNL/NUREG/TM-367*, 1980.

[13] E. Farfan, E. Han, C. Huh, T. Huston, E. Bloch, and W. Bloch. A revised stylized model of the extrathoracic and thoracic airways for use with the ICRP-66 respiratory tract model. *Health Physics*, 86:337, 2004.

[14] E.Y. Han, W. Bloch, and K. Eckermann. Revisions to the ORNL series of adult and pediatric computational phantoms for use with the MIRD schema. *Health Physics*, 90:3376, 2006.

[15] Ecole Polytechnique Federale de Lausanne. *http://visiblehuman.epfl.ch.*

[16] V. Spitzer, M.J. Ackerman, A.L. Scherzinger, and D. Whitlock. The visible human male: A technical report. *J. Am. Med. Inform. Assoc.*, 3:118–30, 1996.

[17] C. Lee and J.K. Lee. Computational anthropometric phantoms for radiation protection dosimetry: Evolution and prospects. *Nucl. Eng. and Tech.*, 38(3):239–249, 2006.

[18] I.G. Zubal, C.R. Harrell, E.O. Smith, Z. Rattner, G. Gindi, and P.B. Hoffer. Computerized 3-dimensional segmented human anatomy. *Med. Phys.*, 21:299, 1994.

[19] D.G. Jones. A realistic anthropometric phantom for calculating organ doses arising from external photon irradiation. *Radiation Protection Dosimetry*, 72:21, 1999.

[20] P. Dimbylow. Development of the female voxel phantom NAOMI, and its application to calculations of induced current densities and electric fields from applied low frequency magnetic and electric fields. *Phys. Med. Bio.*, 50:1047, 2005.

[21] C. Lee, C. Lee, and J.K. Lee. Korean adult male voxel model KORMAN segmented from magnetic resonance images. *Med. Phys.*, 31:1017, 2004.

[22] T. Nagaoka, S. Watanabe, K. Sakurai, E. Kunieda, S. Watanabe, M. Taki, and Y. Yamanaka. Developement of realistic high-resolution whole-body voxel models of japanese adult males and females of average height and weight, and application of models to radio-frequency electromagnetic-field dosimetry. *Phys. Med. Bio.*, 49:1, 2004.

[23] E.C. Prakash. Goal-directed deformation of the visible human. In Richard A. Banvard, editor, *The Second Visible Human Project Conference Proceedings*, 1998.

[24] W.P. Segars, D.S. Lalush, and M.W. Tsui. Development of a 4-D digital mouse phantom for molecular imaging research. *Molec. Imag. and Bio.*, 6:149, 2004.

[25] G. Xu and C. Shi. Preliminary development of a 4-D anatomical model for Monte Carlo simulation. In *Proceedings of the Monte Carlo Method: Versatility Unbounded in a Dynamic Computing World, Cattanooga, TN*, 2005.

[26] Wellcome Department of Imaging Neuroscience. *http://www.fil.ion.ucl.ac.uk/spm/.*

[27] J. Ashburner and K.J. Friston. Unified segmentation. *NeuroImage*, 26:839–851, 2005.

[28] S.M. Smith, M. Jenkinson, M.W. Woolrich, C.F. Beckmann, T.E.J. Behrens, H. Johansen-Berg, P.R. Bannister, M. De Luca, I. Drobnjak, D.E. Flitney, R. Niazy, J. Saunders, J. Vickers, Y. Zhang, N. De Stefano, J.M. Brady, and P.M. Matthews. Advances in functional and structural MR image analysis and implementation as FSL. *Neuro Image*, 23:208–219, 2004.

[29] FMRIB web page, 2007. http://www.fmrib.ox.ac.uk/fsl/.

[30] M. Sekino, K. Yamaguchi, N. Iriguchi, and S. Ueno. Conductivity tensor imaging of the brain using diffusion-weighted magnetic resonance imaging. *J. App. Phys.*, 93(110):6730, 2003.

[31] M. Sekino, Y. Inoue, and S. Ueno. Magnetic resonance imaging of electrical conductivity in the human brain. *IEEE Trans. Mag.*, 41(10):4203, 2005.

[32] F. Liu and S. Croizer. Electromagnetic ´fields inside a lossy, multilayered spherical head phantom excited by MRI coils: Models and methods. *Phys. Med Bio.*, 49:1835–1851, 2004.

[33] T. Weiland. A discretization method for the solution of Maxwell's equations for six-component fields. *Electronics and Communications AEÜ*, 31(3):116–120, 1977.

[34] T. Weiland. Time domain electromagnetic field computation with finite difference methods. *Int. J. Num. Mod.: ENDF*, 9:259–319, 1996.

[35] M. Bartsch, U. Becker, M. Dehler, M. Dohlus, Xingjun Du, S. Gutschling, R. Klatt, F. Krawczyk, M. Marx, M. Zhang, T. Pröpper, D. Schmitt, P. Schütt, B. Steffen, P. Thoma, B. Wagner, T. Weiland, S. G. Wipf, and H. Wolter. Finite integration: Ein universell anwendbares Verfahren zur Berechnung elektromagnetischer Felder. In *VDE- Fachberichte 45, Biologische Wirkungen elektromagnetischer Felder, (Vorträge der VDE Fachtagung in Bad Nauheim 9. -10. Nov. 1993)*, pages 109–118, 1993.

[36] T. Weiland and R. Schumann. Discrete electromagnetism by the finite integration technique. *Journal of the Japan Society of Applied Electromagnetics and Mechanics*, 10(2):159–169, 2002.

[37] M. Clemens. Large systems of equations in discrete electromagnetism: Formulations and numerical algorithms. *IEE Proceedings - Science, Measurement and Technology*, 152(2):50–72, 2005.

[38] M. Clemens, R. Schuhmann, and T. Weiland. Algebraic properties and conservation laws in the discrete electromagnetism. *Frequenz*, 53(11-12):218–225, 1999.

[39] R. Schuhmann and T. Weiland. A stable interpolation technique for FDTD on nonorthogonal grids. *Int. J. Num. Mod.: ENDF*, 11(6):299–306, May 1998.

[40] T. Weiland. Lossy waveguides with arbitrary boundary contour and distribution of material. *Electronics and Communcations AEÜ*, 33:170, 1979.

[41] P. Thoma. Zur numerischen Loesung der Maxwellschen Gleichungen im Zeitbereich. PhD thesis, Technische Universitaet Darmstadt, 1997.

[42] M. Clemens and T. Weiland. Magnetic field simulation using Conformal FIT formulations. *IEEE Trans. Magn.*, 38(2):389–392, 2002.

[43] O.P. Gandhi, J.F. Deford, and H. Kanai. Impedance method for calculation of power deposition patterns in magnetically induced hyperthermia. *IEEE Trans. Biomed. Eng.*, 31(10):644–51, 1984.

[44] D.W. Armitage, H.H. Leveen, and R. Pething. Radiofrequency induced hyperthermia: Computer simulation of specific absorption rate distributions using realistic anatomical models. *Phys. Med Bio.*, 28:31, 1983.

[45] O.P. Gandhi and J-Y. Chen. Numerical dosimetry at power-line frequencies using anatomically based models. *IEEE Trans. Biomed. Eng.*, Suppl 1:43–60, 1992.

[46] O.P. Gandhi, G. Kang, D. Wu, and G. Lazzi. Currents induced in anatomic models of the human for uniform and nonuniform power frequency magnetic fields. *Bioelectromagnetics*, 22:112–121, 2001.

[47] O P. Gandhi. Some numerical methods for dosimetry: Extremely low frequencies to microwave frequencies. *Radio Science*, 30(1):161–177, 1995.

[48] K. S. Yee. Numerical solution of initial boundary value problems involving Maxwell's equations in isotropic media. *IEEE*, AP-14:302–307, 1966.

[49] J. de Moerloose, T.W. Dawson, and M.A. Stuchly. Application of the finite difference time domain algorithm to quasi-static field analysis. *Radio Science*, 32(2):329–341, 1997.

[50] J. P. Berenger. A perfectly matched layer for the absorption of electromagnetic waves. *Journal of Computational Physics*, 114:185–200, 1994.

[51] T.W. Dawson and M.A. Stuchly. Analytic validation of a three-dimensional scalar-potential finite-difference code for low-frequency magnetic induction. *ACES Journal*, 11(3):72–81, November 1996.

[52] J. van Bladel. *Electromagnetic Fields*. Hemisphere Publishing Corporation, Washington DC, 1985.

[53] K. Caputa, P. J. Dimbylow, T. W. Dawson, and M. A. Stuchly. Modelling fields induced in humans by 50/60 Hz magnetic fields: Reliability of the results and effects of model variations. *Physics in Medicine and Biology*, 47:1391–1398, 2002.

[54] T.W. Dawson, K. Caputa, and M.A. Stuchly. A comparison of 60 Hz uniform magnetic and electric induction in the human body. *Phys. Med. Biol.*, 42:2319–2329, 1997.

[55] T.W. Dawson, K. Caputa, and M. A. Stuchly. High-resolution organ dosimetry for human exposure to low-frequency electric fields. *IEEE Transactions on Power Delivery*, 13(2):366–373, 1998.

[56] A. Hirata, K. Caputa, T.W. Dawson, and M.A. Stuchly. Dosimetry in models of child and adult for low-frequency electric field. *IEEE Transactions on Biomedical Engineering*, 48(9):1007–1012, September 2001.

[57] M.A. Stuchly and O.P. Gandhi. Inter-laboratory comparison of numerical dosimetry for human exposure to 60 Hz electric and magnetic fields. *Bioelectromagnetics*, 21:167–74, 2000.

[58] T.W. Dawson, J. de Moerloose, and M.A. Stuchly. Comparison of magnetically induced ELF fields in humans computed by FDTD and scalar potential FD codes. *ACES Journal*, 11(3):63–71, November 1996.

[59] T. Kowalski, J. Silny, and H. Buchner. Current density threshold for the stimulation of neurons in the motor cortex area. *Bioelectromagnetics*, 23:421–428, 2002.

[60] T.A. Wagner, M. Zahn, A.J. Grodzinski, and A. Pascual-Leone. Three-dimensional head model simulation of tanscranial magnetic stimulation. *IEEE Tran. Bio. Med. Eng.*, 51(9):1586–1589, 2004.

[61] M. Clemens, A. Barchanski, H. De Gersem, M. Rezinkina, and T. Weiland. Numerical simulation of low-frequency current density distributions in voxel-based human anatomy models due to ambient electric and magnetic fields. In *Proc. CEM 2004 Conference, Stratford-upon-Avon, United kingdom*, 2004.

[62] T.W. Dawson, S. Velamparambil, and M.A. Stuchly. Hybrid integral equation and finite difference method for lowfrequency electric induction. *ACES Journal*, 16(3):218–227, 2001.

[63] S. Balay, K. Buschelman, W.D. Gropp, D. Kaushik, M. Knepley, L.C. McInnes, B.F. Smith, and H. Zhang. PETSc users manual. Technical Report ANL-95/11 - Revision 2.1.5, Argonne National Laboratory, 2002.

[64] S. Balay, W.D. Gropp, L.C. McInnes, and B.F. Smith. Efficient management of parallelism in object oriented numerical software libraries. In E. Arge, A. M. Bruaset, and H. P. Langtangen, editors, *Modern Software Tools in Scientific Computing*, pages 163–202. Birkhauser Press, 1997.

[65] V.E. Henson and U.M. Yang. Boomeramg: A parallel algebraic multigrid solver and preconditioner. *Appl Numer. Math.*, 41:155–77, 2002.

[66] P. Thoma. *Zur numerischen Lösung der Maxwellschen Gleichungen im Zeitbereich.* PhD thesis, Technische Universität Darmstadt, 1997.

[67] O. Pŏdebrad. *Finite Integration der Maxwellschen Gleichungen auf lokal verfeinerten orthogonalen Gittern.* PhD thesis, Technische Universität Darmstadt, 2001.

[68] M. Clemens, S. Feigh, M. Wilke, and T. Weiland. Geometric multigrid algorithms using the conformal finite integration technique. *IEEE Trans. on Magn.*, 40(2):1065–1068, 2004.

[69] C. Bernardi, Y. Maday, and A.T. Patera. *A new nonconforming approach to domain decomposition: The mortar element method,*. Nonlinear Partial Differential Equations and Their Application. Pitman, New York, 1994.

[70] B. Fischer, A. Ramage, D.J. Silvester, and A.J. Wathen. Minimum residual methods for augmented systems. *BIT*, 38(3):527–543, 1998.

[71] H. De Gersem, M. Wilke, M. Clemens, and T. Weiland. Efficient modeling techniques for complicated boundary conditions applied to structured grids. *Compel*, 23(4):904–912, 2004.

[72] S. Schulze and U. van Rienen. Computation of land mine signatures using domain decomposition with lagrange multipliers. In *The 12th Biennial IEEE Conference on Electromagnetic Field Computation, Miami, FL, April 30th - May 3rd*, 2006.

[73] A. Thomasset. Proprietes bio-electriques des tissus. mesures de l'impedance en clinique. signification des courbes obtenues. *Lyon Med*, 207:107–118, 1962.

[74] I. Janssen, S.B. Heymsfeld, R.N. Baumgartner, and R. Ross. Estimation of skeletal muscle mass by bioelectrical impedance analysis. *J Appl Physiol*, 78:465–471, 2000.

[75] U.G. Kyle, L. Genton, D.O. Slosman, and C. Pichard. Fat-free and fat mass precentiles in 5225 healthy subjects aged 15 to 98 years. *Nutrion*, 17:534–541, 2001.

[76] K.R. Segal, M. Van Loan, P.I. Fitzgerald, J.A. Hodgdon, and T.B. Van Itallie. Lean body mass estimation by bioelectrical impedance analysis: a four-site cross-validation study. *Am. J. Clin. Nutr.*, 47:7–14, 1988.

[77] C. Pichard, U.G. Kyle, D. Bracco, D.O. Slosman, A. Morabia, and Y. Schultz. Reference values of fat-free and fat masses by bioelectrical impedance analysis in 3393 healthy subjects. *Nutrion*, 16:245–254, 2000.

[78] R. Rubinacci and G. Albanese. Integral formulation for 3d eddy-current computation using edge elements. *IEE Proceedings*, 135(7):457, 1988.

[79] H. Igarashi. On the property of the curl-curl matrix in finite element analysis with edge elements. *IEEE Trans. Magn.*, 37(5):1325–1329, 2001.

[80] M. Clemens and T. Weiland. Regularization of eddy current formulations using discrete grad-div operators. *IEEE Trans. Magn.*, 38(2):569–572, 2002.

[81] K. Kumar, G Hunter, and D Demeria. Spinal cord stimulation in treatment of chronic benign pain: Challanges in treatment planning and present status, a 22-year experience. *Neurosurgery*, 58:481–496, 2006.

[82] T. Tsubokawa, Y. Katayama, T. Yamamoto, T. Hirayama, and S. Koyama. Chronic motor cortex stimulation for the treatment of central pain. *Acta Neurochir Suppl (Wien)*, 52:137–139, 1991.

[83] L.C. Kloth and J.A. Feedar. Acceleration of wound healing with high voltage, monophasic, pulsed current. *Phys Ther*, 68:503–508, 1988.

[84] M.J. Sjorgen, P.T. Hellstrom, M.A. Jonsson, M. Runnerstam, H.C. Silander, and E. Ben-Menachem. Cognition-enhancing effect of vagus nevre stimulation in patients with alzheimers's disease: A pilot study. *J Clin Psychiatry*, 63:972–980, 2002.

[85] P. Limousin, P. Pollak, A. Benazzouz, D. Hoffmann, JF Le Bas, E. Broussolle, JE Perret, and AL Benabid. Effect of parkinsonian signs and symptoms of bilateral subthalamic nucleus stimulation. *Lancet*, 345(8942):91–5, 1995.

[86] W. Koller, R. Pahwa, K. Busenbark, J. Hubble, S. Wilkinson, A. Lang, P. Tuite, E. Sime, A. Lazano, R. Hauser, et al. High-frequency unilateral thalamic stimulation in the treatment of essential and parkinsonian tremor. *Ann Neurol*, 42(3):292–9, 1997.

[87] P.D. Faghri, M.M. Rodgers, R.M. Glaser, J.G. Bors, C. Ho, and P. Akuthota. The effects of functional electrical stimulation on shoulder subluxation, arm function recovery, and shoulder pain in hemiplegic stroke patients. *Arch Phys Med Rehabil*, 75(1):73–9, 1994.

[88] J. Liepert, W.H. Miltner, H. Bauder, M. Sommer, C. Dettmers, E. Taub, and C. Weiller. Motor cortex plasticity during constraint-induced movement therapy in stroke patients. *Neurosci Lett*, 250(1):5–8, 1998.

[89] R.G. Bickford and B.D. Freeming. Neuronal stimulation by pulsed magnetic fields in animals and man. page 112, 1965. Digest of the 6th International Conference of Medical Electronics in Biology and Engineering.

[90] A.T. Barker, R. Jalinous, and I.L. Freeston. Non-invasive magnetic stimulation of human motor cortex. *Lancet*, 1(8437):1106–7, 1985.

[91] W. Paulus, M. Hallet, P.M. Rossini, and Rothwell. *Transcranial Magnetic Stimulation. Proceedings of the International Symposium on Transcranial Magnetic Stimulation, Goettingen, 1998*. Elsevier, 1999.

[92] M. Nadeem, T. Thorlin, O. Gandhi, and M. Persson. Computation of electric and magnetic stimulation in human head using the 3-d impedance method. *IEEE Trans. Biomed. Eng.*, 50(7):900–906, 2003.

[93] P. Nicholson. Specific impedance of cerebral white matter. *Exp. Neurol.*, 13:386–401, 1965.

[94] T. Krings, B.R. Buchbinder, and W.E. Butler. Functional magnetic resonance imaging and transcranial magnetic stimulation: Complementary approaches in the evaluation of cortical motor functions. *Neurology*, 48:1406–1416, 1997.

[95] A.L. Hodgin and A.F. Huxley. A quantitative description of membrane current and its application to conduction and excitation in nerve. *Journal of Physiology*, 117:500–544, 1952.

[96] A. Pascual-Leone. *Handbook of Transcranial Magnetic Stimulation*. Arnold Publishers, 2002.

[97] F. Rattay. Analysis of models for extracellular fiber stimulation. *IEEE Tran. Biomed. Eng.*, 36, 1989.

[98] The Hypre Project High Performance Preconditioners. *http://www.llnl.gov/CASC/hypre/*.

[99] S. Feigh, M. Clemens, and T. Weiland. Geometric multigrid method for electro- and magnetostatic field simulations using the Conformal Finite Integration Technique. Virtual Proc. 11th Copper Mountain Conf. on Multigrid Methods (CMCMM 2003), USA. (www.mgnet.org)., 2003.

Acknowledgments

sorry, this part is in German... :-)

An dieser Stelle möchte ich allen Danken, die mich auf meinem Weg bis zur Fertigstellung dieser Arbeit begleitet haben.

- Prof. Dr. Thomas Weiland, für die Aufnahme am Institut, und die Schaffung optimaler Arbeitsbedingungen.
- Prof. Dr. Volkert Hansen, für die freundliche Übernahme des Korreferates.
- Prof. Dr. Markus Clemens, für das Schaffen einer Stelle im Bereich des Bioelektromagnetismus, und die zahlreichen 'Steuerzahlermittagessen'.
- Prof. Dr. Herbert 'Chef' De Gersem, für die zahlreichen Hilfestellungen während meiner Zeit bei TEMF.
- Dr. Erion 'Vincenzo' Gjonaj, für unzähligen theoretischen Input, und Teile seiner Software.
- Dipl.-Ing. Stephan 'Chab' Koch, für soooo viele Zigarettenpausen, und einen unvergesslichen Florida Trip.
- Frau Heike Seiler, für die Unterstützung bei allem, um was man sich Abseits der Wissenschaft noch so kümmern muss.
- Allen Mitarbeitern am Institut für Theorie Elektromagnetischer Felder, die stets für ein sehr angenehmens Arbeitsklima gesorgt haben.
- Allen Freunden und Bekannten, besonders Steffen, Benny und Fabian, die während der Entstehungszeit dieser Arbeit für Abwechlsung vom Institutsalltag gesorgt haben.
- Frau Christina Elisa Lubahn, für ihre Geduld und ihre Nähe.
- Schließlich bedanke ich mich bei meiner Familie und besonders meinen Eltern für die bedingungslose Unterstützung, und für das Interesse an meiner Arbeit.

Curriculum Vitae

Andreas Barchanski
born on 14. December 1976 in Kattowitz

1983-1987	Primary school in Zabrze
1987-1993	Middle school in Hanau
1993-1996	High school in Hanau
1996-1997	Military service
1997-2003	Master degree study (Dipl.Phys.) of physics at the TU Darmstadt
2003-2007	Research assistant at the Institut für Theorie Elektromagnetischer Felder, TU Darmstadt